Electric Field Grading by Functionally Graded Materials (FGM) for HVDC Gas Insulated Power Apparatus

Rachmawati

Electric Field Grading by Functionally Graded Materials (FGM) for HVDC Gas Insulated Power Apparatus

Chapter 1 Introduction

1.1 HVDC Gas Insulated Power Equipment

1.1.1 HVDC Power Transmission

Nowadays, global electricity consumption has been increasing at a faster rate than energy consumption. In 2017, the world's annual electricity consumption rose to 22.3 trillion kWh from 13 trillion kWh in 2000. In 2018, the electricity sector holds 25.4% share of the total final energy consumption [1, 2]. On the other hand, along with the growth in economy, the electricity consumption tends to spread across regions within a country, though the main source of energy is generally localized. In many cases, the electricity is even traded among countries. Due to this growing necessity of electricity combined with the encouragement for affordable and clean energy from the Sustainable Development Goals (SDGs), power generations from renewable energy have been expanding in the last decades and are expected to accelerate in the future that require higher capacity of power delivery over long distances [3, 4].

As a solution to these problems, high voltage direct current (HVDC) technology has played the important role in long distance transmission, grid interconnection of AC systems, submarine power cables, and frequency converter [5–7]. HVDC provides advantages for those purposes, such as high-capacity transmission lines over long distance, low losses (higher efficiency), compact infrastructures (transmission tower size, number of conductors), no skin effect, and enabling asynchronous interconnections [8–10].

Japan is a good example of a country that implements the technology for those various purposes, where there are 9 DC facilities in total, operating as HVDC interconnection (Japan's first 500 kV-designed Kii Channel, two Hokkaido-Honshu submarine cable transmissions, and newly operating Hida-Shinano frequency converter), frequency converters between 50 Hz and 60 Hz (at Sakuma, Shin-Shinano 1 and 2, Higashi Shimizu), back-to-back (BTB) converter station (at Minami-Fukumitsu) [11, 12]. In China, ultra-high voltage (UHV) and UHVDC power transmission for voltage level ±800 kV and above have been progressing to fulfill the demand on long distance transmission [13]. Many

HVDC links used as grid interconnections and power exchange within and between countries can be found in Europe, Russia, and North America, where they deliver vast amount of power from various renewable energy sources, such as hydro energy, solar energy in desert areas, and vast off-shore wind farms to the load centers [14, 15]. Current development comes from the German Network Extension Plan which builds 12 GW of HVDC links within Germany to connect offshore wind power in the northern part to the load hubs in southern Germany [16].

With the progressive development of HVDC power transmission in the world, more research and projects are happening to reinforce compact and reliable infrastructure and DC power apparatus. Particularly in this dissertation, the focus is the improvement of insulation performance and reduction of size and SF_6 gas volume for DC gas-insulated switchgear (GIS) and gas-insulated transmission line (GIL).

1.1.2 Technology of GIS/GIL

The gas insulated equipment, such as GIS and GIL were initially established for AC transmission system since the 1960s, where problems regarding space or right-of-way occur in highly populated areas. The equipment has been favorable in the present power transmission system since it offers compactness, high reliability, ease of maintenance, less sensitive to environmental exposure, and safety for personnel [5, 17]. Up to now, there are AC GIS/GILs operating at rated voltages from 72.5 kV up to 1200 kV worldwide [18]. As the application to AC system have been well-proven, the application to DC system started to be considered in 1980, and the history of DC GIS until recent days is shown in Fig. 1.1, where the number of bays connected to the DC GIS increase as more of the equipment with increased voltage level are put into operation [19]. Currently HVDC GIS/GILs for at least ±550 kV rated voltage have been developed worldwide. For example, a ±320 kV HVDC GIS which was built for offshore application allows space reduction up to 95% for the switchgear, and the total size reduction of the HVDC platform up to 10%, with typical configuration as shown in Fig. 1.2 [6, 8].

Fig. 1.3 shows the (a) appearance, (b) constructions, and (c) single line diagram of 362 kV, 63 kA GIS [20]. The power equipment, such as busbars, circuit breakers, line disconnector, current transformer, earthing switches are housed in metal tanks filled with

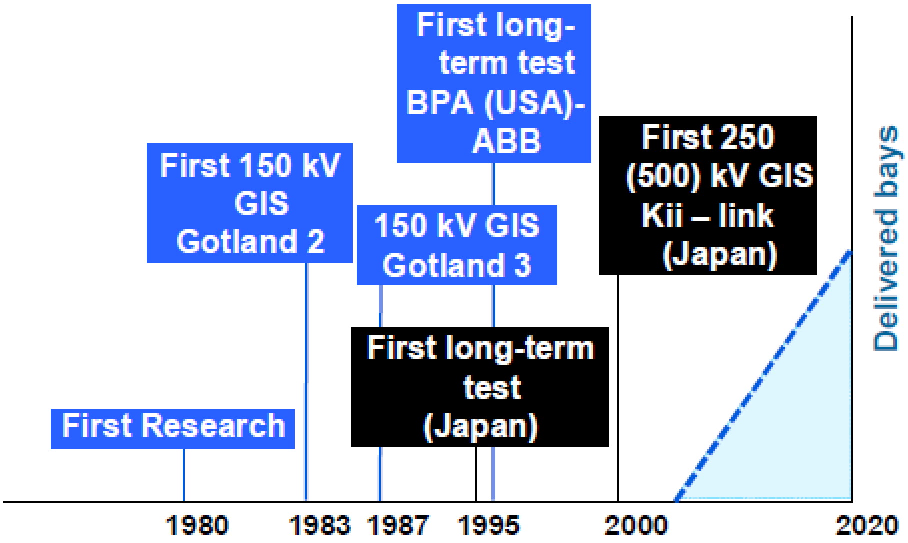

Fig. 1.1 DC GIS milestones [19].

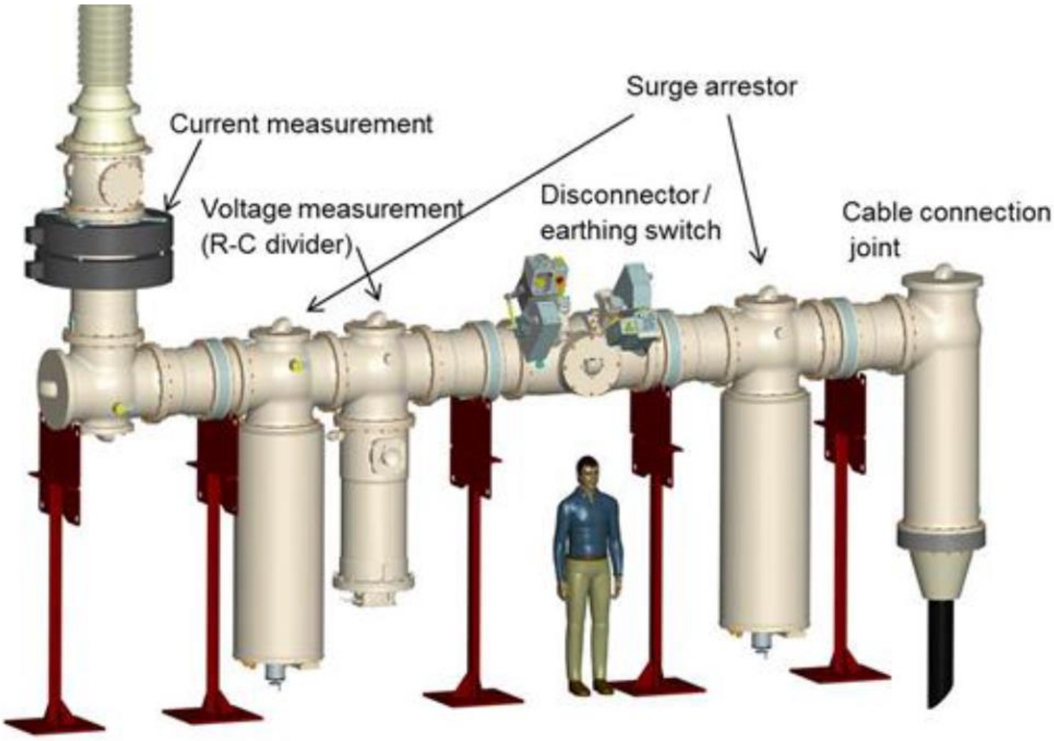

Fig. 1.2 Typical configuration of ±320 kV DC compact switchgear by Siemens [8].

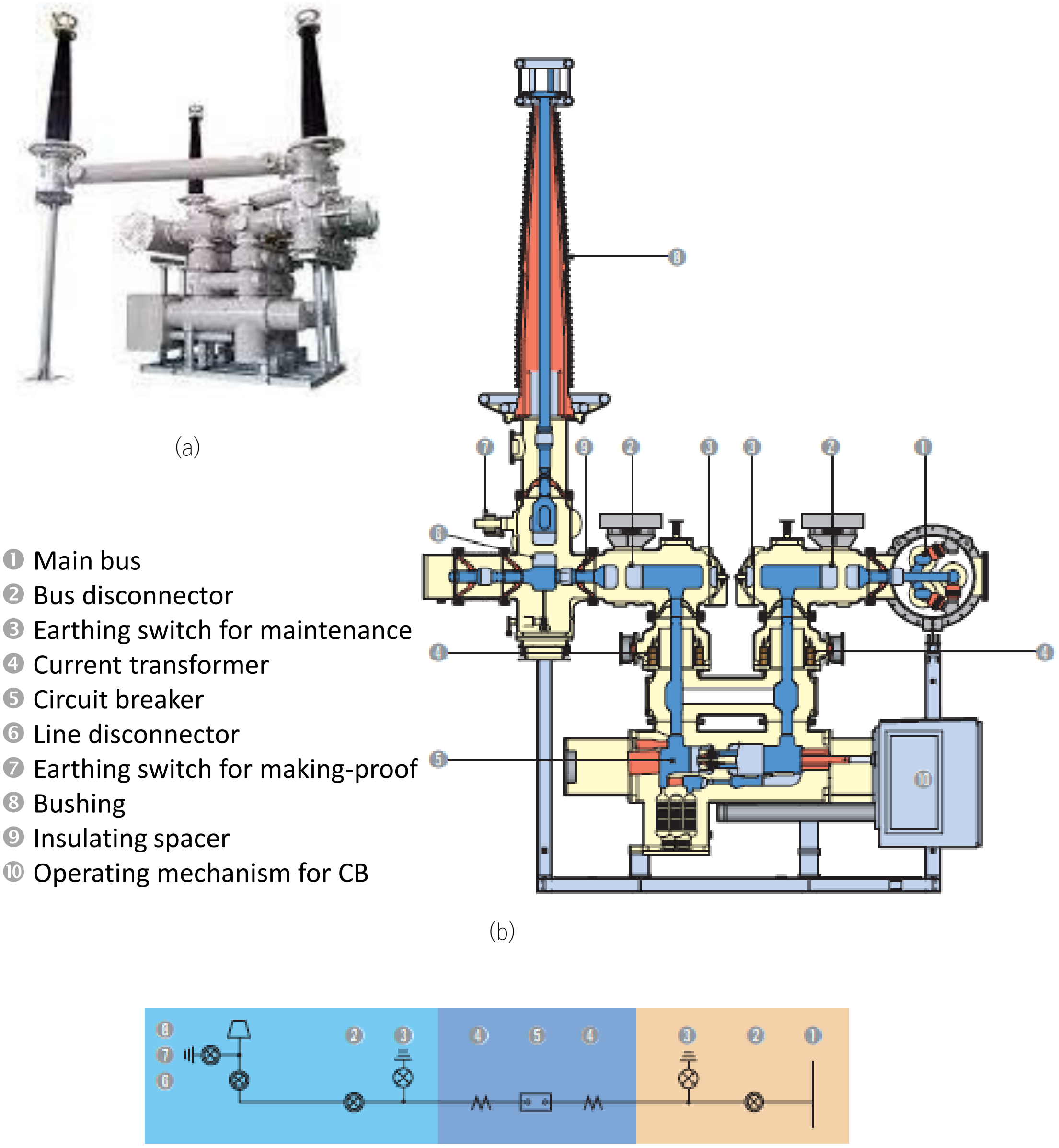

(a)

(b)

(c)

Fig. 1.3 (a) Appearance, (b) constructions, and (c) single line diagram of 362 kV, 63 kA GIS [20].

gas at high pressures. In GIS, sulfur hexafluoride (SF_6) gas is commonly used due to its excellent properties for arc extinguishing and electrical insulation, while in GIL SF_6 or the mixture of SF_6/N_2 is used to provide excellent electrical insulation and global warning mitigation. Beside gas insulation, solid insulators are also contained in GIS/GIL in the forms of post-type, cone-type or disk-type insulators, also known as spacers, to hold steady the HV conductor in the center of GIS/GIL against the ground enclosure, and at the same time to separate the gas compartments in GIS/GIL, as shown in Fig. 1.4 [6, 21].

As SF_6 gas has been pronounced as an extremely potent greenhouse gas with GWP values of 23,500 [22], the investigation of alternative gases in order to replace SF_6 gas is vigorously researched nowadays. In the meantime, it is required to utilize and at the same time to reduce the usage of SF_6 gas for global warming mitigation. Downsizing the GIS/GIL is one of the effective ways that may reduce not only SF_6 gas usage, but also cost, installation space, and manufacturing energy [23].

1.1.3 Challenges in Solid Insulator Development of HVDC GIS/GIL

For both HVAC and HVDC equipment, downsizing the gas insulated equipment results in higher electric field stress in the insulation medium, hence it needs to be reduced or controlled in order to maintain the high reliability of the apparatus [24]. However, there are differences regarding electric field distribution in HVAC and HVDC equipment, so that we cannot simply apply the existing design of HVAC GIS/GIL and their components to the HVDC ones. First of all, the electric field distribution under AC voltage is determined by the permittivity of gas and spacer, whereas under DC voltage it is determined by the conductivity. Secondly, unlike permittivity, conductivity strongly depends on or varies with temperature [25]. Furthermore, the shape of the spacer between the HV conductor and GND enclosure may cause electric field intensified, especially at the contacts where gas, spacer, and HV conductor/GND enclosure meet, also known as the triple junctions [26-27]. Fig. 1.5 shows how electric field distribution differs in GIS/GIL under (a) AC voltage, (b) DC voltage without temperature difference ($\Delta T = 0$) between the HV conductor and the GND enclosure, and (c) DC voltage with temperature difference ($\Delta T > 0$) [8, 28]. Under AC voltage (Fig. 1.5 (a)), high electric field stress is found on the surface of HV conductor. On the other hand, when DC voltage is applied and $\Delta T = 0$ (Fig. 1.5 (b)), electric field is

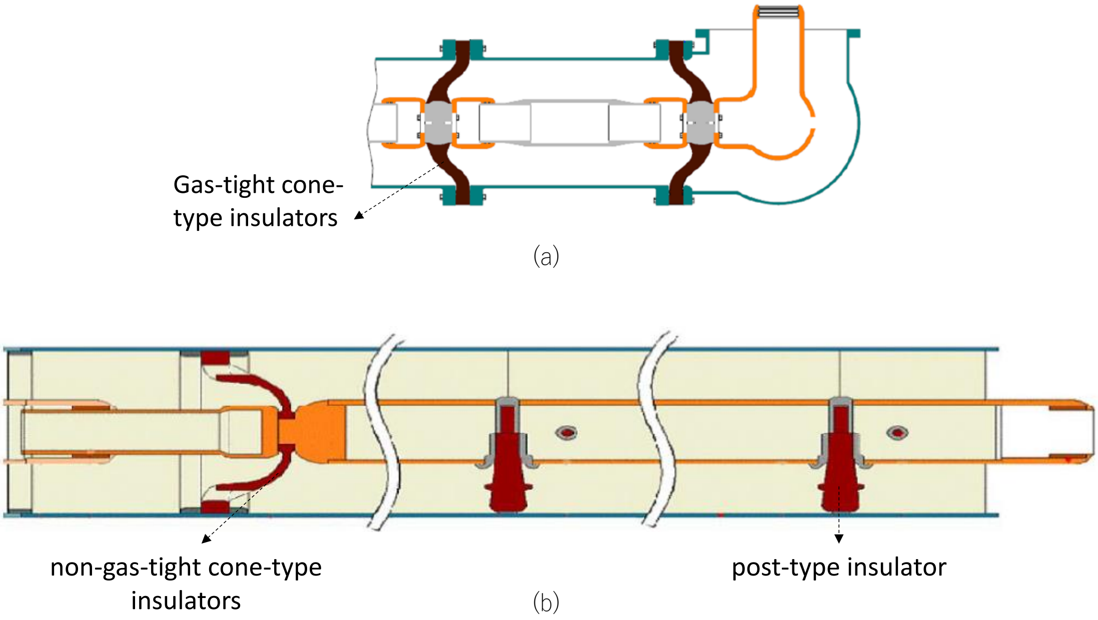

(a)

(b)

Fig. 1.4 Types of solid insulators in (a) GIS, and (b) GIL [6,21].

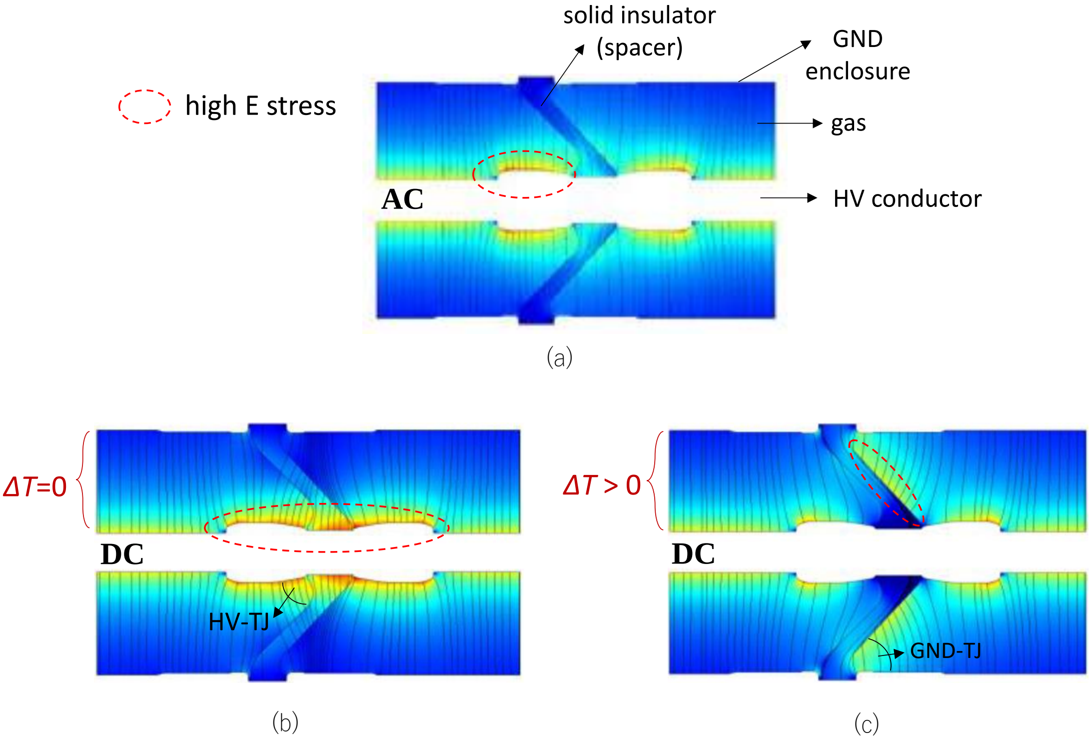

(a)

(b)

(c)

Fig. 1.5 Electric field distribution in GIS/GIL under (a) AC voltage, (b) DC voltage without temperature difference, and (c) DC voltage with temperature difference between HV conductor and GND enclosure [8,28].

intensified around the triple junction near the HV side (HV-TJ), as well as on the spacer/HV conductor's interface. In Fig. 1.5 (c) under DC voltage and $\Delta T > 0$, high electric field stress is found on the spacer surface up to the triple junction near GND side (GND-TJ). Both triple junctions are critical areas in GIS/GIL, where breakdowns can easily occur if the high electric field stress is uncontrolled. Therefore, an innovative way is required to reduce the high electric field stress in the insulation system under DC voltage.

1.2 Electric Field Grading

Electric field grading or stress grading commonly implies to the methods to reduce the locally intensified electric field at one spot and distribute it more evenly to other areas within or around the insulation medium. The high electric field stress is usually unavoidable when there is large potential difference, e.g. at terminals of transmission equipment. Hence, it must be controlled so that partial discharges and breakdowns do not occur in the insulation medium, particularly in HV apparatus, where an overstressed weak spot can lead to insulation failures [27].

1.2.1 Capacitive and Resistive Electric Field Distributions

The basic concept of electric field grading comes from the Ampere's Law of Maxwell's equation, where the total current density $\vec{J}$ consists of the conduction current by moving charges $\vec{J_c}$ and the displacement current $\vec{J_d}$, as shown in equation (1.1).

$$\vec{J} = \vec{J_c} + \vec{J_d} \tag{1.1}$$

The conduction current of moving charges J_c is defined by the electric field $\vec{E}$ and the conductivity (σ) of the material, as in equation (1.2),

$$\vec{J_c} = \sigma\vec{E} \tag{1.2}$$

and the displacement current $\vec{J_d}$ is defined as the time-varying displacement field ($\vec{D}$) and can be calculated by the permittivity (ε) of the material and the time-dependent electric field as in equation (1.3).

$$\vec{J_d} = \frac{\partial\vec{D}}{\partial t} = \varepsilon\frac{\partial\vec{E}}{\partial t} \tag{1.3}$$

By substituting equations (1.2) and (1.3) to equation (1.1), the following equation (1.4) of total current density is obtained.

$$\vec{J} = \sigma\vec{E} + \varepsilon\frac{\partial\vec{E}}{\partial t} \tag{1.4}$$

The conductivity σ and permittivity ε are the principal material properties that describes the response to the applied electric fields.

From Maxwell-Ampere equation,

$$\nabla \times \vec{H} = \vec{J} = \sigma\vec{E} + \varepsilon\frac{\partial\vec{E}}{\partial t} \tag{1.5}$$

By applying divergence (vector's identity) to equation (1.5), below derived equations are obtained.

$$\nabla \cdot \left(\nabla \times \vec{H}\right) = \nabla \cdot \vec{J} = 0 \tag{1.6}$$

$$\nabla \cdot \left(\sigma\vec{E} + \varepsilon\frac{\partial\vec{E}}{\partial t}\right) = 0 \tag{1.7}$$

$$\nabla \cdot \left(\sigma + \varepsilon\frac{\partial}{\partial t}\right)\vec{E} = 0 \tag{1.8}$$

Here, if the electric field E changes with ω, by applying Fourier transform, then the continuity equation becomes,

$$\nabla \cdot (\sigma + j\omega\varepsilon)\dot{\boldsymbol{E}} = 0 \tag{1.9}$$

where $\dot{\boldsymbol{E}}$ is the complex electric field.

As the electric field $\vec{E}$ is related to the electric potential φ as follows,

$$\vec{E} = -\mathrm{grad}\varphi = -\nabla\varphi \tag{1.10}$$

by substituting equation (1.10) to equation (1.9), the continuity equation is obtained as follows,

$$\nabla \cdot (\sigma + j2\pi f\varepsilon)(-\nabla\varphi) = 0 \tag{1.11}$$

$$\nabla \cdot \left(\varepsilon - j\frac{\sigma}{2\pi f}\right)\nabla\varphi = 0 \tag{1.12}$$

where f is assumed to be the frequency of the applied AC voltage. Therefore, when AC voltage is applied or immediately after DC voltage is applied ($\varepsilon \gg \sigma/f$), the term related to permittivity ε stands (in equation (1.12)), i.e. the displacement current $\overrightarrow{J_d}$ with decisive ε is usually dominant. Here, the conduction current $\overrightarrow{J_c}$ is ignored

$$\nabla \cdot (\varepsilon\nabla\varphi) = 0 \tag{1.13}$$

On the other hand, for DC (resistive) fields, as long as it is under constant DC stress (at DC steady state, f=0), only the conduction current $\overrightarrow{J_c}$ with σ of the material is needed to be considered, and therefore $\overrightarrow{J_d}$ is neglected. Hence, the equation below applies.

$$\nabla \cdot (\sigma \nabla \varphi) = 0 \tag{1.14}$$

Nevertheless, in case of time-varying voltage change under DC system, such as at DC-on and DC polarity reversal, then AC or capacitive electric fields should be taken into account as well [27].

1.2.2 Electric Field Grading Concept

The purpose of electric field grading is to change the potential distribution smoothly along the interfaces (surface) or within the bulk (volume) of electrical insulation so that electric fields are distributed more uniformly and the field stress is kept below critical levels. By doing so, it allows us to scale down the size of the insulating material or operate the equipment at higher voltage. Table 1.1 shows the main types of electric field grading as well as the overviews of each concept [27].

In geometric field grading, electric field distribution is influenced by adding conductive surfaces (electrodes) which are connected to certain potentials (usually HV or GND) so that the corresponding dielectric stress is within a tolerable limit. For example, in GIS/GIL, a shield electrode is added to control high electric field stress around HV-TJ. In capacitive field grading, conductive grading layers are formed between high voltage and potential, such as in condenser type bushing, where the graded potential distribution is created through capacitance between layers [29]. Surface field grading has aims to find a suitable potential distribution along a surface or interface between different materials to prevent surface discharges. It can be done by using embedded electrodes in the insulating material or by adding conductive layer on the insulating surface (resistive field control) [30].

Fig. 1.6 shows the potential and electric field distribution inside GIS, in which there are examples of geometry field grading and surface field grading by adding shield electrode on HV side, spacer shape optimization and adding embedded electrode in the spacer near GND side [24]. However, structure modification can be a complicated process. Therefore, applying conductive layer on a GIS spacer can be an easier way to reduce electric field stress while maintaining the simple shape of the spacer, such as shown in Fig. 1.7. In Fig. 1.7 (a), high electric field stress is seen at the triple junction of HV conductor, SF_6 gas and the conventional spacer with ε_r=6. On the other hand, Fig. 1.7 (b)

Table 1.1 Overview of electric field grading concepts [27].

Electric field grading concept	Significant parameter for DC	Significant parameter for AC
1) Geometry (bulk field grading) 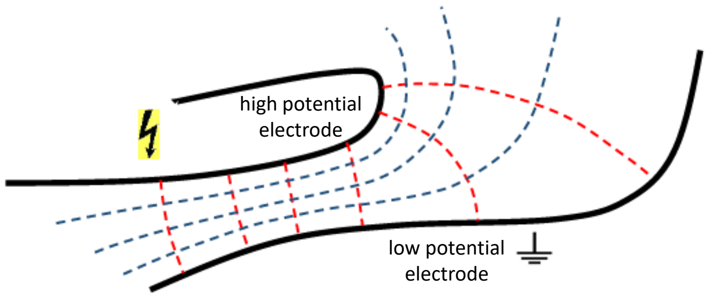	shape of electrode and total current density along electrodes	
2) Potential grading (capacitive/resistive field grading, bulk field grading) 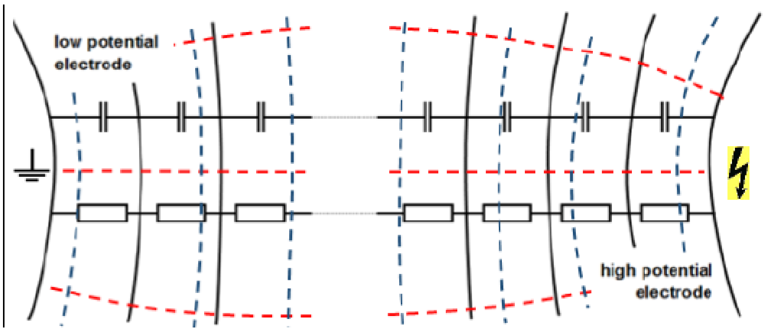	σ of layer between adjacent grading foils	ε of layer between adjacent grading foils
3) Potential grading (surface field grading) 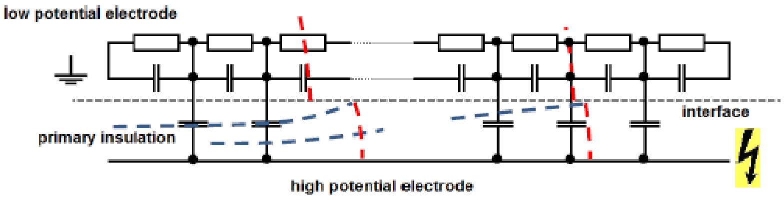	σ	σ and ε
4) Nonlinear materials with field dependent conductivity/permittivity	σ = *f* (E)	ε = *f* (E) σ = *f* (E)
5) Continuous or stepwise discrete functionally graded materials	σ = *f* (x, y, z, E, ϑ,…)	ε = *f* (x, y, z, E, ϑ,…) σ = *f* (x, y, z, E, ϑ,…)

Notes: red dashed lines = field lines, blue dashed lines = equipotential lines

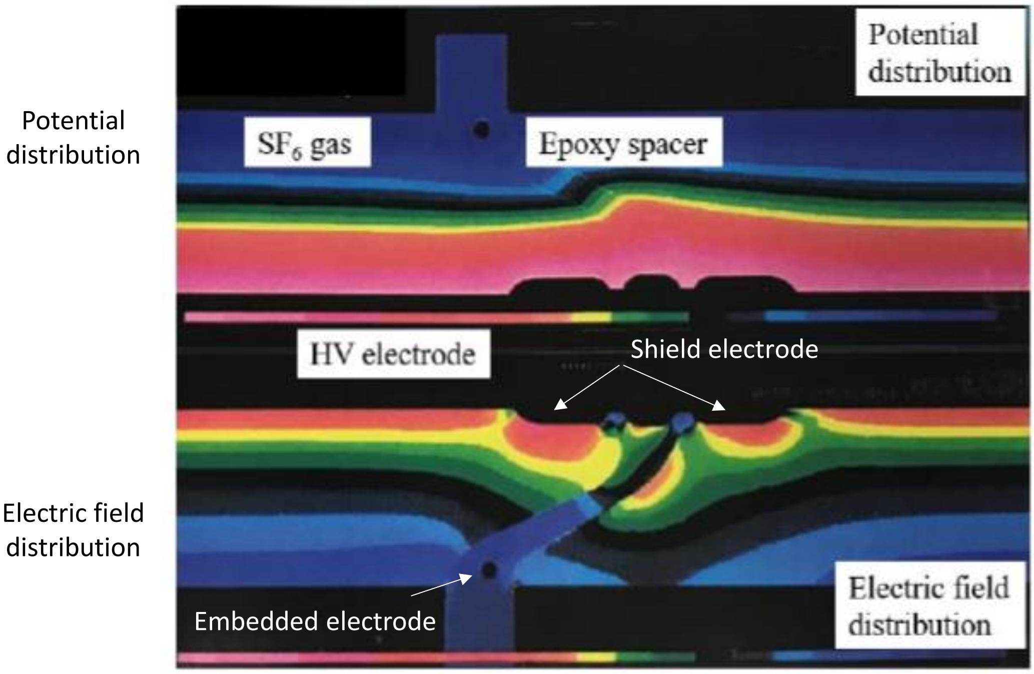

Fig. 1.6 Electric field distribution around GIS spacer [24].

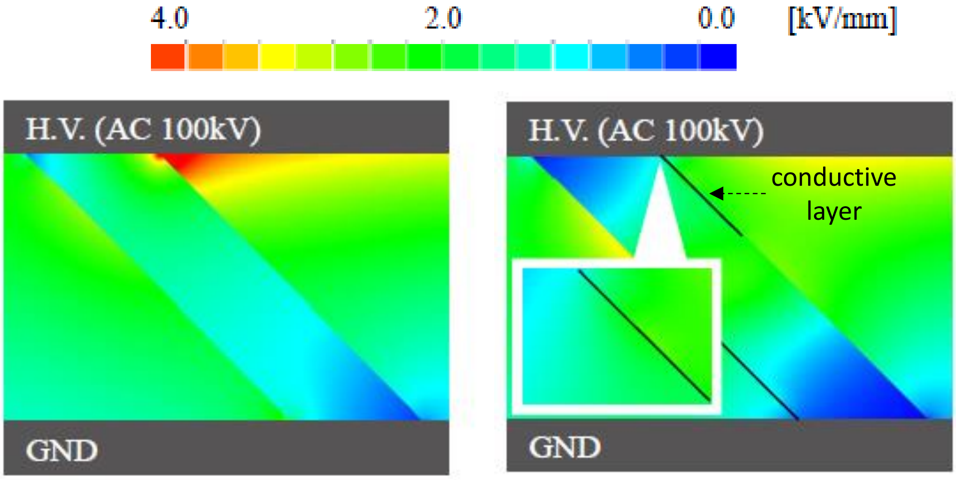

(a) conventional spacer
σ = 0 S/m, ε_r = 6

(b) σ/ε-FGM
$\sigma = 10^{-4}$–10^{-7} S/m, ε_r = 30-6-30

Fig. 1.7 Electric field distribution around GIS spacer with and without conductive layer [30].

shows the suppressed electric field stress around that area due to application of conductive layer on the spacer surface with exponentially graded σ of 10^{-4} to 10^{-7} S/m, and parabolically graded ε_r which is applied to the spacer bulk (ε_r=30 at the spacer/HV conductor and spacer/GND tank interfaces, and ε_r=6 at the center of the spacer). This method was the first stage of research on functionally graded materials (FGM).

Nonlinear materials have property that changes itself in a nonlinear manner when, for example, a certain field strength is exceeded (switching field). So far it is only nonlinear resistive field materials with electric field-dependent conductivity, such as microvaristors that are mixed into elastomer. Fig. 1.8 shows an application of SiR/ZnO microvaristor composites as field grading layer in a 500-kV cable termination [31].

1.2.3 Functionally Graded Materials (FGM)

The last concept is the functionally graded materials (FGM), which becomes the focus in this research. FGM here differ from the previously mentioned nonlinear materials in a way that the material properties (conductivity and/or permittivity) change spatially within the solid insulator bulk in order to control resistive and/or capacitive fields. The following sections will discuss the details about the materials used, fabrication techniques, and the application of FGM to GIS/GIL spacers.

1.3 Material and Fabrication

1.3.1 Materials

The materials used for field grading are divided into two categories, which are the matrix materials and the filler materials. The matrix materials can be glass, thermoplastic polymers (e.g. polyethylene (PE), polyvinyl chloride (PVC), and polypropylene (PP) for insulators or spacers), thermoset polymers (e.g. epoxy resin (EP) as cast resins, polyurethane (PUR), cross-linked polyethylene (XLPE) for cable insulations), and elastomers (e.g. silicone rubbers, ethylene propylene rubber (EPM), ethylene propylene diene rubber (EPDM) for cable accessories, suspension, and post insulators) [27].

Fillers are particles that added to a matrix in order to change its physical properties, such as the color and strength. In the case of electric field grading, it is to change the

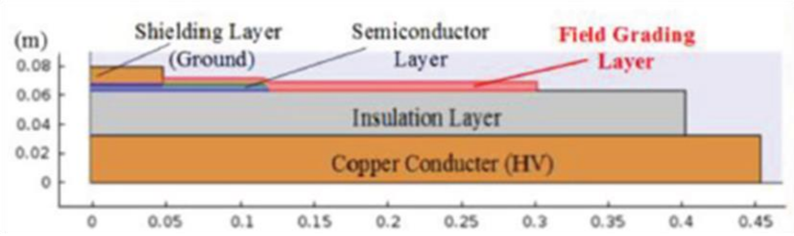

(a) schematic of cable structure

(b) E distribution without grading layer

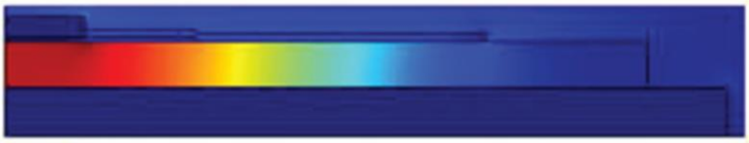

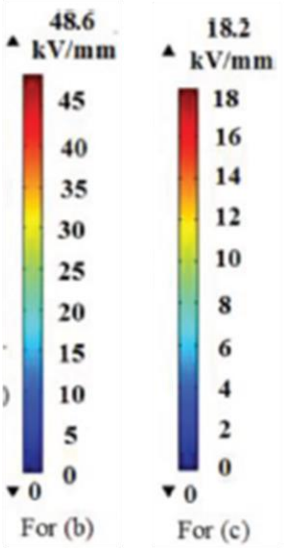

(c) E distribution with field grading layer

Fig. 1.8 Application of SiR/ZnO microvaristor composite as field grading layer in a 500 kV cable termination [31].

permittivity and conductivity. Spacers are made of epoxy resin filled with conventional fillers, such as alumina (Al_2O_3) or silica (SiO_2) fillers. These fillers are added in order to improve the mechanical and thermal properties, as well as to minimize the shrinkage during casting [6]. In addition, there are conducting fillers (e.g. carbon black, carbon nanotubes (CNT)), semiconducting fillers (e.g. SiC, ZnO microvaristors, antimony-tin oxide (ATO – SnO_2/Sb_2O_3)), and high permittivity particles (e.g. $SrTiO_3$, TiO_2, etc) [27]. Some of the common functional fillers that are used for electric field grading in DC devices are as follows.

1) Silicone Carbide (SiC)

SiC is a semiconducting filler that has been commonly used due to its high thermal conductivity, low thermal expansion coefficient and high chemical stability. It has nonlinear property due to the contact interfaces between adjacent fillers, however the nonlinearity is rather unstable since it is easily influenced by filler parameters (size, doping ratio), and environmental factors (humidity, pressure, pollution, abrasion, etc), which in turns affect the whole electrical properties of the composite material [32]. The used SiC powder usually has a few micrometers to a few tens of micrometers in particle size. Fig. 1.9 shows the resistivity and permittivity characteristics of micro-grain SiC/EPDM composite for different particle size [33].

In the past research of layered σ-FGM for AC application, SiC and Fe_3O_4 fillers that are used for electric field relaxation at the cable-end and the coil-end of the rotating machine [34-36], are investigated for its conductivity and permittivity characteristics, as shown in Fig. 1.10 [37]. Based on the conductivity range that they provide, and the stability of permittivity value against frequency, SiC fillers are then selected as the filler materials used in this research as well.

2) Zinc Oxide (ZnO)

Pure ZnO usually has to be processed into ZnO microvaristors first in order to possess the nonlinear characteristics. Its nonlinear behavior is dominated by the double (back-to-back) Schottky barrier over the adjacent ZnO grains inside each microvaristor particles [38]. Unlike SiC, the overall properties of ZnO-filled composite are affected by the treatment process, the matrix material, the packing arrangement of the particles, and the

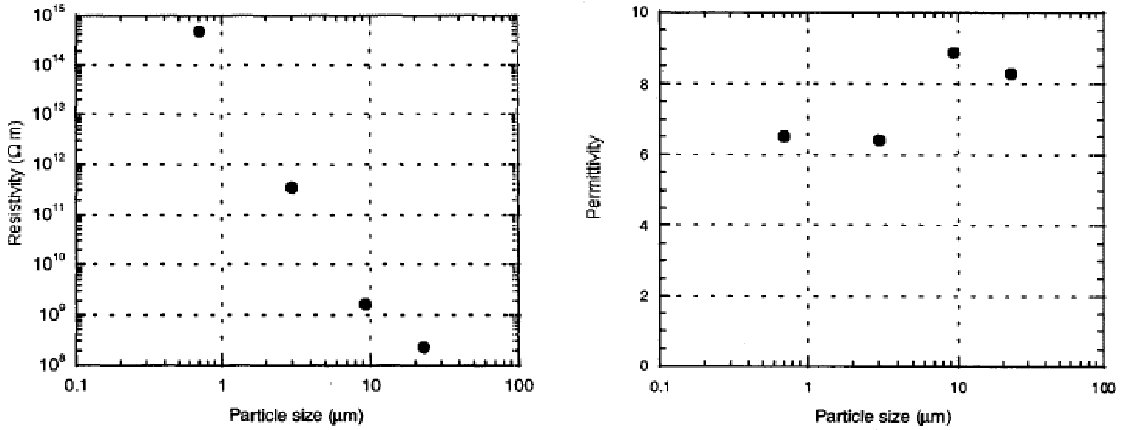

(a) DC Resistivity at E=2 kV/mm, and T=30°C.

(b) Permittivity at 10 V and f = 46 Hz.

Fig. 1.9 (a) Resistivity and (b) permittivity of 40 vol% green SiC/EPDM composite [33].

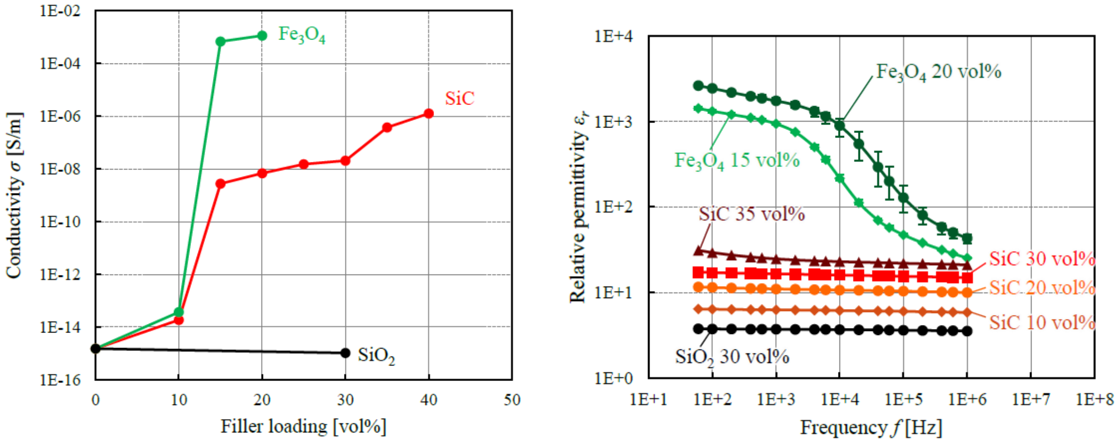

(a) DC Resistivity at E=1 kV/mm

(b) Permittivity at 1 V_{rms}

Fig. 1.10 (a) Conductivity and (b) permittivity of SiC and Fe_3O_4-filled epoxy composite [37].

contact between particles. Fig. 1.11 shows that it is possible to choose the nonlinear composite with certain switching field and nonlinear coefficient by adjusting the ZnO particle's size and shape. Currently ZnO is not widely used as SiC for applications on GIS/GIL spacers, due to the sedimentary problem of ZnO fillers in the matrix material, and that it usually requires larger filler contents with several tens of micrometers particles which can lead to poor mechanical property [31,32]. Nonetheless, it is applicable for coatings on the inner side of enclosure and triple junction in GIS/GIL [39].

3) Graphene Oxide (GO)

GO for electric field grading material is used in the sheet forms with low dimension and hence, can form stable conduction paths at considerably lower concentrations. It has characteristics of high dielectric constant, small loss factor, adjustable switching fields and saturation conductivity. Fig. 1.12 shows the conductivity characteristics of doped GO/polydimethylsiloxane (PDMS) composites with nonlinearity properties that unlike other fillers, can reach saturation condition [32,40].

1.3.2 Fabrication Technology

The use of nonlinear composite for electric field grading materials can be in the forms of surface coating or bulk doping. Several techniques regarding both forms will be shortly discussed as follows.

1) Dip coating method

Du *et al* fabricated nano-graphene-filled epoxy (EP/GR) coated insulators with whole side surface covered in the coatings as shown in Fig. 1.13 (a). The experiment results show that 0.1 wt% EP/GR coated insulator can increase the flashover voltage from ~25.9 kV (uncoated) to ~33.8 kV, as shown in Fig. 1.13 (b) [41].

Oishi *et al* fabricated σ-FGM with conductive layer where they can control the coating layer thickness by controlling the pulling speed of the dip coater. Fig. 1.14 shows the illustration of the fabrication process, sample appearance, and the flashover experiment results of σ-FGM. Flashover voltage of σ-FGM is improved by 10.3% compared to the uncoated insulator [42,43].

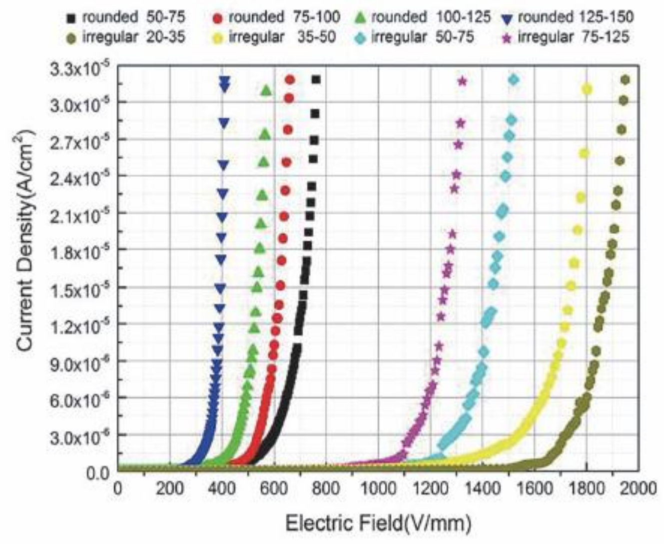

Fig. 1.11 J(E) characteristics of 46.5 vol% ZnO/SiR composites with different filler shape and size [31].

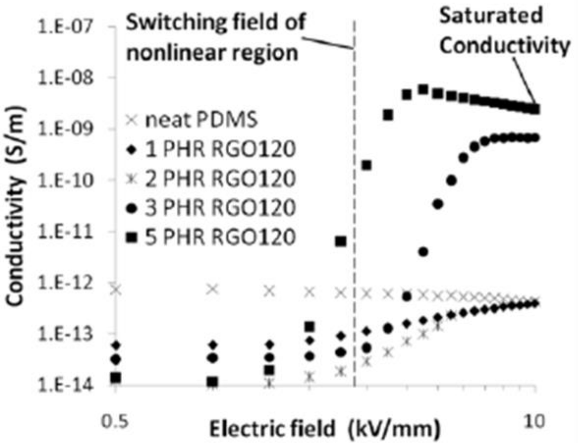

Fig. 1.12 Conductivity characteristics of GO/PDMS composite with different loading at 120°C [40].

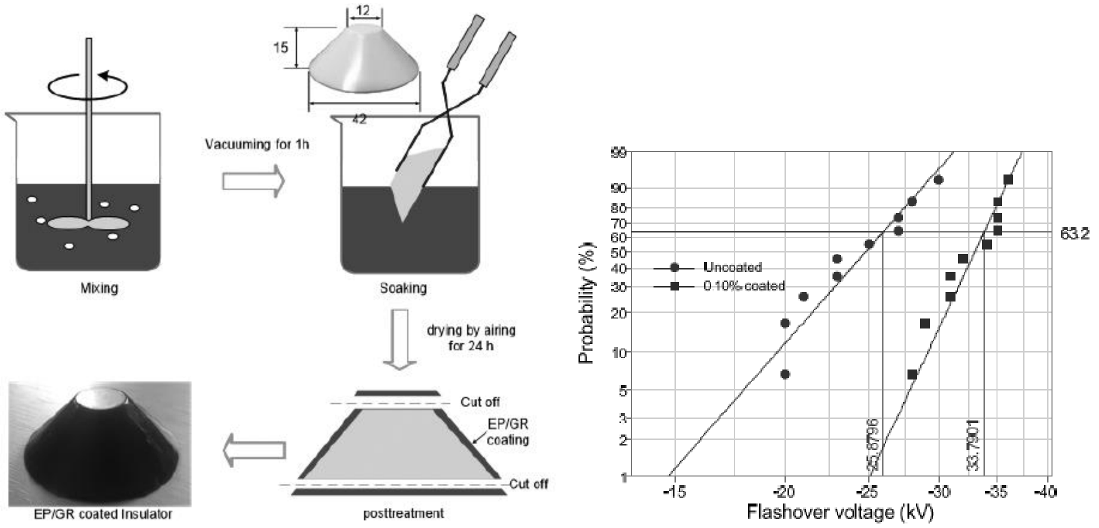

(a) (b)

Fig. 1.13 (a) Surface coating process and (b) weibull distributions of flashover voltages of the uncoated and EP/GR coated insulators [41].

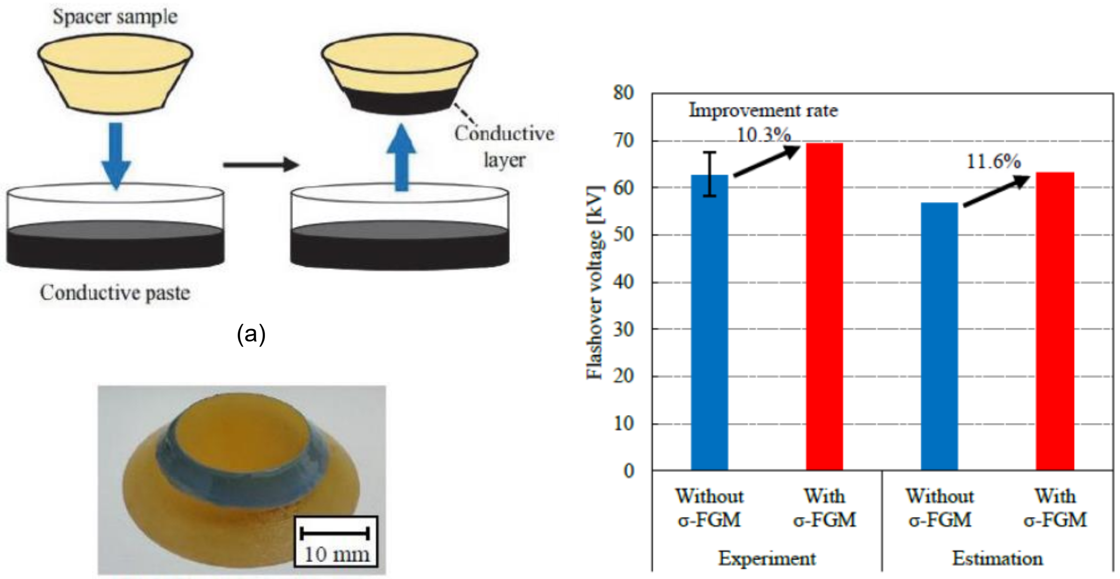

(a)

(b)

(c)

Fig. 1.14 (a) Dip coating process, (b) the sample appearance and (c) the flashover experiment results on SiC layered σ-FGM [42,43].

2) Magnetron sputtering method

Du et al then fabricated a surface functional gradient material (SFGM) using stratified magnetron sputtering to sputter ZnO onto the surface of GIS epoxy disk gasket, as shown in Fig. 1.15 [44].

3) 3D printing

3D printing method has been attempted to fabricate dielectric functionally graded insulation (d-FGI) using fused deposition modeling (FDM) technology which can use recyclable thermoplastic materials as printing raw materials and can produce almost any shape or geometry of objects [45]. Fig. 1.16 shows an example of spacer made of alumina/UV-cured resin composite by 3D printing [46]. However, it has a few disadvantages, e.g. voids are unavoidable to form which may lead to low mechanical strength, and there is maximum limit of filler contents for certain types of fillers that may result in weak or unoptimized electric field relaxation effect [45,47].

4) Flexible mixture casting (FMC) method

Ochiai *et al* fabricated a truncated cone-type and cone-type FGM spacers with continuously graded permittivity (ε-FGM) using flexible mixture casting (FMC) method. Fig. 1.17 shows the illustration of FMC method, the appearance of fabricated cone-type ε-FGM spacer, the permittivity distribution within the cone-type ε-FGM spacer. The 12% improvement rate of discharge inception voltage of the ε-FGM spacer is verified compared to the Uniform spacer [48,49].

1.4 FGM Application to GIS/GIL Spacers and Feasibility

In the past works [50-52], application of ε-FGM to a 245 kV-class AC GIS cone-type spacer has been developed by FMC fabrication method, containing $SrTiO_3$-filled epoxy composite as the high ε_r composite and SiO_2-filled epoxy composite as the low ε_r composite that bring about graded ε_r between 10 and 4, as shown in Fig. 1.18 [51]. Related to the downsizing of GIS, the target was to reduce the spacer diameter by 30% and the cross section by 50%. Fig. 1.19 (a) shows the electric field relaxation effect of ε-FGM spacer that can reduce the high electric field stress at the shield edges of both concave

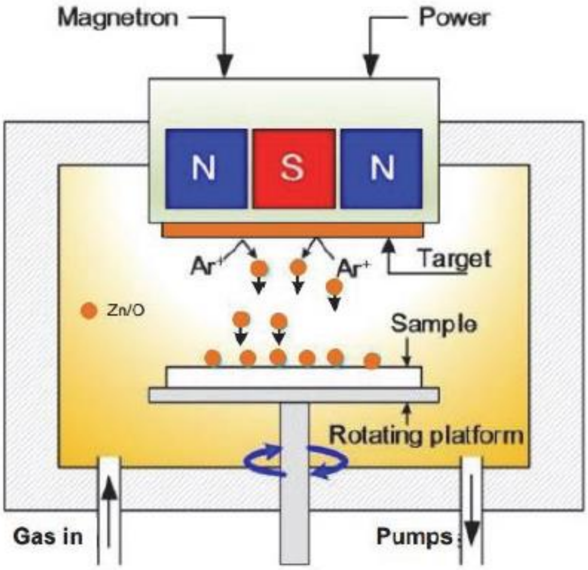

Fig. 1.15 Diagram of magnetron sputtering device [44].

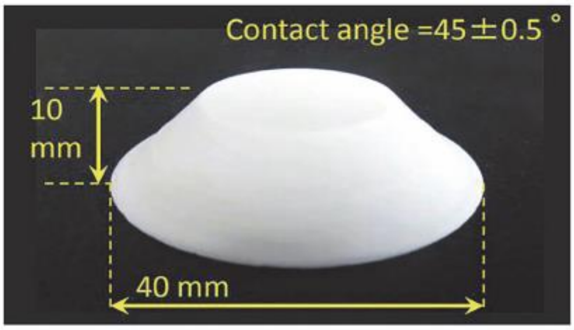

Fig. 1.16 Alumina/UV-cured resin composite conical spacer by stereolithographic 3D printing [46].

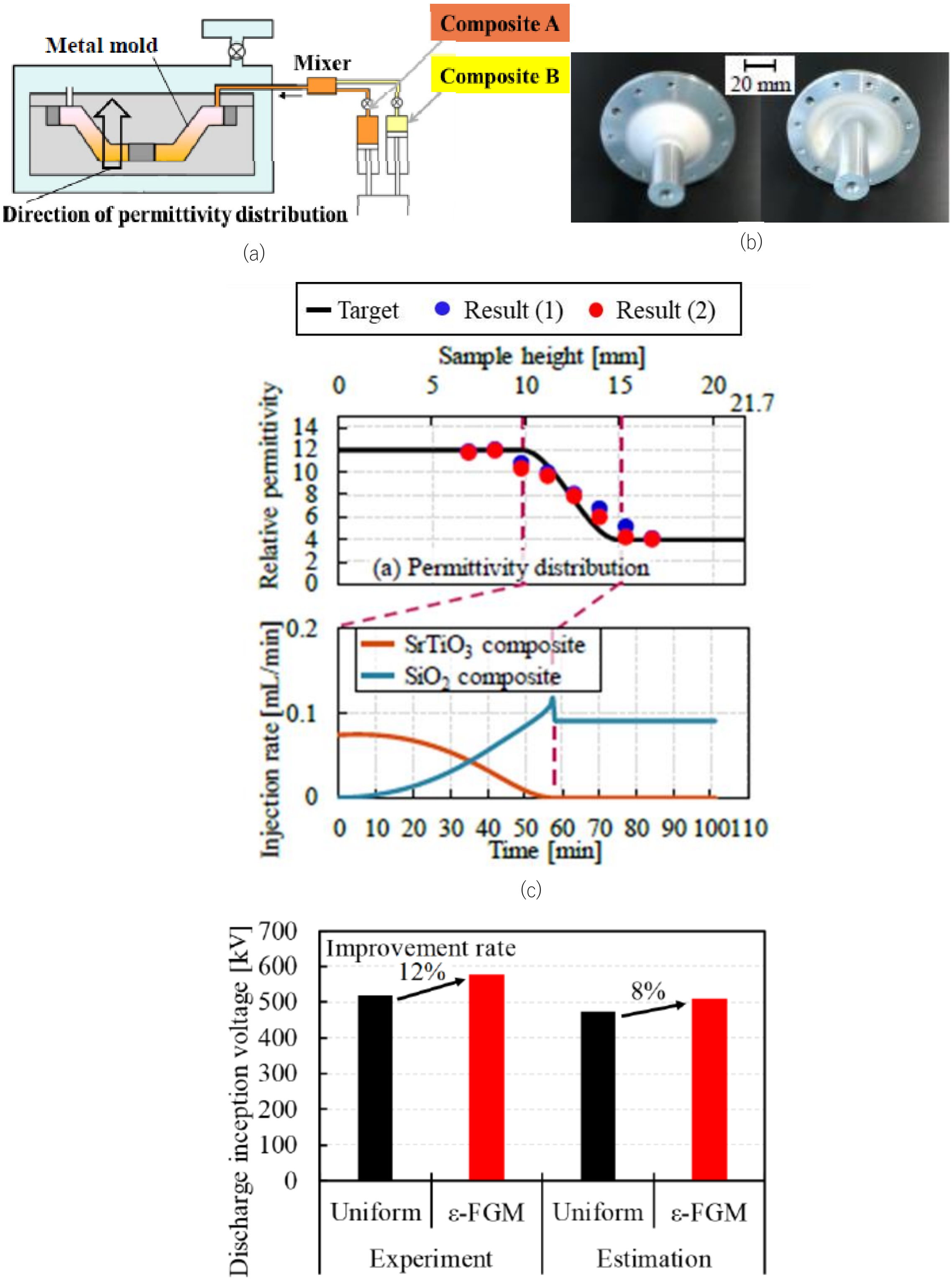

(a)

(b)

(c)

(d)

Fig. 1.17 (a) FMC method illustration, (b) fabricated cone-type ε-FGM spacer, (c) ε distribution and injection rate program to syringe pumps, and (d) discharge inception voltage experiment results [48].

and convex side, and distribute it to the middle parts of the spacer. The breakdown experiment results also show that the flashover voltages of ε-FGM spacer are verified to be higher than that of the conventional spacer by 28% at 0.6 MPa-abs of SF_6 gas pressure, as shown in Fig. 1.19 (b) [52].

Early investigation was also conducted on σ-FGM for a 320 kV HVDC GIS cone-type spacer model, where a saddle shaped (or U-shaped) distribution of $\sigma=10^{-15} – 10^{-14}$ S/m is formed longitudinally along the HV conductor, in comparison with the Uniform spacer with $\sigma=10^{-15}$ S/m, as shown in Fig. 1.20 (a). Fig. 1.20 (b) shows the electric field strength around the HV electrode on the concave surface of σ-FGM spacer is relaxed, and the high electric field strength around the HV electrode on the convex surface is also shifted away to the middle part of the spacer, compared to that of the Uniform spacer. This is because the potential burden around the spacer part near the HV electrode is reduced due to the high σ at those area, and shared or distributed toward the middle part with the lower σ. Fig. 1.20 (c) also shows the electric field relaxation effect around the Uniform and σ-FGM spacers when temperature distribution between HV conductor and GND enclosure (ΔT) is 0 and 70 K [53].

Nevertheless, the above case applies only for electric field grading under DC steady state (DC-SS). As previously mentioned in Section 1.2.1, in DC system, there are not only constant resistive electric fields that occur under DC-SS, but also time-varying capacitive electric fields that occur during switching to different voltage, e.g. DC-on, polarity reversal. In the same way as in AC GIS, the capacitive fields in DC GIS are also determined by permittivity. Therefore, in order to be able to respond to both types of electric fields under various DC operating conditions, it is necessary to apply FGM with combination of grading permittivity and conductivity (ε/σ-FGM) to DC GIS spacer.

1.5 Research Purpose and Thesis Structure

Coming from the background in the previous section, it can be concluded that the effectiveness of ε-FGM application to HVAC GIS spacer for electric field relaxation as well as for breakdown strength improvement has already been proven, which leads to high possibility to downsize the GIS. Furthermore, it is also feasible to apply the FGM concept with permittivity and/or conductivity distributions to HVDC GIS/GIL spacer.

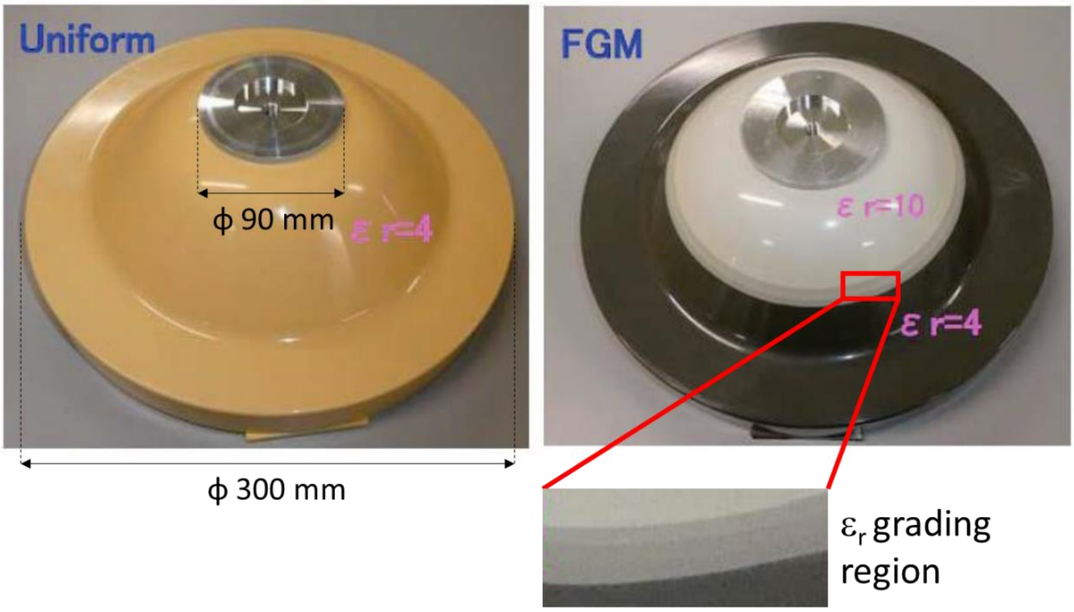

Fig. 1.18 Uniform and ε-FGM spacer for 245 kV-class AC GIS [51].

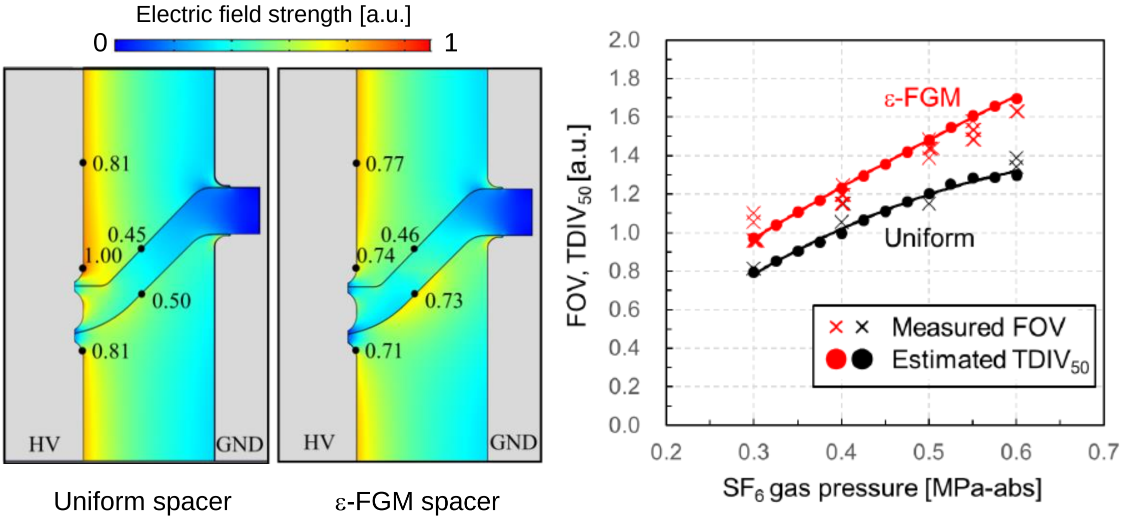

(a) (b)

Fig. 1.19 (a) Electric field relaxation effect and (b) FOV and $TDIV_{50}$ improvement of ε-FGM spacer for 245 kV-class AC GIS [52].

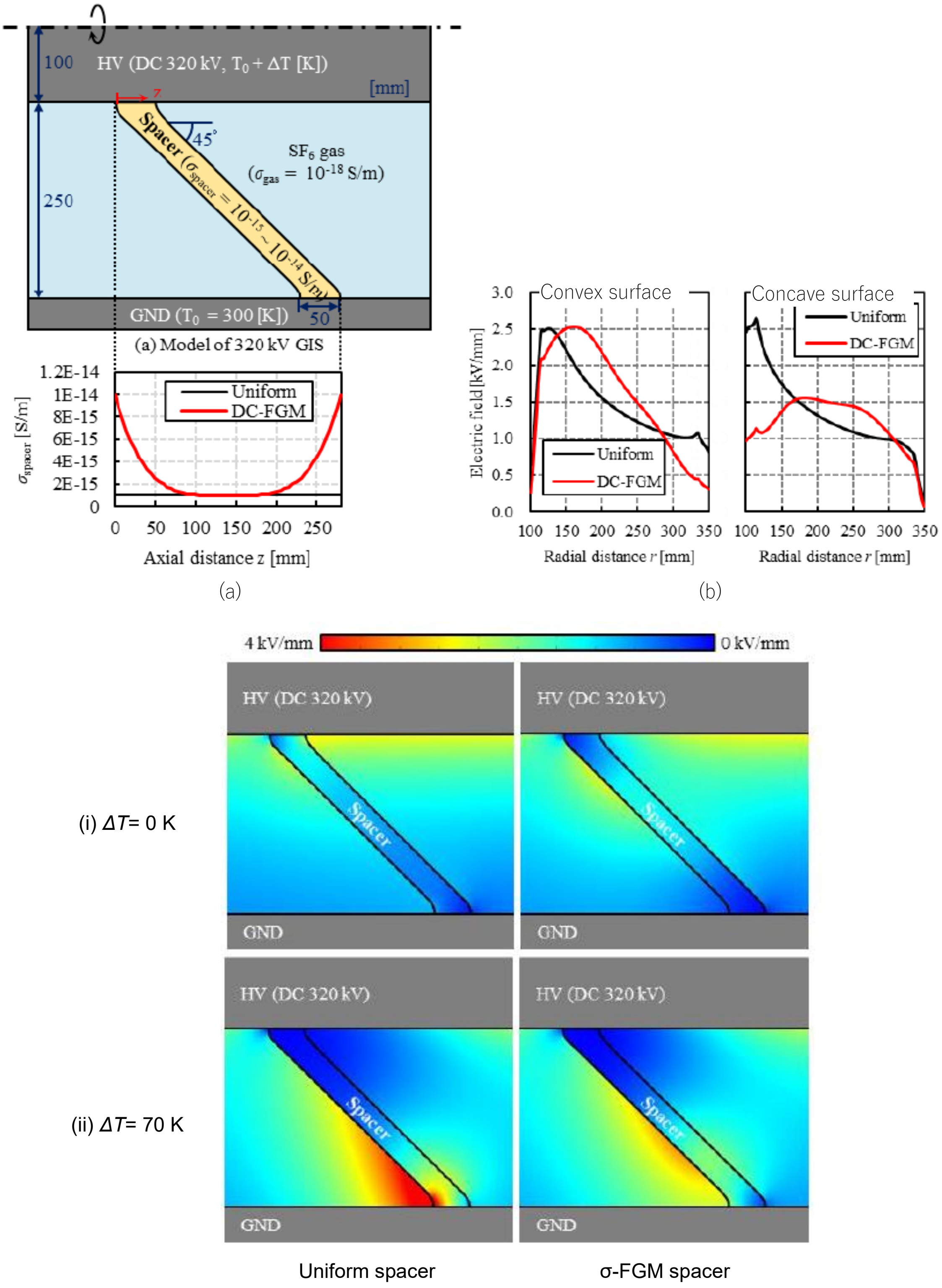

(a)

(b)

(c)

Fig. 1.20 (a) σ distribution of a HVDC GIS σ-FGM spacer model, (b) electric field strength along the spacer surfaces, and (c) electric field relaxation effect around the Uniform and σ-FGM spacers [53].

However, more investigations are required to conduct, such as the insulation performance under various DC operating conditions, the nonlinear materials to be used, the fabrication method, the breakdown tests, and so on. For that reason, those investigations are carried out in this research and the results are reported and discussed in this thesis.

Thus, the research purpose of this thesis is to evaluate the effectiveness of ε/σ-FGM under various DC operating conditions in consideration of temperature distributions.

Based on the above research background and purpose, the outline of each chapter in this dissertation is described as follows.

In Chapter 2, the concept of ε/σ-FGM is explained. Permittivity (ε) as well as conductivity (σ) characteristics of composite materials to be used in this research are discussed, including the sample fabrication methods, the σ and the ε measurement methods and the results. Multivariate analysis for different parameters, i.e. temperature, applied electric field strength, and filler contents is performed on the measurement data of σ and ε to obtain the characteristics of arbitrary composite material for ε/σ-FGM.

In Chapter 3, fundamental simulation on electric field grading of ε/σ-FGM for 320 kV HVDC GIS spacer model are discussed. Some types of ε and σ distributions are given to obtain the effective ε/σ distribution for electric field relaxation under various DC operating conditions, i.e. DC steady state (DC-SS), DC polarity reversal (DC-PR), DC-on, and superimposed positive and negative lightning impulse (LI) on DC-SS. In this simulation, the conductivity characteristics of ε/σ-FGM spacer were based on the reference data with temperature and electric field dependency of typical epoxy resin. Temperature effect is also investigated for each simulation condition.

In Chapter 4, toward practical application, the actual measured ε characteristics of $SrTiO_3$-filled epoxy composite and σ characteristics of SiC-filled epoxy composite in Chapter 2 are applied to ε/σ-FGM for a scaled model of HVDC GIS/GIL spacer. Then, electric field simulations are conducted for an independently controlled ε and σ distribution of ε/σ-FGM spacer, in comparison to the Uniform spacer, under various DC operating conditions. Furthermore, Theoretical Discharge Inception Voltage ($TDIV_{50}$) is also calculated based on the Volume-Time theory for positive lightning impulse voltage. $TDIV_{50}$ of ε/σ-FGM spacer is compared with that of Uniform spacer under several values of SF_6 gas pressures.

Chapter 5 summarizes the results obtained in this research.

References

[1] Z. Liu, "Global Energy Development: The Reality and Challenges," in *Global Energy Interconnection*, Academic Press, 2016, pp. 1-64.

[2] "World Population Review," 2022. [Online]. Available: https://worldpopulationreview.com/country-rankings/electricity-consumption-by-country.

[3] C. Horwill, N. M. Macleod, R. E. Bonchang, D. Castagna, M. Artenstein and M. Croce, "A new 500MW frequency converter station to exchange power between Uruguay and Brazil," in *2011 IEEE/PES Power Systems Conference and Exposition*, Phoenix, AZ, USA, 2011, pp.1-6.

[4] M. Ardelean and P. Minnebo, "HVDC Submarine Power Cables in the World," European Union, Netherlands, 2015.

[5] U. Riechert, U. Straumann, R. Gremaud and M. Callavik, "Compact gas-insulated systems for high voltage direct current transmission: design and testing," in *IEEE PES Transmission & Distribution Conference & Exposition*, Dallas, USA, 2016, pp.1-5.

[6] N. Zebouchi and M. A. Haddad, "A Review on real-size epoxy cast resin insulators for compact high voltage direct current gas insulated switchgears (GIS) and gas insulated tranmision lines (GIL) - Current achievements and envisaged research and development," *Energies,* vol. 13, no. 23, pp. 1-25, 2020.

[7] Y. Luo, J. Tang, Z. Pan and C. Pan, "How temperature and pressure affect the electric field distribution in HVDC GIS/GIL: A numerical study," *IEEE Transactions on Dielectrics and Electrical Insulation,* vol. 28, no. 4, pp. 1334-1342, 2021.

[8] M. Tenzer, K. Juhre, M. Benhe and D. Imamovic, "Compact gas insulated systems for HVDC applications," in *CIGRE HVDC and Power Electronics International Colloquium*, Agra, India, 2015, no.26, pp.1-7.

[9] N. A. V. Behravesh, "New Comparison of HVDC and HVAC Transmission System," *International Journal of Engineering Innovation & Research (IJEIR),* vol. 1, no. 3, pp. 300-304, 2012.

[10] CIGRE Working Group B4.44, "HVDC Environmental Planning Guidelines," *CIGRE Technical Brochures No. 508,* Oct 2012.

[11] Y. Tanaka, A. Kawahara and M. Sanpe, "Recent technology in the Kii Channel DC 500 kV Link Project - converter station equipment and technology," *IEEJ Transactions on Fundamentals and Materials,* vol. 120, no. 11, pp. 959-964, 2000.

[12] Y. Makino, "The trend of DC Transmission (translated from Japanese)," *OHM electrical magazine,* pp. 13-19, Feb 2018.

[13] C. Li, C. Lin, J. Hu, W. Liu, Q. Li, B. Zhang, S. He, Y. Yang, F. Liu and J. He, "Novel HVDC spacers by adaptively controlling surface charges - Part 1: Charge transport and control strategy," *IEEE Transactions on Dielectrics and Electrical Insulation,* vol. 25, no. 4, pp. 1238-1245, 2018.

[14] B. M. Buchholz, D. Povh and D. Retzmann, "Stability analysis for large power system interconnections in Europe," in *2005 IEEE Russia Power Tech*, St. Petersburg, Russia, 2005, pp.1-7.

[15] L. Michi, G. Donnini, C. Giordano, F. Scavo, E. Luciano, B. Aluisio, C. Vergine, M. Pompili, S. Lauria, L. Calcara and A. L'Abbate, "New HVDC technology in Pan-European power system planning," in *2019 AEIT HVDC International Conference (AEIT HVDC)*, Florence, Italy, 2019, Session 4.5, pp.1-6.

[16] D. Echternacht, D. Heuberger, C. Breuer, C. Linnemann and A. Moser, "Advantageous Positions for HVDC Terminals in Europe," in *2013 IEEE Energytech*, Cleveland, OH, USA, 2013, pp.1-5.

[17] H. Meinecke, "High voltage gas insulated switchgear: an overview," in *IEE Colloquium on GIS (Gas-Insulated Switchgear) at Transmission and Distribution Voltages*, Nottingham, UK, 1995, pp.3/1-3/8.

[18] M. Hering, J. Speck, K. Backhaus, S. Großmann and U. Riechert, "Capacitive-resistive transition in gas insulated DC systems under the influence of particles on the insulator surface," in *the 19th International Symposium on High Voltage Engineering (ISH)*, Pilsen, Czech Republic, 2015, no.157.

[19] U. Riechert, U. Straumann and R. Gremaud, "Compact Gas-insulated Systems for High Voltage Direct Current Transmission: Basic Design," in *IEEE PES Transmission & Distribution Conference & Exposition*, Dallas, USA, 2016, pp.1-5.

[20] LS ELECTRIC, *Gas Insulated Switchgear,* 2020.

[21] H. Koch and M. Hopkins, "Overview of gas insulated lines (GIL)," in *IEEE Power Engineering Society General Meeting*, San Fransisco, USA, 2005, vol.1, pp.940-944.

[22] G. Myhre, D. Shindell, F.-M. Bréon, W. Collins, J. Fuglestvedt, J. Huang, D. Koch, J.-F. Lamarque, D. Lee, B. Mendoza, T. Nakajima, A. Robock, G. Stephens, T. Takemura and H. Zhang, "Anthropogenic and Natural Radiative Forcing," in *Climate Change 2013: The Physical Science Basis*, Cambridge, Cambridge University Press, 2013, pp. 659-740.

[23] K. Okamoto, N. Hayakawa, M. Hikita, H. Okubo, K. Kato, N. Osawa, K. Watanabe and K. Adachi, "Distinctive Downsizing of Cone-Type Insulating Spacer for 245 kV Class GIS by Functional

Insulating Materials," *CIGRE Science and Engineering,* pp. 120-133, Feb 2022.

[24] M. Kurimoto, "Polymer Composites for Electric Stress Control," in *Polymer Composites for Electrical Engineering, First Edition*, John Wiley & Sons Ltd., 2022, pp. 179-189.

[25] N. Zebouchi, H. Li and M. A. Haddad, "Development of Future Compact and Eco-friendly HVDC Gas-Insulated Systems: Shape Optimization of a DC Spacer Model and Novel Materials Investigation," *Energies,* vol. 13, no. 12, pp. 1-14, 2020.

[26] T. Hasegawa, K. Yamaji, M. Hatano, F. Endo, T. Rokunohe and T. Yamagiwa, "Development of insulation structure and enhancement of insulation reliability of 500 kV DC GIS," *IEEE Trans. Power Deliv.,* vol. 12, no. 1, pp. 194-202, 1997.

[27] CIGRE WG D1.56, "Field grading in electrical insulation systems," CIGRE Technical Brochure No. 794, 2020.

[28] B. Lutz, K. Juhre and D. Imamovic, "Long-term performance of solid insulators in gas insulated systems under HVDC stress," in *The 19th International Symposium on High Voltage Engineering (ISH)*, Pilsen, Czech Republic, 2015, no.530.

[29] A. Küchler, High voltage engineering Fundamentals-Technology-Applications, Berlin, Germany: Springer Vieweg, 2017.

[30] N. Hayakawa, Y. Miyaji, H. Kojima and K. Kato, "Electric field reduction by functionally graded materials (FGM) with permittivity and conductivity distribution," in *2016 IEEE Conference on Electrical Insulation and Dielectric Phenomena (CEIDP)*, Toronto, Canada, 2016, pp.627-630.

[31] X. Yang, X. Zhao, J. Hu and J. He, "Grading electric field in high voltage insulation using composite materials," *IEEE Electrical Insulation Magazine,* vol. 34, no. 1, pp. 15-25, Jan-Feb 2018.

[32] W. Pan, Y. Wang, H. Ding, E. Shen, Z. Zhang, X. Yang, Z. Wang and S. Akram, "Nonlinear Materials Applied in HVDC Gas Insulated Equipment: From Fundamentals to Applications," *IEEE Transactions on Dielectrics and Electrical Insulation,* vol. 28, no. 5, pp. 1588-1603, 2021.

[33] C. Onneby, E. Martensson, U. Gafvert, A. Gustafsson and L. Palmqvist, "Electrical properties of field grading materials influenced by the silicon carbide grain size," in *Proceedings of the 2001 IEEE 7th International Conference on Solid Dielectrics (ICSD)*, Eindhoven, Netherlands, 2001, pp.43-45.

[34] L. Donzel, F. Greuter and T. Christen, "Nonlinear Resistive Electric Field Grading Part 2: Materials and Applications," *IEEE Electrical Insulation Magazine,* vol. 27, no. 2, pp. 18-29, 2011.

[35] A. Roberts, "Stress Grading for High Voltage Motor and Generator Coils," *IEEE Electric Insulation Magazine,* vol. 11, no. 4, pp. 26-31, 1995.

[36] 岡本徹志, 川. 原誠, 山田利光, 井上良之, 中村修平, "2 粒子系複合体のパーコレーション現象と電界緩和材料の開発," *電気学会論文誌A,* vol. 126, no. 10, pp. 1004-1012, 2006.

[37] 大石 涼太, "導電率傾斜機能材料によるガス絶縁電力機器の電界制御技術に関する研究

",名古屋大学 修士学位論文, 2018, pp. 19-28.

[38] N. Riahi-Noori, "Comparison of electrical properties of zinc oxide varistors manufactured from micro and nano ZnO powder," *Journal of Ceramic Processing Research,* vol. 12, no. 6, p. 752–755, 2011.

[39] Q. Shao, W. Sima, P. Sun, M. Yang, H. Xu and Z. Yin, "A novel nonlinear conductive ZnO micro-varistor/epoxy resin composite film for metallic particle deactivation in DC GIL," *IEEE Transactions on Dielectrics and Electrical Insulation,* vol. 27, no. 2, pp. 675 - 683, 2020.

[40] Z. Wang, J. K. Nelson, H. Hillborg, S. Zhao and L. S. Schadler, "Nonlinear conductivity and dielectric response of graphene oxide filled silicone rubber nanocomposites," in *2012 Annual Report Conference on Electrical Insulation and Dielectric Phenomena*, Montreal, Canada, 2012, pp.40-43.

[41] B. X. Du, H. C. Liang and J. Li, "Surface Coating Affecting Charge Distribution and Flashover Voltage of Cone-type Insulator under DC Stress," *IEEE Transactions on Dielectrics and Electrical Insulation,* vol. 26, no. 3, pp. 706-713, 2019.

[42] R. Oishi, H. Kojima, K. Kato and N. Hayakawa, "Electric field relaxation effect of Functionally Graded Materials (FGM) with conductive multilayer coating," in *2017 IEEE Conference on Electrical Insulation and Dielectric Phenomenon (CEIDP)*, Fort Worth, USA, 2017, pp.46-49.

[43] 大石 他, "導電率傾斜機能材料 (σ-FGM)による 沿面放電電圧向上効果," in *電気学会全国大会*, 6-010, 2018.

[44] G. Wang, T. Wang, W. Zhu, M. Fu, J. Li, H. Liang, Z. Ran and B. Du, "Surface Functional Graded Material Considered for DC Gas-Insulated Pipeline," in *2019 IEEE Conference on Electrical Insulation and Dielectric Phenomena (CEIDP)*, Richland, USA, 2019, 2C-7, pp.222-225.

[45] H.-Y. Yin, W.-D. Li, Y.-C. Zhang, C. Wang, Z.-H. Jiang and G.-J. Zhang, "Characterization of Polypropylene/ Titatium Dioxide Composites used for 3D Printing of Dielectric Functionally Graded Insulators," in *22nd International Symposium on High Voltage Engineering (ISH)*, [hybrid], 2021, no. 947, pp.1-5.

[46] M. Kurimoto, Y. Yamashita, H. Ozaki, T. Kato, T. Funabashi and Y. Suzuoki, "3D printing of conical insulating spacer using alumina /UV-cured-resin composite," in *2015 IEEE Conference on Electrical Insulation and Dielectric Phenomena (CEIDP)*, Ann Arbor, USA, 2015, 6A-3, pp.463-466.

[47] D. J. Park, J. Y. Shim, J. H. Son, J. Deitschun and V. Zoellmer, "Electric Field Relaxation by Functionally Graded Insulating Materials in GIS," in *CIGRE Session 48*, Paris, France, 2020, D1-307, pp.1-7.

[48] 落合 健太, "可変配合注型法による誘 電率傾斜機能材料の作製とガス絶縁電力機器への適用に関する研究", 名古屋大学大学院工学研究科 修士論文, 2018, pp. 39-58.

[49] 落合 他, "可変配合注型法による誘電率傾斜機能材料の作製および放電開始電圧向上効

果," in *電気学会電力・エネルギー部門大会*, 363, 2018.

[50] K. Adachi, H. Muto, K. Okamoto, Y. Hoshina and N. Fujimoto, "Development of New Types of Insulators for Electric Power Apparatuses Using Nanocomposites and Functionally Graded Materials," in *2020 IEEE 3rd International Conference on Dielectrics (ICD)*, Valencia, Spain, 2020, pp.317-320.

[51] N. Hayakawa, K. Kato, M. Hikita, H. Okubo, K. Watanabe, K. Adachi and K. Okamoto, "Development of Cone-Type FGM Spacer for Actual Size GIS," in *2020 IEEE Conference on Electrical Insulation and Dielectric Phenomena (CEIDP)*, East Rutherford, USA, 2020, pp.255-258.

[52] N. Hayakawa, Y. Miyazaki, H. Kojima, K. Kato, H. Okubo, K. Adachi and K. Okamoto, "Flashover voltage estimation of cone-type GIS spacer with permittivity graded materials (ε-FGM) by Volume-Time theory in consideration with conductor surface roughness in SF6 gas," in *22nd International Symposium on High Voltage Engineering (ISH)*, no.705, *online*, 2021.

[53] N. Hayakawa, R. Oishi, H. Kojima, K. Kato and N. Zebouchi, "Electric field grading by Functionally graded materials (FGM) for HVDC gas insulated power apparatus," in *2018 IEEE Conference on Electrical Insulation and Dielectric Phenomena (CEIDP)*, Cancun, Mexico, 2018, 5-3, pp.309-312.

Chapter 2 Concept and Material Characteristics of Functionally Graded Materials (FGM) for DC Application

2.1 Introduction

After the successful applications of functionally graded materials with graded permittivity (ε-FGM) and with conductivity (σ-FGM) to AC GIS spacers [1-6], the idea has now started to expand to DC applications [7]. Some researchers have evaluated the insulation performance of field grading materials for DC applications in the form of bulk doping with fixed concentrations of conducting or semiconducting fillers [8-10]. However, research on functionally grading materials with continuously graded conductivity is still limited. Therefore, this dissertation proposes the concept of σ-FGM and evaluation method of insulation performance on HVDC GIS spacer. This chapter discusses the concept of σ-FGM and the preliminary steps of material characteristics investigation of the used composite, i.e. the permittivity and the conductivity characteristics of SiC- and $SrTiO_3$-filled epoxy composites.

2.2 σ-FGM Concept

In Section 1.2.1, it has been discussed about capacitive and resistive field distribution and the derivation from Maxwell's equations leading to the final equation (1.4). The equation suggests that in an insulation system, capacitive (AC) field distribution is determined by the insulating material's permittivity (ε), while resistive (DC) field distribution is determined by the material's conductivity (σ). Under AC applications where time-varying fields present, only permittivity of the material needs to be considered. Thus, controlling the electric distribution around AC GIS/GIL spacer can be done by modifying the permittivity distribution of the spacer's bulk.

Nevertheless, in DC operating voltages, both constant voltage stress as well as time-varying voltage stress occur, as illustrated in Fig. 2.1. Hence, both capacitive and resistive field distributions also present within the insulation medium, depending on the operation modes that take place. At the turn on of DC voltage, time-varying capacitive fields occur. As time passes, resistive fields take over toward DC steady state (DC-SS) at the same time capacitive fields diminish. Then, the presence of both capacitive and resistive fields at the same time can be found at DC polarity reversal (DC-PR) and turn off. Moreover, apart from the regular operating conditions, mixed electric fields also occur under superimposed lightning impulse (LI) voltage on DC-SS that can take place during operation or during tests before installation.

Considering these phenomena, in order to control the electric field distributions in the insulation system of a HVDC GIS/GIL, the FGM application to the spacer should incorporate both ε and σ grading, which from now on will be called as ε/σ-FGM. An example of this scheme is also illustrated in Fig. 2.2. ε/σ-FGM is built by combining (in principle) two types of composites (the high ε and σ composite and the low ε and σ composite) in such a way that ε and σ are graded spatially in certain types of distribution. For example, Fig 2.2 shows both U-type ε and σ distributions of ε/σ-FGM spacer (b), in comparison with the Uniform spacer that has constant ε and σ (a).

In practical, the functional fillers with both high ε and σ characteristics are rarely found. So, if two composites combination are sufficient for AC ε-FGM spacer, for DC ε/σ-FGM spacer we may have to mix three types of composites: the high ε composite, the high σ composite, and the low ε and σ composite. Moreover, combining three types of composites also allows us to have independent ε and σ distribution, that can be realized by FMC fabrication method.

2.3 Bulk Sample Fabrication

Toward the practical application of ε/σ-FGM spacer to HVDC GIS/GIL, it is necessary to investigate the actual insulating material properties, which in this case are the permittivity and the electrical conductivity.

2.3.1 Materials

In order to investigate the effect of SiC filler contents to ε and σ characteristics, three types of SiO_2-filled epoxy-based bulk samples, each containing 0, 5, and 10 vol% SiC filler, are fabricated, where the total filler contents of SiC and SiO_2 is 50 vol% of the total

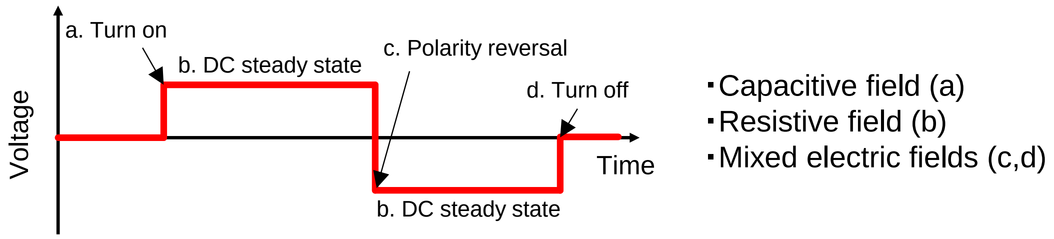

Fig. 2.1 Voltage pattern in HVDC power apparatus

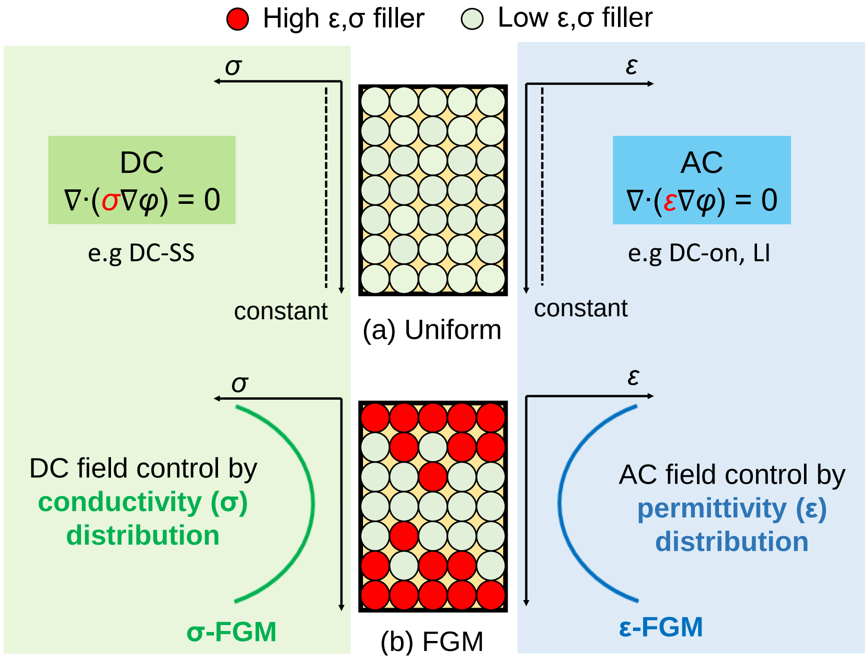

Fig. 2.2 Electric field control by permittivity and conductivity distributions of the insulating material

Table 2.1 Material properties of epoxy resin

Base material	Specific gravity [g/ml]	Chemical structure
Epoxy	1.17	Bisphenol-A resin
Hardener	1.21	3 or 4- methyl-1,2,3,6-tetrahydrophthalic anhydride
Hardening accelerator	0.94	1-isobutil-2-methylimidazole

Table 2.2 Specifications of filler particles

Filler material	Specific gravity [g/ml]	Mean diameter [µm]
SiC	3.16	3.71
SiO_2	2.21	9.98
$SrTiO_3$	5.13	1.00 – 1.50

epoxy-composite. Tables 2.1 and 2.2 show the material properties of the base epoxy resinand fillers.

2.3.2 Fabrication Method

First of all, bulk samples of different filler contents are fabricated according to the following steps.

a) Adding hardener and hardening accelerator to the base resin (epoxy), followed by mixing the resin using a planetary mixing machine for about 3 minutes,
b) Adding filler material to the epoxy resin in a), then stirring it using planetary mixing machine for about 10 minutes. Adding and mixing filler materials to the composite should be done one at a time for each different filler, to result in better dispersed fillers in the composite,
c) Degassing the composite in a vacuum chamber to remove air bubbles for about 10 minutes, and
d) Curing the composite in an oven at constant temperature of 100 °C for 6 hours.

In order to measure the material properties of the prepared samples, the samples are prepared into thinner flat pieces. The thinner the sample's thickness is, the wider range of electric field we get for investigating the conductivity characteristics, as electric field is determined by applied voltage divided by sample thickness ($E=V/d$). The bulk samples are prepared in two different ways, which are by bulk cutting method for permittivity measurement and by parallel glass pressing method for conductivity measurement.

2.3.2.1 Bulk Cutting

The after-curing bulk samples is sliced in the radial direction by cutting machine, as shown in Fig. 2.3, to a thickness of 0.5 mm. At current stage, setting the thickness target smaller than 0.5 mm would result in poor uniformity of thickness throughout the bulk sample.

2.3.2.2 Parallel Glass Pressing

This method uses two 10 x 10 cm square plate glasses that are put in parallel with the liquid composite (before curing) poured onto one of the glass surfaces beforehand. Fig.

2.4 shows the images of this process as also described in the following steps.

a) Attach adhesive PTFE or PI tapes with the desired thickness on the four edges of one glass (see Fig. 2.4 (a)),
b) Cover the glass surface including the taped parts, as well as one side of the other glass with mold releasing agent, then the glasses are dried in the oven at 100 °C for 10 hours,
c) Pour a small amount of the degassed liquid composite onto the middle surface of the taped glass (see Fig. 2.4 (b)),
d) Put carefully another glass without tape onto the top of the glass with composite on it in parallel, as shown in Fig. 2.4 (c), until the composite liquid spread by itself forming a thin volume of composite. At this stage, if voids are clearly formed, we should immediately separate the glass, wipe the composite from the glass, clean the glass, and redo the steps all over again.
e) Secure the glasses in parallel with double clips at four sides, as shown in Fig. 2.4 (d).
f) Proceed to the curing process.

The advantage of this method is that we can make thin samples up to 0.11 mm-thick following the tape's thickness. However, it is difficult to control the voids that are formed during the glass pressing, so making several samples of the same type (same filler contents) at once is recommended.

2.4 Conductivity Measurement of SiC-filled Epoxy Composite

2.4.1 Conductivity Measurement Method

The conductivity (σ) of insulating materials is dependent on the temperature (T) and the electric field strength (E), which can be expressed by equation (2.1) [11-12]:

$$\sigma(T, E) = \sigma_0 \exp\left(-\frac{W}{kT}\right) \exp(aE) \tag{2.1}$$

where σ_0 is the specific conductivity constant in S/m, k is the Boltzmann constant, and W and a are the temperature and electric field-dependency coefficients, respectively.

In order to comply with equation (2.1), the conductivity of each sample is measured using double-ring electrode system of JIS C 2170 under varying applied voltages of 10 V, 100 V, 500 V and 1000 V (E = 0 ∼10 kV/mm) and at different temperatures (T = 303 K, 333 K, and 353 K), according to JIS C2139-3-1-2018 or IEC 62631-3-4 [13-15]. Before

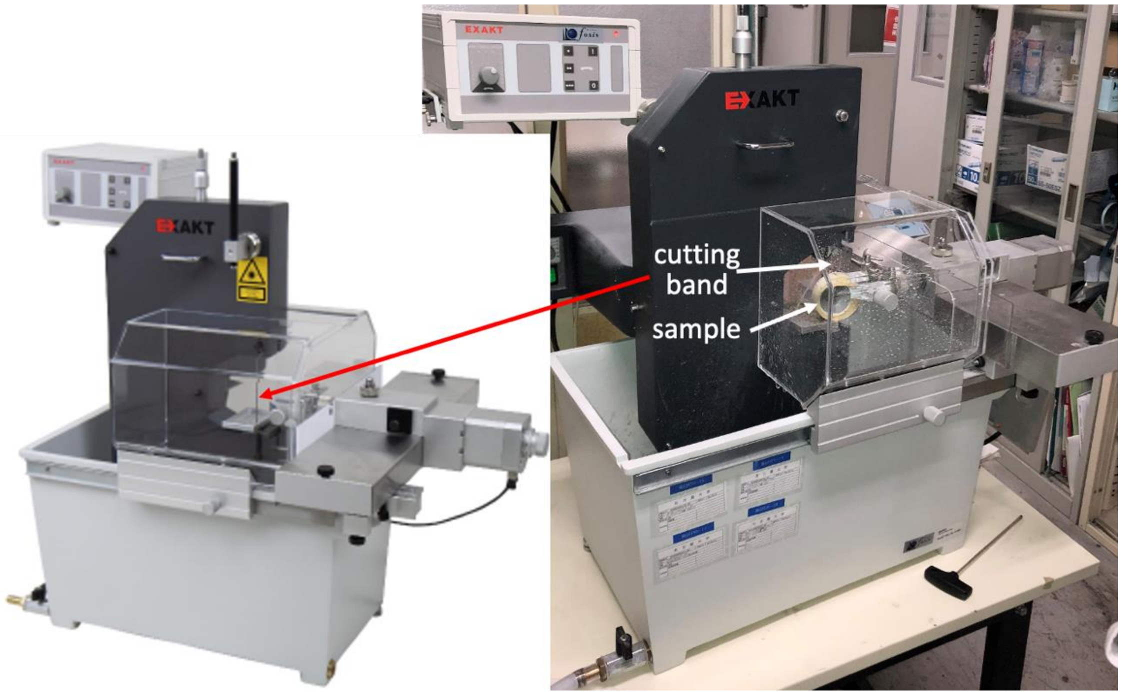

Fig. 2.3 Cutting machine

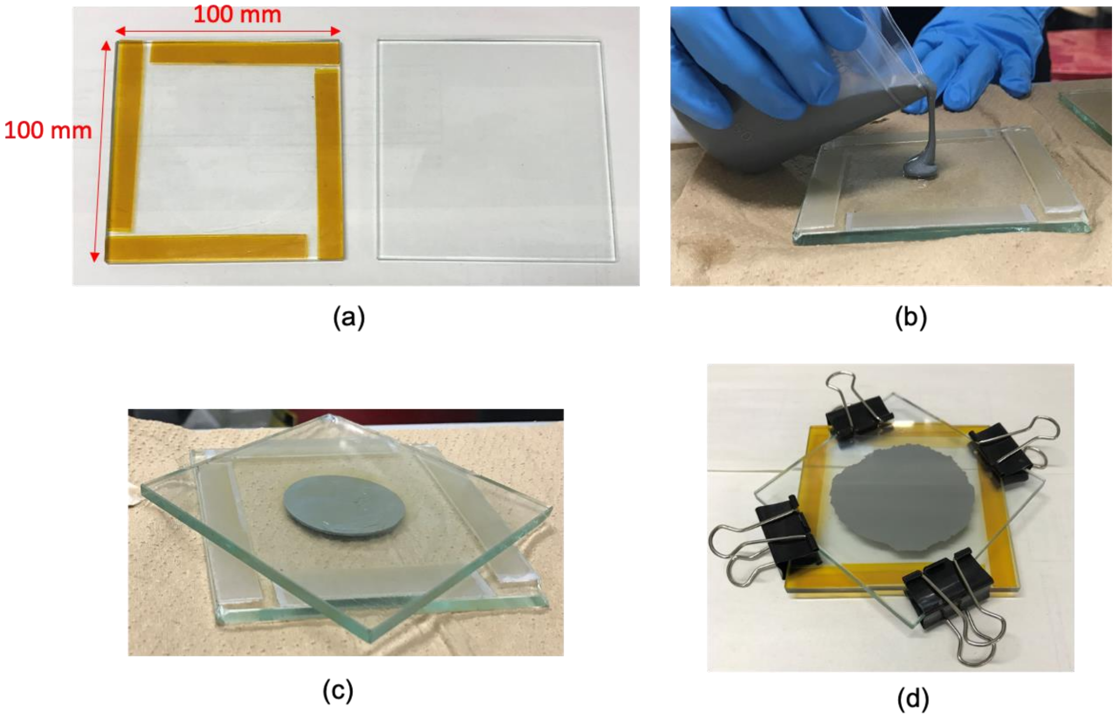

(a)

(b)

(c)

(d)

Fig. 2.4 Images of sample fabrication using parallel glass pressing measurement takes place, conductive Ag paste is painted on both sides of each sample`s surface and dried in the oven at 100°C for 5 minutes (for each side), as shown in Fig. 2.5, in order to fit the electrode system during measurement. Fig. 2.6 shows the electrode system as well as the measurement circuit. At each applied voltage, the measured current decreases over time, and until steady state is reached, the current values at 1, 10, 20, 30, 40, and 50 minutes since voltage application are recorded. Afterward, the conductivity value is calculated by equation (2.2):

$$\sigma = \frac{I}{V} \cdot \frac{d}{S} \tag{2.2}$$

where I is the steady state current flowing through the main electrode in A, V is the applied voltage in V, d is the sample thickness in m, and S is the area of the main electrode in m^2.

2.4.2 Conductivity Measurement and Multivariate Analysis Results

Fig. 2.7 shows the temperature- and electric field-dependent conductivity measurement results of SiC-filled epoxy composite. The markers in Fig. 2.7 show σ measurement results of 0 vol% (black), 5 vol% (red), and 10 vol% (blue) SiC-filled epoxy composites at 303 K, 333 K, and 353 K (different marker types).

Afterwards, multivariate analysis is performed to the σ measurements' data with the associated E and T values according to equation (2.1), which then reveals the dependency

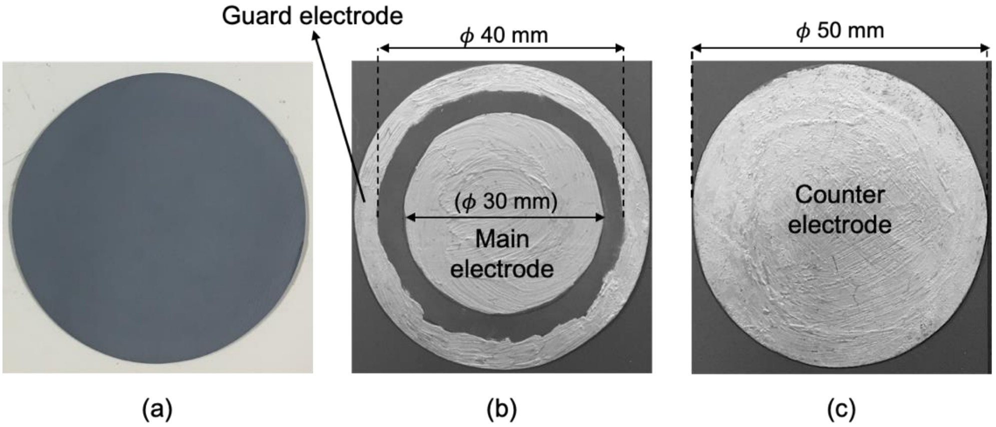

Fig. 2.5 Bulk sample appearance: (a) before painted with Ag paste, (b) after painted with Ag paste (front side), and (c) after painted with Ag paste (back side)

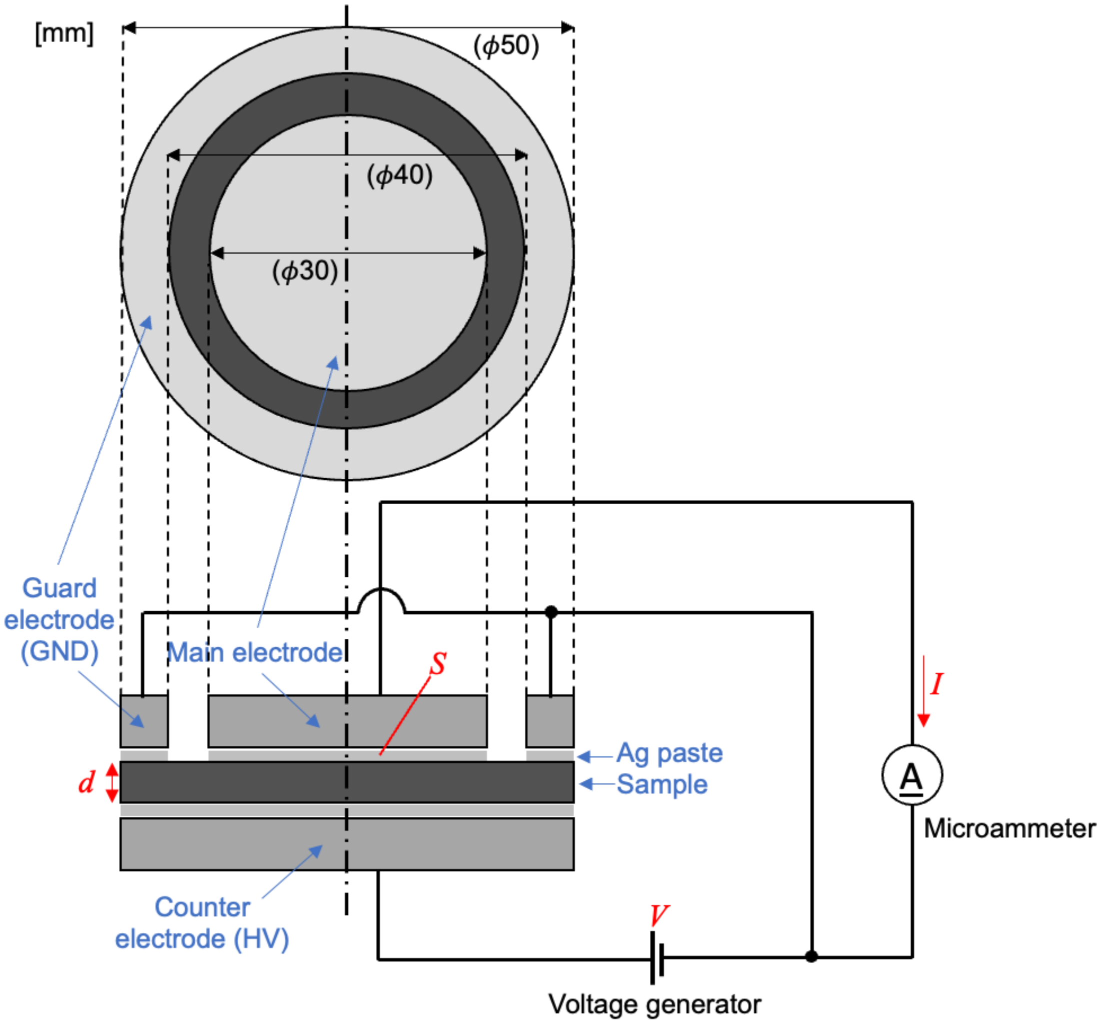

Fig. 2.6 Conductivity measurement circuit

of coefficients σ_0, W, and a on SiC filler contents, as listed in Table 2.3, and shown in Fig. 2.8. As the final result of multivariate analysis process, the curves in Fig. 2.7 indicate the conductivity (σ) characteristics of SiC-filled epoxy composite as a function of T, E, and SiC filler contents.

Table 2.3 σ_0, W, and a coefficients' values based on σ measurements' data

SiC filler contents [vol%]	σ_0 [S/m]	W [eV]	a [mm/kV]
0	1.67×10^{-6}	0.629	0.01
5	2.24×10^{-10}	0.337	0.55
10	1.75×10^{-11}	0.17	1.42

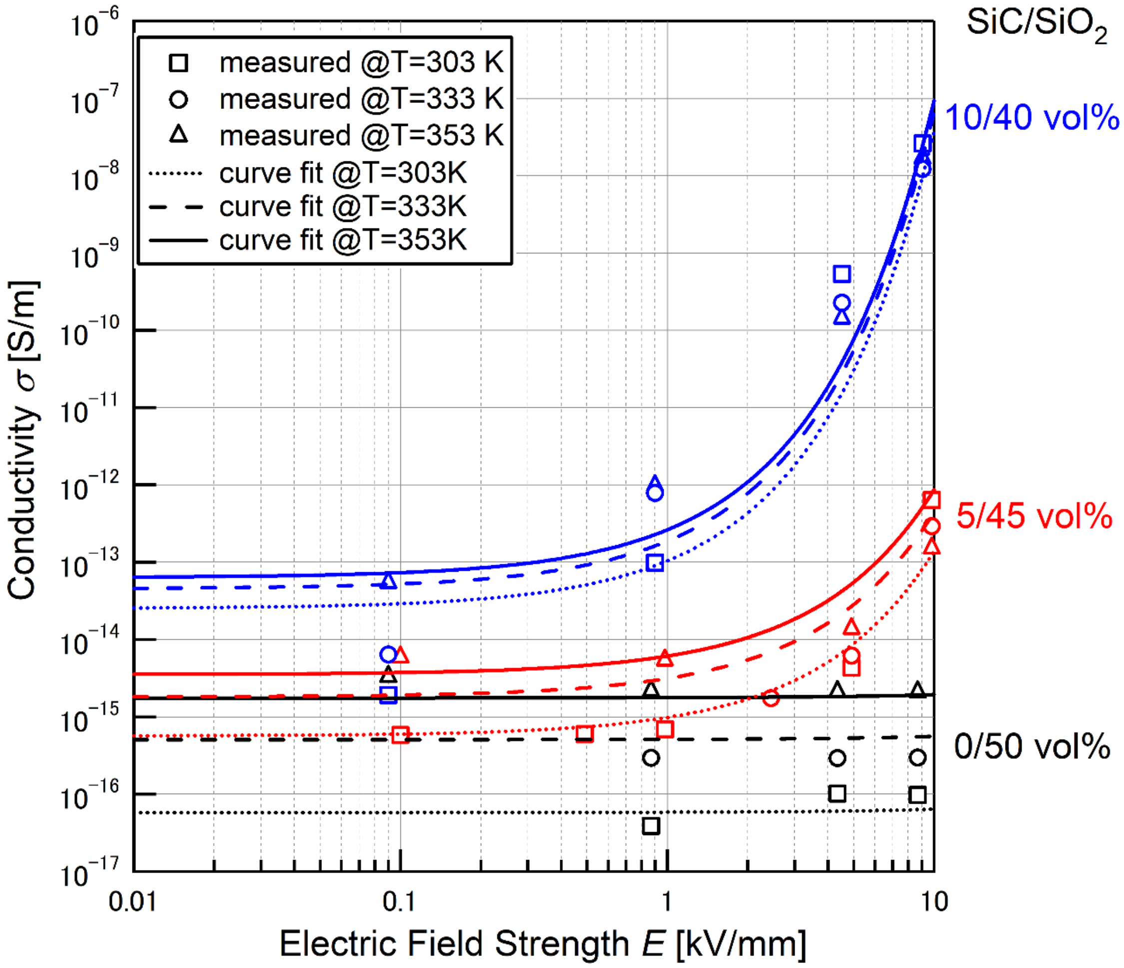

Fig. 2.7 Conductivity (σ) characteristics of SiC-filled epoxy composite.

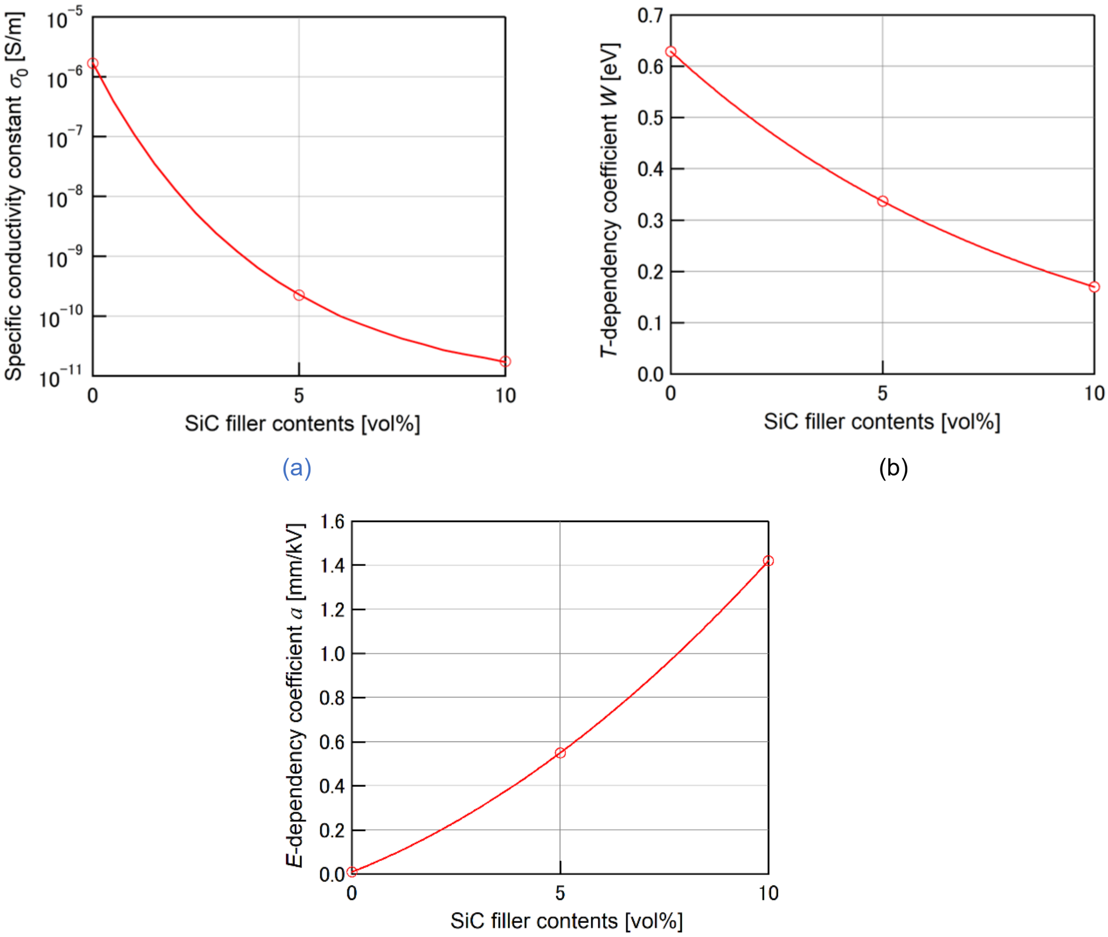

(a)

(b)

(c)

Multivariate analysis results

σ_0, *W*, and *a* as a function of SiC vol%

$$\sigma_0(vol\%) = 5.8 \cdot 10^{-12} \exp(12.57 \exp(-24.61 \times vol\%))$$

$$W(vol\%) = -0.05 + 0.68 \exp(-11.18 \times vol\%)$$

$$a(vol\%) = 0.01 + 7.5 \cdot vol\% + 66 \cdot vol\%^2$$

Fig. 2.8 (a) σ_0, (b) *W*, and (c) a as functions of SiC filler contents

Based on Fig. 2.7, adding SiC filler particles by 5 to 10 vol% can increase the basic σ level by about 10 to 100 times of non-SiC-filled epoxy composite. Furthermore, SiC-filled epoxy composite has higher electric field dependency which will further increase the σ at high electric field stress. On the contrary, the temperature dependency of SiC-filled epoxy composite decreases with SiC filler contents as well as with electric field. It is expected that SiC filler addition can bring an effective electric field relaxation despite temperature changes.

2.5 Permittivity Measurement of SiC-filled Epoxy Composite

2.5.1 Permittivity Measurement Method

The relative permittivity (ε_r) of each sample is obtained through the capacitance measurements by LCR meter at various frequency, where ε_r is calculated by equation (2.3):

$$\varepsilon_r = \frac{C}{\varepsilon_0} \cdot \frac{d}{A} \tag{2.3}$$

where *C* is the measured capacitance in F, ε_0 is the permittivity of the vacuum, and *d* is the sample's thickness in m, and *A* is the cross-sectional area of the sample piece in m^2. Fig. 2.9 shows the setup for capacitance measurement.

2.5.2 Permittivity Measurement and Curve Fitting Results

The ε_r measurement results of epoxy composites with different SiC filler contents at various frequency is shown in Fig. 2.10 (a), and as the representative value, Fig. 2.10 (b) shows ε_r at the frequency of 1 kHz, as well as the curve fitting result indicated by the curve.

The measured ε_r of each 0, 5, and 10 vol% SiC-filled epoxy composite are 3.9, 5.3, and 7.0, respectively. The ε_r measurement results show relatively small difference in ε_r between 0 vol% and 10 vol% SiC-filled epoxy composites ($\Delta\varepsilon_r$~3), which is expected to be insufficient for effective electric field relaxation purpose under LI voltage. If ε/σ-FGM spacer is made of only one type of composite with a certain range of graded functional fillers, e.g. 0 to 10 vol% SiC-filled epoxy composite, then the ε and σ distributions are interdependent according to the SiC-filler distribution. On the one hand, the resulted ε

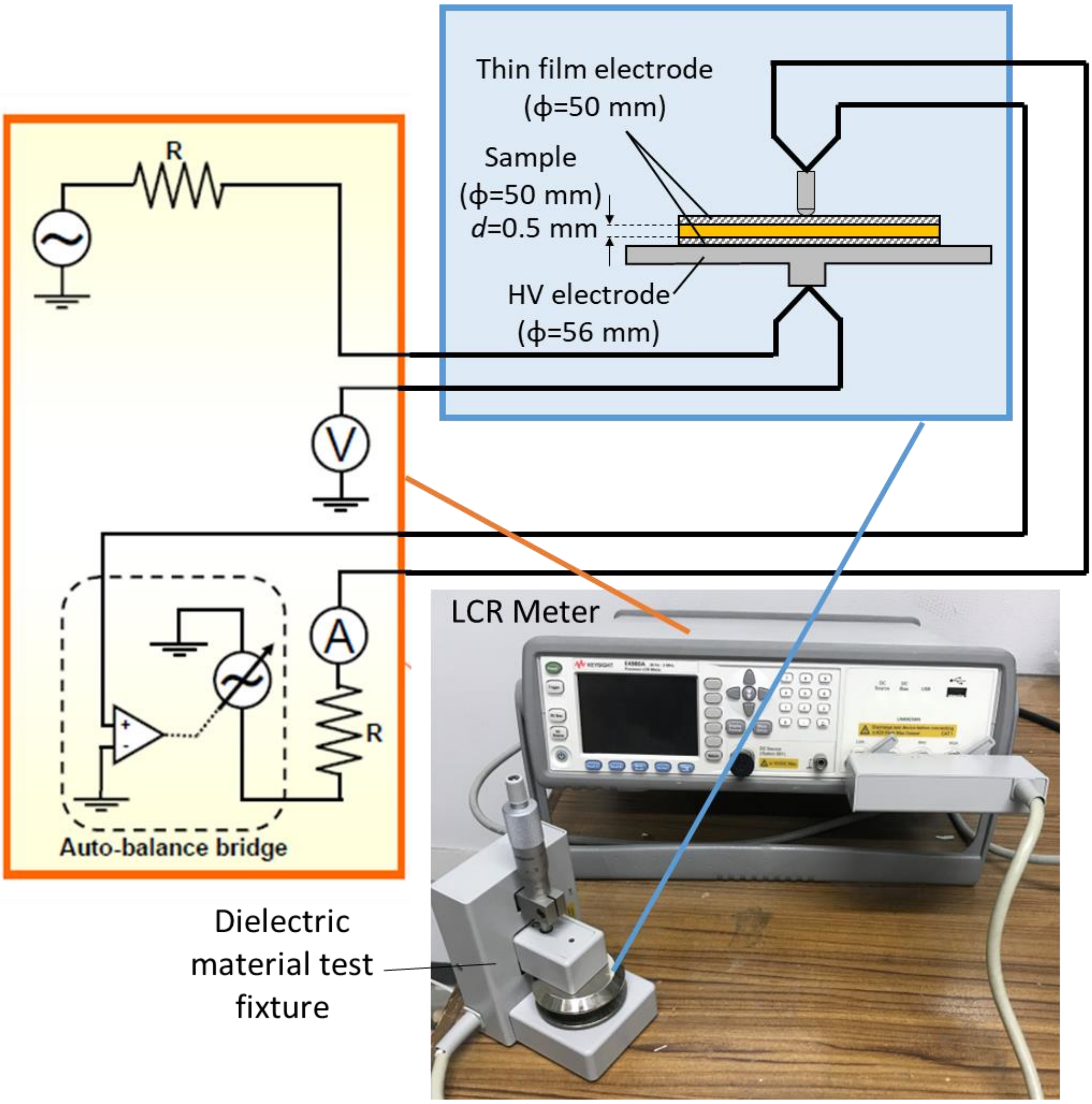

Fig. 2.9 Setup for capacitance measurement.

grading is not effective for capacitive field relaxation. On the other hand, if the range of SiC filler contents are widened in order to obtain sufficient ε grading for E relaxation, e.g. 0 to 30 vol% SiC, the use of too high σ level may risk thermal runaway due to heat generation within the spacer [16].

Thus, it is necessary to add another type of high ε_r composite, which will be described in the next subsection, so that we can create independently controlled ε and σ grading.

2.6 Permittivity Characteristics of $SrTiO_3$-filled Epoxy Composite

For high ε composite, one of the options is the $SrTiO_3$-filled epoxy composite, that are already used for AC ε-FGM in the past works and well proven for electric field relaxation under AC and LI voltages [17]. Fig. 2.11 shows the ε_r characteristics of $SrTiO_3$-filled epoxy composite, while the specification of $SrTiO_3$ filler is included in Table 2.2. Table 2.4 shows the filler contents of the four types of $SrTiO_3/SiO_2$-filled epoxy composite bulk samples and their average ε_r measurement results at the frequency of 1 kHz. The samples were prepared by mixing two composites, which one of them contains 39.6 vol% $SrTiO_3$ and another one contains 41.7 vol% SiO_2, and varying the ratio of both composites. The graph shows that ε_r of $SrTiO_3/SiO_2$-filled epoxy composite is determined by the $SrTiO_3$ filler loading.

Table 2.4 Filler contents and average ε_r of $SrTiO_3/SiO_2$-filled epoxy composites

$SrTiO_3$ filler contents [vol%]	SiO_2 filler contents [vol%]	ε_r
0.0	41.7	3.9
9.9	31.3	6.2
19.8	20.9	9.2
26.9	13.4	12.7

2.7 Conductivity Characteristics of $SrTiO_3$-filled Epoxy Composite

As mentioned in Section 2.5, where $SrTiO_3$-filled epoxy composite is used to provide sufficient ε grading at the same time SiC-filled epoxy composite is used for σ grading, it is important to make sure that the σ of SiC-filled epoxy composite and ε of $SrTiO_3$-filled epoxy composite remain dominant, i.e not to be overlapped by the other composite`s associated properties. The ε of SiC-filled epoxy composite in the range of 0 to 10 vol% SiC (which will be used in the modelling of ε/σ-FGM application) is already confirmed as lower than that of 26.9 vol% $SrTiO_3$-filled epoxy composite, i.e the high ε composite which is used to fabricate AC ε-FGM spacer (see Sections 2.5.2 and 2.6). Therefore, it is also necessary to confirm that σ of $SrTiO_3$-filled epoxy composite does not affect SiC-filled epoxy composite, assuming that $SrTiO_3$ fillers are less conductive of a material than SiC fillers.

Fig. 2.12 shows the σ measurement results of high ε composite, i.e. 26.9 vol% $SrTiO_3$-filled epoxy composite, which is displayed on σ characteristics of SiC-filled epoxy composite in Fig. 2.7. From the figure, the σ of $SrTiO_3$-filled epoxy composite at T=303 K has similar base conductivity as 5 vol% SiC-filled epoxy composite at T=333 K, i.e. about 10^{-15} S/m and a little higher than that of 5 vol% SiC-filled epoxy composite at the same low temperature of 303 K. However, as the applied electric field strength increases higher than 1 kV/mm, the σ of 5 vol% SiC-filled epoxy composite both at T=303 and 333 K starts to increase exponentially (the nonlinearity is activated), while the σ of $SrTiO_3$-filled epoxy composite has comparably much lower increase, i.e much lower E-dependency. Therefore, we can say that the σ characteristics of $SrTiO_3$-filled epoxy composite are less effective for σ grading, compared to those of SiC-filled epoxy composite.

2.8 Summary

In this chapter, ε/σ-FGM concept for DC application that utilizes both permittivity and conductivity grading in order to gain electric field relaxation effects under various DC operating conditions are explained. The basic steps to obtain permittivity and conductivity characteristics of the nonlinear field grading material, i.e. SiC-filled epoxy composite from sample fabrication, measurement method, to measurement results are also discussed.

The following results are obtained:

1) It is necessary to incorporate both permittivity and conductivity grading to control capacitive (AC) and resistive (DC) fields that occur under various DC operating conditions,
2) Conductivity profiles of SiC-filled epoxy composite as functions of temperature, electric field strength, and SiC filler contents were measured and their database was constructed by multivariate analysis.

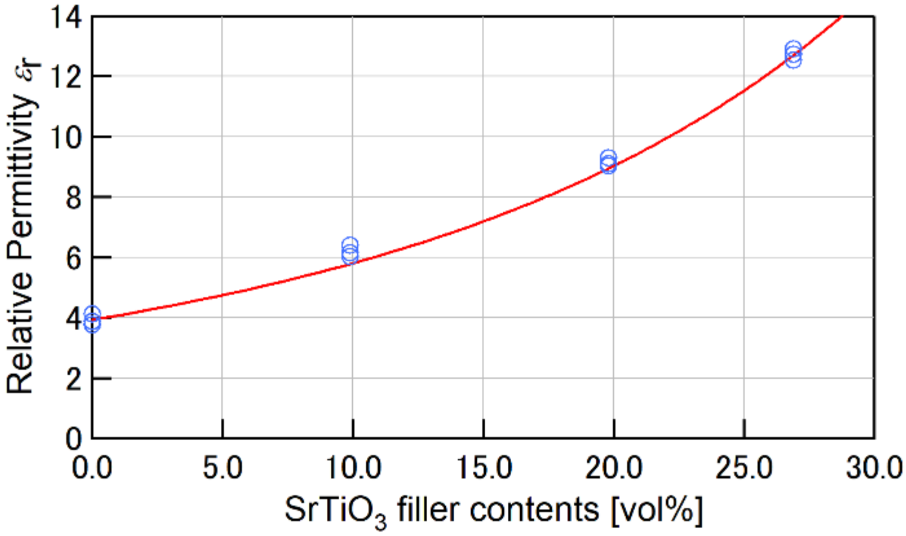

Fig. 2.11 ε_r characteristics of $SrTiO_3$-filled epoxy composite [17].

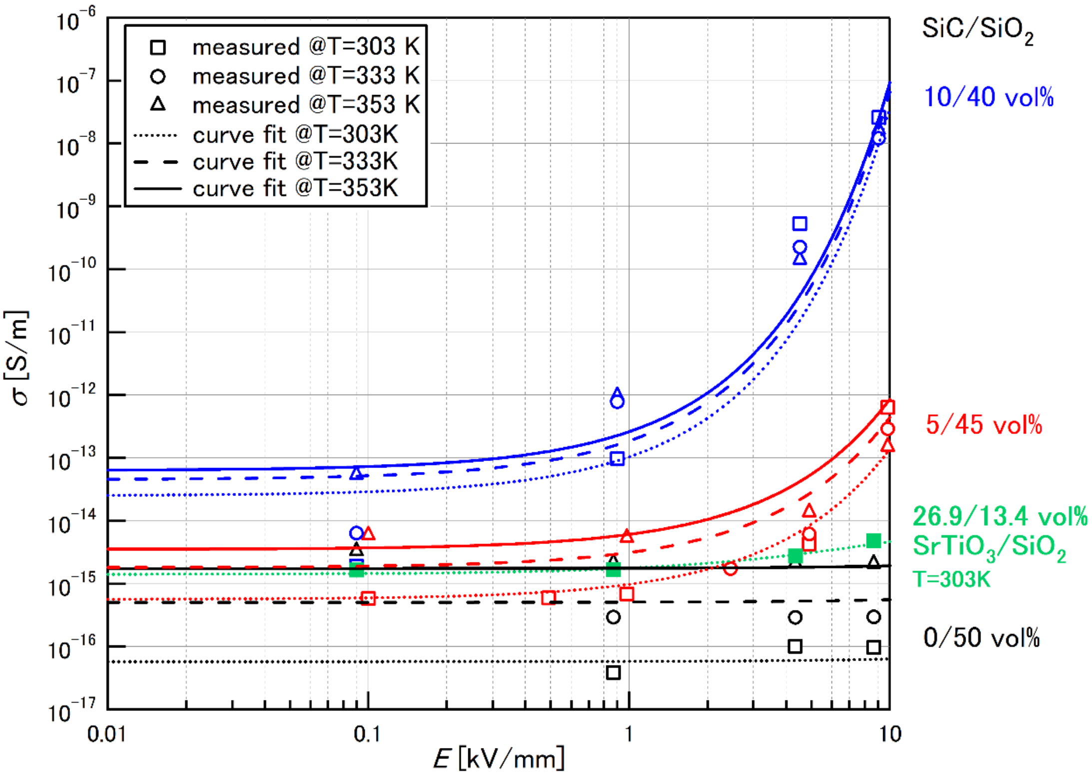

Fig. 2.12. σ characteristics of $SrTiO_3$-filled epoxy composite.

3) Permittivity profiles of SiC-filled epoxy composite as a function of SiC filler content was also measured and the results show relatively small gap of ε of 0 to 10 vol% SiC-filled epoxy composite, which is expected as not sufficient for capacitive field grading.
4) Permittivity characteristics of $SrTiO_3$-filled epoxy composite will be adopted and incorporated to the implementation of ε/σ-FGM spacer for DC application.

References

[1] K. Okamoto, N. Hayakawa, M. Hikita, H. Okubo, K. Kato, N. Osawa, K. Watanabe and K. Adachi, "Distinctive Downsizing of Cone-Type Insulating Spacer for 245 kV Class GIS by Functional Insulating Materials," *CIGRE Science and Engineering,* pp. 120-133, Feb 2022.

[2] N. Hayakawa, Y. Miyaji, H. Kojima and K. Kato, "Electric field reduction by functionally graded materials (FGM) with permittivity and conductivity distribution," in *2016 IEEE Conference on Electrical Insulation and Dielectric Phenomena (CEIDP)*, Toronto, Canada, 2016, pp.627-630.

[3] 落合 他, "可変配合注型法による誘電率傾斜機能材料の作製および放電開始電圧向上効果," in *電気学会電力・エネルギー部門大会*, 363, 2018.

[4] K. Adachi, H. Muto, K. Okamoto, Y. Hoshina and N. Fujimoto, "Development of New Types of Insulators for Electric Power Apparatuses Using Nanocomposites and Functionally Graded Materials," in *2020 IEEE 3rd International Conference on Dielectrics (ICD)*, Valencia, Spain, 2020, pp.317-320.

[5] N. Hayakawa, K. Kato, M. Hikita, H. Okubo, K. Watanabe, K. Adachi and K. Okamoto, "Development of Cone-Type FGM Spacer for Actual Size GIS," in *2020 IEEE Conference on Electrical Insulation and Dielectric Phenomena (CEIDP)*, East Rutherford, USA, 2020, pp.255-258.

[6] N. Hayakawa, Y. Miyazaki, H. Kojima, K. Kato, H. Okubo, K. Adachi and K. Okamoto, "Flashover voltage estimation of cone-type GIS spacer with permittivity graded materials (ε-FGM) by Volume-Time theory in consideration with conductor surface roughness in SF6 gas," in *22nd International Symposium on High Voltage Engineering (ISH)*, no.705, *online*, 2021.

[7] N. Hayakawa, R. Oishi, H. Kojima, K. Kato and N. Zebouchi, "Electric field grading by Functionally graded materials (FGM) for HVDC gas insulated power apparatus," in *2018 IEEE Conference on Electrical Insulation and Dielectric Phenomena (CEIDP)*, Cancun, Mexico, 2018, 5-3, pp.309-312.

[8] CIGRE WG D1.56, "Field grading in electrical insulation systems," CIGRE Technical Brochure No. 794, 2020.

[9] X. Yang, X. Zhao, J. Hu and J. He, "Grading electric field in high voltage insulation using composite materials," *IEEE Electrical Insulation Magazine,* vol. 34, no. 1, pp. 15-25, Jan-Feb

2018.

[10] B. X. Du, H. C. Liang and J. Li, "Surface Coating Affecting Charge Distribution and Flashover Voltage of Cone-type Insulator under DC Stress," *IEEE Transactions on Dielectrics and Electrical Insulation,* vol. 26, no. 3, pp. 706-713, 2019.

[11] M. Hering, S. Grossmann, J. Speck and U. Riechert, "Investigation of the temperature influence on the breakdown voltage in gas insulated systems under DC voltage stress," in *Proceedings of the 18th International Symposium on High Voltage Engineering (ISH),* OE7-02, pp. 1354-1359, Seoul, South Korea, 2013.

[12] H. Li, N. Zebouchi and A. Haddad, "Theoretical and practical investigations of spacer models for future HVDC GIL/GIS applications," in *Proceedings of the 21st International Symposium on High Voltage Engineering (ISH),* vol.2, pp. 1538-1549, Budapest, Hungary, 2019.

[13] 日本工業標準調査会, “JIS C 2170：静電気電荷蓄積を防止する固体平面材料の抵抗及び抵抗率試験方法”, 2004.

[14] 日本工業標準調査会, “JIS C 2139-3-1: 固体電気絶縁材料の誘電特性及び抵抗特性－第 3-1 部：直流電圧印加による抵抗特性の測定－体積抵抗及び体積抵抗率”, 2018.

[15] IEC 62631-3-4, “Dielectric and Resistive Properties of Solid Insulating Materials – Part 3-4: Determination of resistive properties (DC methods) – Volume resistance and volume resistivity at elevated temperatures”, 2019.

[16] M. Hering, K. Juhre, M. Secklehner and V. Hinrichsen, "Requirements on solid insulating materials and gas-solid interfaces in compact HVDC gas-insulated systems," in *The 20th International Symposium on High Voltage Engineering (ISH),* OG1-3, Buenos Aires, Argentina, 2017.

[17] Y. Miyazaki, H. Kojima, H. Masui, H. Mitsudome, H. Yanase, K. Okamoto, K. Watanabe, K. Kato and N. Hayakawa, "Breakdown characteristics of cone-type ε-FGM spacer for gas insulated switchgears," *IEEJ Transactions on Fundamentals and Materials,* vol. 141, no. 10, pp. 546-551, 2021.

Chapter 3 Electric Field Simulation of 320 kV HVDC ε/σ-FGM Spacer under Various DC Operating Conditions

3.1 Introduction

As mentioned in Section 2.2, it is important to evaluate the applicability of ε/σ-FGM with graded permittivity and/or conductivity to a GIS/GIL spacer under various DC operating conditions in order to verify the designed FGM spacer can handle both capacitive (AC) and resistive (DC) fields. For the initial stage, this chapter discusses the electric field calculation results of 320 kV HVDC ε/σ-FGM spacer model under DC steady state (DC-SS), DC polarity reversal (DC-PR), DC-on, and superimposed positive and negative LI voltage on DC-SS in comparison to those of the Uniform model without graded ε and σ. The simulation is conducted using COMSOL Multiphysics® software by finite element method. In the simulation, we apply the material properties (ε and σ) directly to each domain that represent different mediums and/or materials, e.g. gas, spacer, conductors. The ε and σ can be a constant value (as in the Uniform spacer) or a variable that changes with space coordinates so that different properties present at different parts of the material structure (as in ε/σ-FGM spacer). Potential value is also applied to the boundary of HV and GND electrodes. COMSOL then internally applies the ε and σ values to mesh in each different material and calculate the potential and electric field at each mesh of the whole simulation model. The final solutions are presented as potential and electric field distributions.

3.2 Calculation Method and Conditions

The electric field analysis is performed using finite element method (FEM) by COMSOL Multiphysics® software. The electric field distribution around the GIS spacer model is calculated by considering the conduction process between the spacer material (epoxy composite) and the surrounding gas (SF_6), which is characterized by their volume conductivities.

In calculating electric field, first the potential value φ of each element can be calculated by the following differential equation.

$$\nabla^2\varphi = \frac{1}{r}\frac{\partial}{\partial r}\left(r\frac{\partial\varphi}{\partial r}\right) + \frac{1}{r^2}\frac{\partial^2\varphi}{\partial\theta^2} + \frac{\partial^2\varphi}{\partial z} \tag{3.1}$$

According to Poisson's equation

$$\nabla^2\varphi = \frac{1}{r}\frac{\partial}{\partial r}\left(r\frac{\partial\varphi}{\partial r}\right) + \frac{1}{r^2}\frac{\partial^2\varphi}{\partial\theta^2} + \frac{\partial^2\varphi}{\partial z} = -\frac{\rho_V}{\varepsilon} \tag{3.2}$$

with ρ_V is space charge density and ε is permittivity. Then, the relationship between E and φ is shown as in equation (3.3)

$$E = -grad\varphi = -\nabla\varphi \tag{3.3}$$

On the other hand, the temperature distribution in this electric field simulation is obtained by heat equation analysis which is derived from energy balance equation in a volume of a material (domain *D*) as shown in equation (3.4).

$$\int_D \rho\frac{dE_i}{dt}dV + \int_D (\boldsymbol{q}\cdot\boldsymbol{n})\,dS = \int_D Q\,dV. \tag{3.4}$$

with

$$E_i = C_p \cdot T \tag{3.5}$$

$$\boldsymbol{q} = -(\kappa\nabla T) \tag{3.6}$$

The first term of equation (3.4) shows the total accumulated energy rate in *D* with ρ is density in kg/m^3, E_i is the total internal energy in *D* in J/kg, *t* is time in s, *V* is the volume of *D* in m^3, C_p is the specific heat capacity at constant pressure in J/(kg.K), and *T* is absolute temperature in K. The second term of equation (3.4) refers to net energy transfer to and out of *D*, which in this case is defined by conduction heat flux $\boldsymbol{q}$ in W/m^2 and $\boldsymbol{n}$ is the normal vector on the boundary of *D*. κ is the thermal conductivity in W/(m.K). Then, the term on the right side of equation (3.4) refer to heat source, with *Q* is heat generated by a heat source in W/m^3.

By applying divergence and substituting equations (3.5) and (3.6) to equation (3.4), the following equation (3.7) is obtained,

$$\rho C_p\frac{\partial T}{\partial t} + \nabla\cdot -(\kappa\nabla T) = Q \tag{3.7}$$

In the current simulation, the heat generation *Q* within the spacer is assumed to be so small, hence neglected. Therefore, the heat equation becomes,

$$\rho C_p\frac{\partial T}{\partial t} + \nabla\cdot -(\kappa\nabla T) = 0 \tag{3.8}$$

where for a steady state simulation, the first term with time derivatives disappears.

For further details, Table 3.1 shows the equations used in this simulation as well as the boundary conditions.

Table 3.1 Equations used and boundary conditions in electric field simulation.

Electric field distribution	**Steady state** $\nabla\cdot\boldsymbol{J}=\boldsymbol{0}$ $\boldsymbol{J}=\sigma\boldsymbol{E}$ $\boldsymbol{E}=-\mathrm{grad}\varphi=-\nabla\varphi$ $\nabla\cdot(\sigma\nabla\varphi)=0$ Boundary conditions on the interfaces. $\sigma_1E_1-\sigma_2E_2=0$ $\varepsilon_1E_1-\varepsilon_2E_2=\rho_s$ **Time-dependent** (DC-on, DC±LI) $\nabla\cdot\boldsymbol{J}=\boldsymbol{0}$ $\boldsymbol{J}=\sigma\boldsymbol{E}+\frac{\partial\boldsymbol{D}}{\partial t}$ $\boldsymbol{D}=\varepsilon_0\varepsilon_r\boldsymbol{E}$ $\nabla\cdot\left(\varepsilon-j\frac{\sigma}{2\pi f}\right)\nabla\varphi=0$ **DC-on** Boundary conditions on the interfaces. $\varepsilon_1E_1-\varepsilon_2E_2=0$ **DC-PR** $\lvert\boldsymbol{E_{PR}}\rvert=\lvert 2\boldsymbol{E_{AC}}-\boldsymbol{E_{DC}}\rvert$	$\boldsymbol{J}$: current density [A/m^2] σ : conductivity [S/m] E : electric field [V/m] φ : potential [V] ε : permittivity [F/m] ρ_s : surface charge density [C/m^2] $\boldsymbol{D}$: Displacement field [C/m^2] ε_0 : permittivity in vacuum [F/m] ε_r : relative permittivity f : frequency [Hz] $\boldsymbol{E_{PR}}$: E at DC-PR [V/m] $\boldsymbol{E_{AC}}$: capacitive field [V/m] $\boldsymbol{E_{DC}}$: resistive field [V/m]
Voltage application	**HV conductor surface :** $\varphi=V_0$ DC-SS : V_0 = 320 kV DC-on : V_0 = 0 to 320 kV (switching time t_s=0.01 s) DC±LI : V_0 = 320 kV ± 1175 kV$_{\mathrm{peak}}$ **GND inner tank :** $\varphi=0$ [V]	
Temperature distribution	**Steady-state :** $\nabla\cdot\boldsymbol{q}=0$ **Time-dependent :** $\rho C_p\frac{\partial T}{\partial t}+\nabla\cdot\boldsymbol{q}=0$ $\boldsymbol{q}=-\kappa\nabla T$	$\boldsymbol{q}$: heat flux κ : thermal conductivity [W/(m.K)] ρ : density [kg/m^3] C_p : heat capacity [J/(kg.K)] T : temperature [K]
Temperature on boundary	**HV conductor surface :** T_{HV} = 300 – 370 K (T_{step}=10 K) **GND inner tank :** T_{GND}= 300 K	

In Table 3.1, under DC-PR voltage application, according to [9], the electric field (E_{PR}) in SF_6 gas at DC-PR can be calculated by Equation (3.9):

$$E_{PR} = |2E_{AC} - E_{DC}| \tag{3.9}$$

where E_{AC} and E_{DC} are the capacitive and resistive field, respectively. This calculation can be illustrated by the voltage waveform in Fig. 3.1.

3.3 ε and σ Distributions of 320 kV HVDC ε/σ-FGM Model and Simulation Conditions

3.3.1 σ model for ε/σ-FGM

The idea of electric field grading in gas in this gas/solid composite system is by controlling the σ of the spacer bulk, i.e. by setting higher σ at the spacer parts around the area with locally enhanced electric field, such as interfaces and triple junctions, so that electric field stress around that area is suppressed and the potential burden is distributed to areas around the spacer parts with lower σ. Thus, smooth grading of material properties (ε and/or σ) of the spacer is necessary to result in more evenly distributed electric field in gas around the spacer.

Common spacer's material for GIS/GIL is made of epoxy resin, with conductivity that can be expressed by equation (3.10) [1,2].

$$\sigma(T, E) = \sigma_0 \exp\left(-\frac{W}{kT}\right) \exp(aE) \tag{3.10}$$

where σ_0 is the specific conductivity constant in S/m, k is Boltzmann constant in eV/K, $W = 0.95$ eV and $a = 0.08$ mm/kV [1-3] are the thermal activation energy and electric field dependency coefficient of epoxy insulating material. Fig. 3.2 shows σ characteristics of epoxy insulating material with relatively larger T-dependency compared to the smaller E-dependency [4].

3.3.2 320 kV HVDC GIS spacer simulation model

Fig. 3.3 shows the simulation model of a 320 kV DC GIS cone-type spacer [5, 6] with graded permittivity and/or conductivity distributions (ε/σ-FGM) in comparison with the Uniform spacer with constant ε and σ. There are two types of σ grading, i.e U-shaped and grading-to-higher conductivity (GHC), and one type of ε grading, i.e U-shaped, each

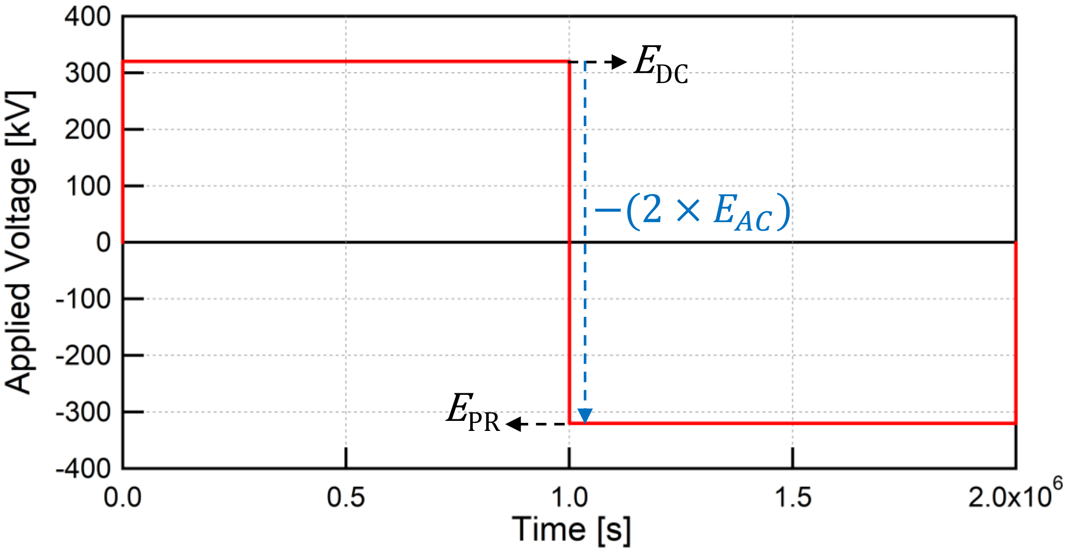

Fig. 3.1 Voltage application at DC-PR and illustration of E_{PR} calculation.

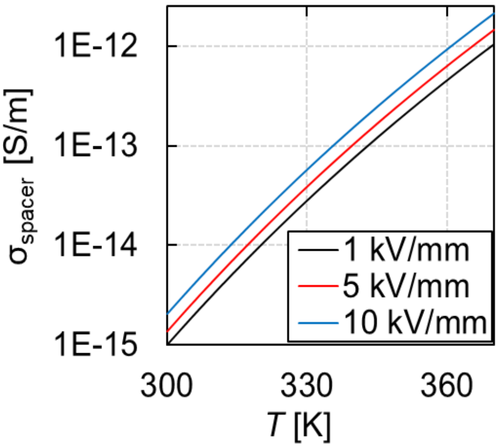

Fig. 3.2 E- and T-dependency characteristics of epoxy resin's conductivity [4]

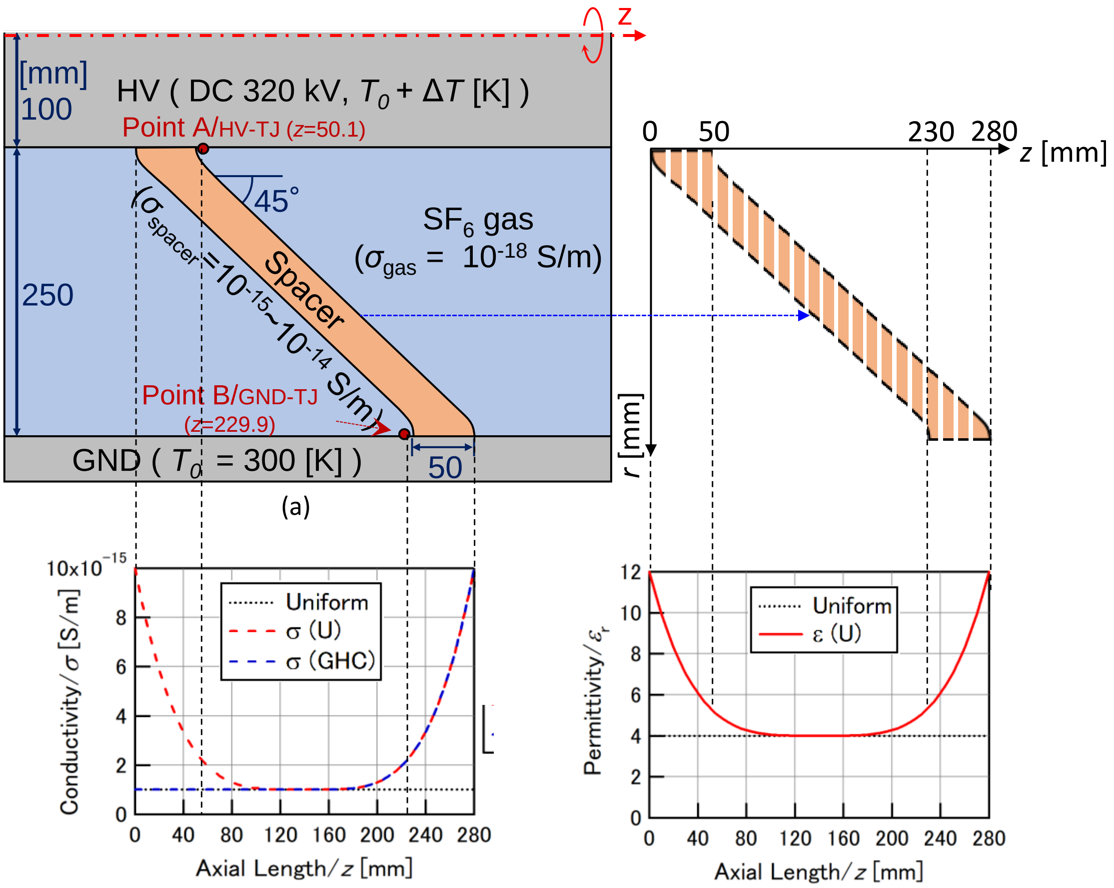

(a)

(b)

(c)

Fig. 3.3 (a) 320 kV DC FGM cone-type spacer simulation model with (b) conductivity distribution types at T=300 K and E=1 kV/mm, and (c) permittivity distribution types combination of which are simulated in this work. These ε and σ gradings are supposed to be formed within the spacer bulk longitudinally along *z* axis by controlling the density of the filler with high ε and σ through flexible mixture casting (FMC) method [7]. This method allows the composite mixture to be accumulated in a spacer mold from $z = 0$ up to $z = 280$ mm, so that the ε and σ values change gradually in z direction.

The conductivity distribution of σ(U) with U-type σ grading and σ(GHC) with grading-to-higher-conductivity has the lowest σ value of 10^{-15} S/m [7], i.e the minimum σ level of unfilled epoxy resin, which is at the same level of the Uniform spacer, and the highest σ value of 10^{-14} S/m (10 times of σ(Uniform)) [3], assuming the temperature (T) is 300 K and the electric field strength (E) is 1 kV/mm. The difference between σ(U) and σ(GHC) is the spacer parts that have higher σ value, i.e. at both interfaces with the high voltage (HV) and the ground (GND) sides for σ(U)-FGM spacer. σ(U) grading is expected to be able to reduce high electric field stress in the vicinity of the concave surface of the spacer near the HV side (the triple junction of HV side, HV-TJ) and in the vicinity of the convex surface of the spacer near the GND side (GND-TJ). Hence, electric field in SF_6 gas is more uniformly distributed around the middle part of the spacer with lower σ.

On the other hand, σ(GHC) with higher σ value contained only at the spacer/GND interface, is considered for electric field relaxation at DC polarity reversal (DC-PR). Following equation (3.9), the spacer with σ(U) has higher σ near HV-TJ which can reduce E_{DC} component at HV-TJ, hence, the E_{PR} increases. For this purpose, σ(GHC) is more likely to lead to better results, as it has low σ around HV-TJ up to the middle part of the spacer, resulting in enhanced E_{DC} component around that area. Thus, E_{PR} is reduced.

Additionally, due to E_{AC} occurrence under DC-PR or other conditions with superimposed voltages, ε grading in U-type where the spacer parts at the interface with HV and GND sides have high ε ($\varepsilon_r = 12$) and the middle part of the spacer has low ε ($\varepsilon_r = 4$) is expected to reduce high electric field in SF_6 gas around HV electrode/ spacer and GND electrode/spacer interfaces [10].

3.3.3 Electric field simulation conditions

Some combinations of ε and σ distributions as mentioned in the previous section are applied to the cone-type spacer model in Fig. 3.2 under four voltage application conditions given in Table 3.2. Based on the electric field simulation results under DC steady state and polarity reversal, the most effective ε and σ distributions of FGM spacer model to the electric field grading will be selected and compared with the Uniform spacer under DC-on and superimposed LI on DC steady state.

As shown in Equation (3.10), DC conductivity depends on temperature. Thus, the temperature effect is examined by changing the temperature of the high voltage conductor as $T_0+\Delta T$ from the lowest temperature of 300 K to the possible maximum temperature in GIS during operation, which is 370 K (ΔT = 0–70 K) [2], while keeping the temperature of the ground tank at T_0 = 300 K.

Table 3.2 Electric field simulation conditions.

Applied Voltage	Uniform ε/σ distribution	FGM	
		σ distribution	ε distribution
DC steady state	uniform ($\varepsilon_r = 4$, $\sigma = 10^{-15}$ S/m)	uniform	U-type
		U-type	constant
		U-type	U-type
		GHC	U-type
DC polarity reversal		uniform	U-type
		U-type	constant
		U-type	U-type
		GHC	U-type
DC-on		GHC	U-type
Superimposed ±LI on DC steady state		GHC	U-type

3.4 Electric Field Simulation Results

3.4.1 DC Steady State

In DC steady state simulation, 320 kV DC voltage is applied to the HV conductor. Then, the electric field distribution and the maximum electric field strength ($E_{\max}$) in gas around the uniform and each type of FGM spacers is calculated with increasing ΔT from 0–70 K. Fig. 3.4 shows the electric field distribution around (a) Uniform, (b) σ(U)-FGM, and (c) ε(U)/σ(GHC)-FGM spacers when ΔT=0, 30, and 60 K. In order to explain further about the differences in Fig, 3.4, temperature distribution and conductivity distribution at each condition are shown in Figs. 3.5 and 3.6, respectively. The black circle on each figure in Fig 3.4 show E_{max} location in SF_6 gas, whereas in Fig. 3.6 it shows σ_{max} in the spacer.

Fig. 3.4 (a) shows that when ΔT=0 K, E_{max} around the Uniform spacer is located at HV-TJ, and as ΔT increases, E_{max} location is shifted toward GND-TJ with larger magnitude. This is because when ΔT>0 K, σ of Uniform spacer is enhanced with temperature increase as shown in Figs. 3.5 (b), 3.5 (c), and 3.6 (a), where σ of the spacer at HV-TJ is about 10^{-14} and 10^{-12} when ΔT=30 and 60 K, respectively. Hence, the equipotential lines are pushed toward area with lower σ. When ΔT=30 K, the σ of half upper part of the spacer is enhanced while the σ of half lower part of the spacer is still low (Fig. 3.6 (a) middle), hence E_{max} location is shifted toward spacer surface near GND-TJ (Fig. 3.4 (a) middle). When ΔT=70 K, almost ¾ parts of the spacer have σ enhanced (Fig. 3.6 (a) lower), causing E in those parts reduced and E magnitude at GND-TJ is further increased (Fig. 3.4 (a) lower). Therefore, E_{max} around the Uniform spacer is the largest when ΔT=70 K at GND-TJ.

However, for σ(U)-FGM spacer, the σ of spacer parts near HV-TJ and GND-TJ of about 10^{-14} S/m is already higher than that of the Uniform spacer (Fig. 3.6 (b) upper). Thus, when ΔT=0 K, E_{max} location is already shifted away from HV-TJ along the conductor surface, hence E_{max} magnitude is reduced, as shown in the upper figure of Fig. 3.4 (b). As ΔT increases, the σ of σ(U)-FGM spacer parts near HV-TJ is further increased 10 to 1000 times (Fig. 3.6 (b) middle and lower), causing E_{max} location shifted along the spacer's concave surface where σ is lower (Fig. 3.4 (b) middle and lower). Despite more volume of the spacer's σ is enhanced when ΔT=70 K, the σ of spacer's part near spacer/GND enclosure interface is also high (~10^{-14} S/m, higher than that of the Uniform spacer). Thus, E_{max} location remains at the spacer's concave surface and does not reach GND-TJ. Additionally, E_{max} magnitude is also lower than that of the Uniform spacer, as shown in Fig. 3.4 (b).

On the other hand, E distribution around ε(U)/σ(GHC)-FGM spacer has higher E stress at HV-TJ compared to σ(U)-FGM and the Uniform spacers when ΔT=0 K, as shown in the upper figure of Fig. 3.4 (c). It is because ε(U)/σ(GHC)-FGM spacer has higher σ only at spacer/GND enclosure interface (Fig. 3.6 (c) upper), so electric field stress around that area is reduced due to higher σ of 10^{-14} S/m. Therefore, potential distribution is shared to

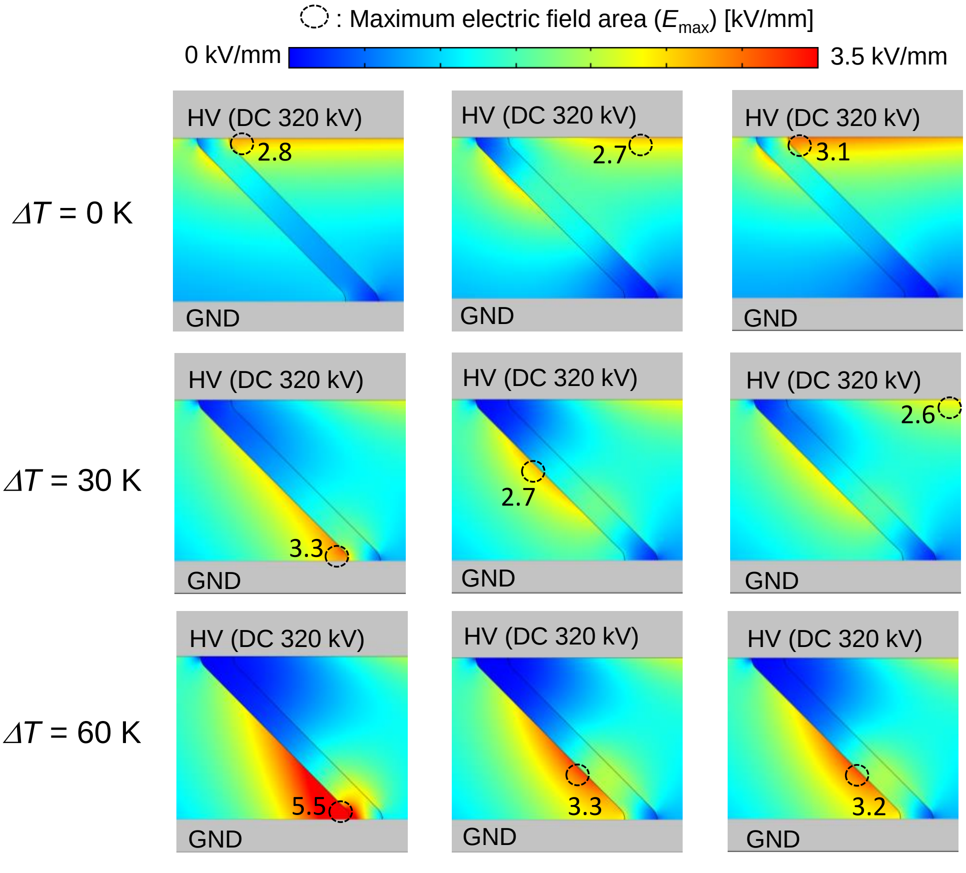

(a) Uniform (b) σ(U)-FGM (c) ε(U)/σ(GHC)-FGM

Fig. 3.4 Electric field distribution around spacers under DC steady state.

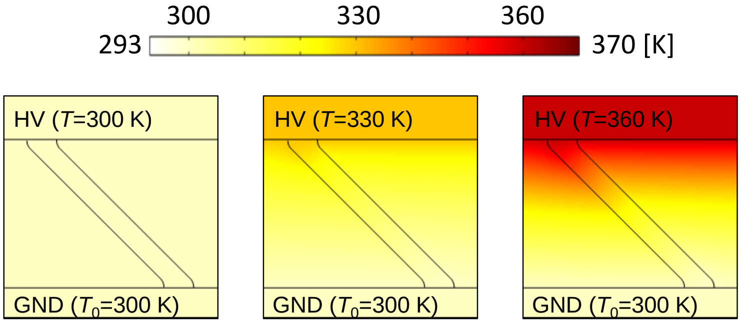

(a) ΔT=0 K (b) ΔT=30 K (c) ΔT=60 K

Fig. 3.5 Temperature distribution in electric field simulation model when ΔT is (a) 0 K, (b) 30 K, and (c) 60 K

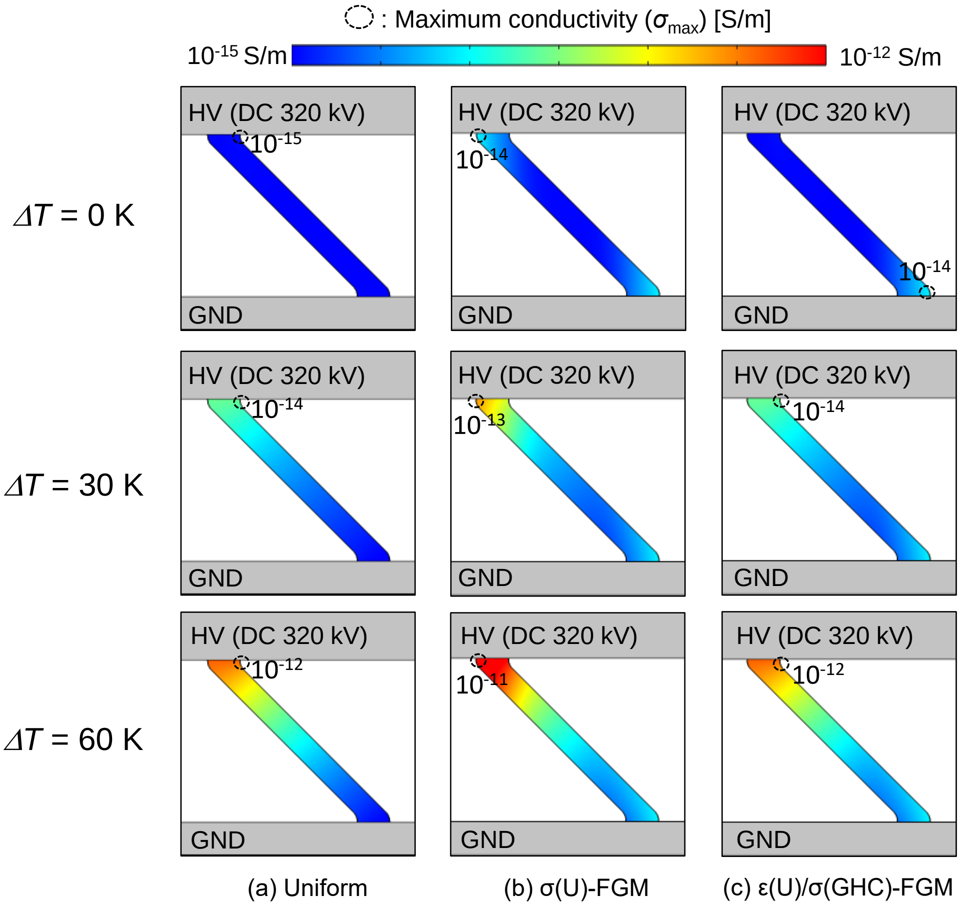

Fig. 3.6 Conductivity distribution within spacers under DC steady state.

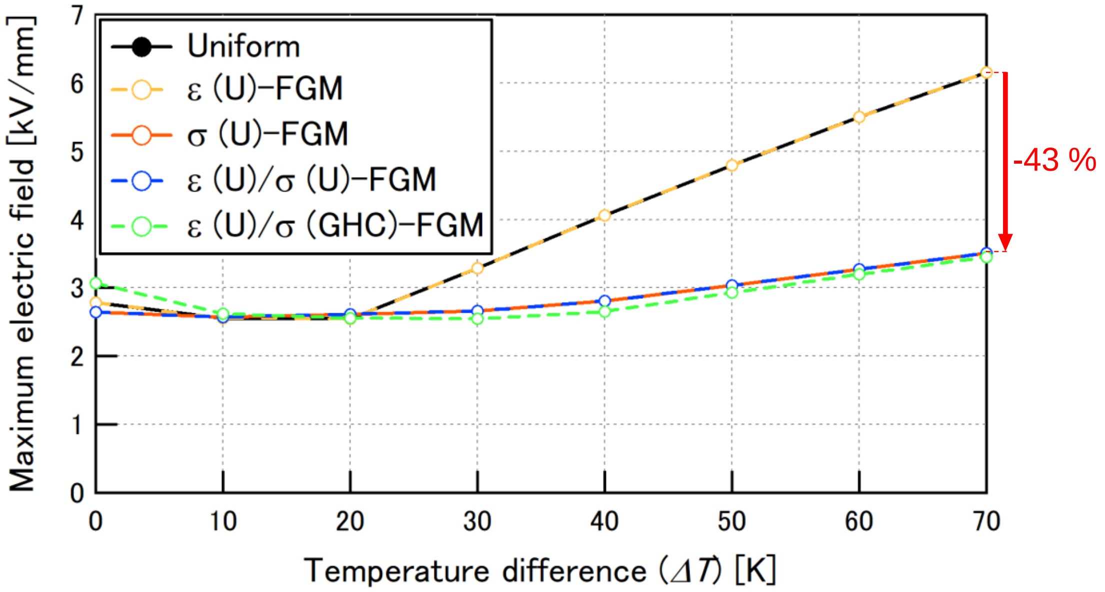

Fig. 3.7 Maximum electric field strength in gas around the spacer under DC steady state.

the spacer parts near HV-TJ which have lower σ ($\sim 10^{-15}$ S/m). As ΔT increases, Fig.3.6 (c) show that the σ of spacer at spacer/HV conductor interface is enhanced in similar magnitude with that of the Uniform spacer, but the σ of spacer part at spacer/GND interface is similar with those of the σ(U)-FGM spacer, i.e. σ of ε(U)/σ(GHC)-FGM is enhanced in a slower rate compared to σ(U)-FGM spacer. Thus, when ΔT=70 K, potential burden is pushed toward spacer's concave surface near GND side, with lower $E_{\max}$ magnitude than that of σ(U)-FGM spacer, as shown in Fig. 3.4 (c).

In order to compare electric field reduction effect, Fig. 3.7 shows the trend of $E_{\max}$ in SF_6 gas against ΔT for different types of spacers. The graph reveals that $E_{\max}$ around the Uniform spacer at each ΔT is the same as that around ε(U)-FGM spacer. Similarly, $E_{\max}$ around σ(U)-FGM spacer is the same as that around ε(U)/σ(U)-FGM spacer. This result proves that under DC steady state condition, whether it is graded or not, ε of the spacer does not contribute to electric field distribution in the insulation system, because ε is not decisive under DC steady state. Only the FGM spacers with graded σ can suppress $E_{\max}$ despite the increase in ΔT. $E_{\max}$ reduction of σ(U)-FGM and ε(U)/σ(GHC)-FGM spacers reaches 43% at ΔT = 70 K.

3.4.2 DC Polarity Reversal

At DC-PR, there is a sudden change in the voltage magnitude from positive 320 kV to negative 320 kV over a short switching time of 0.02 s, as described in Fig 3.1. Therefore, both ε and σ are decisive on electric field distribution. Since E_{PR} in this simulation is calculated according to Equation (3.9), E_{+DC}, E_{AC}, and E_{PR} distribution around the Uniform and various FGM spacers at ΔT=20 K are presented in Figs. 3.8, 3.9, and 3.10, respectively.

Figs. 3.8(a) and 3.8(b) show that electric field distribution around the Uniform spacer is similar to that of ε(U)-FGM spacer, which proves that ε grading without σ grading in an FGM spacer does not affect electric field distribution under DC steady state condition, i.e. the resistive field. On the other hand, Figs. 3.8(c), 3.8(d), and 3.8(e) show that electric field distribution around FGM spacers with graded σ, regardless of the ε grading, is different from that around the Uniform spacer. The high electric field stress within the HV-TJ and GND-TJ are clearly reduced due to the higher σ of the spacer parts near those

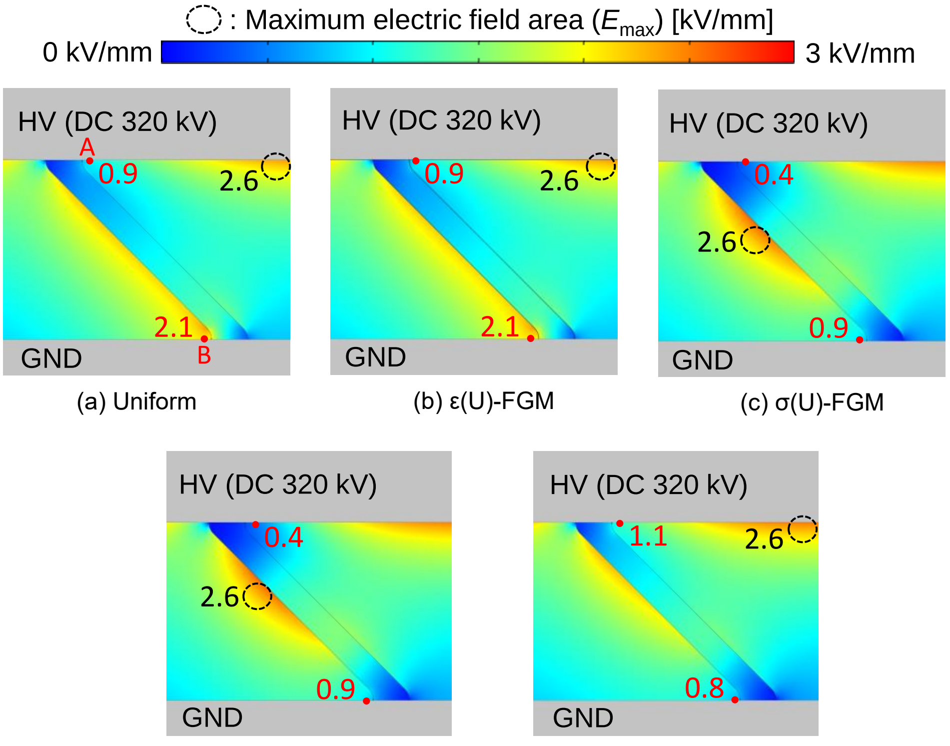

(a) Uniform (b) ε(U)-FGM (c) σ(U)-FGM

(d) ε(U)/σ(U)-FGM (e) ε(U)/σ(GHC)-FGM

Fig. 3.8 Electric field distribution under DC steady state (E_{+DC}) at ΔT=20 K.

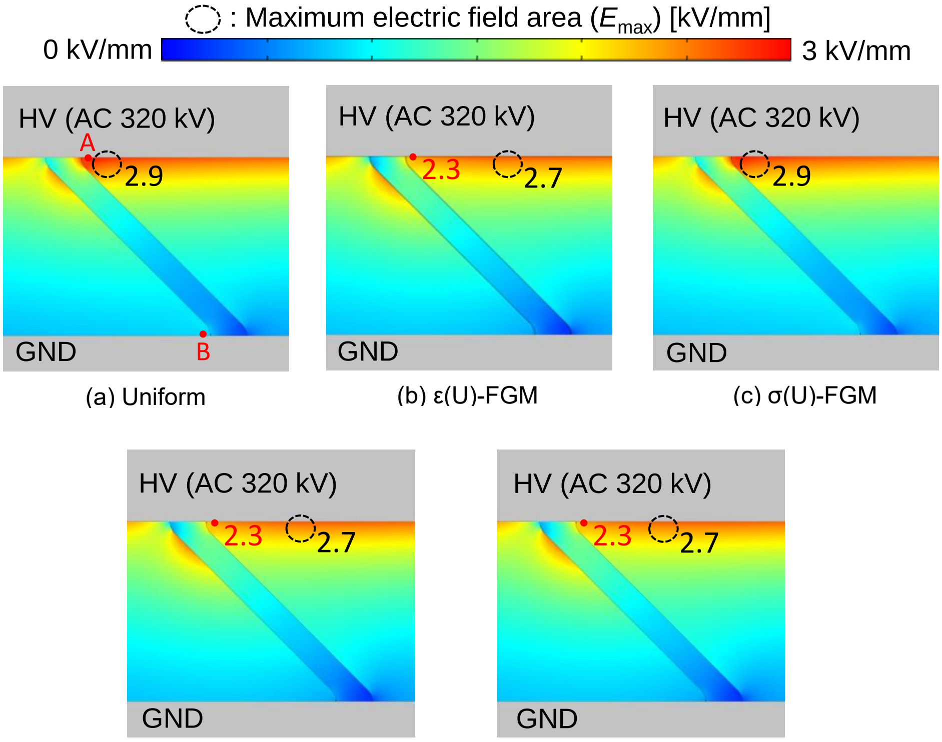

(a) Uniform (b) ε(U)-FGM (c) σ(U)-FGM

(d) ε(U)/σ(U)-FGM (e) ε(U)/σ(GHC)-FGM

Fig. 3.9 Electric field distribution under AC steady state (E_{AC}) at ΔT=20 K.

locations, i.e E_A is reduced from 0.9 kV/mm (Figs. 3.8(a) and (b)) to 0.4 kV/mm (Figs. 3.8(c) and (d)), and E_B is reduced from 2.1 kV/mm (Figs. 3.8(a) and (b)) to 0.8-0.9 kV/mm (Figs. 3.8(c), (d), and (e)).

The opposite phenomena can be seen in Fig. 3.9, which illustrates the capacitive field (E_{AC}) distribution. The FGM spacers with graded ε (Figs. 3.9(b), 3.9(d), and 3.9(e)) have lower E_{AC} around HV-TJ (E_A=2.3 kV/mm) compared to those of uniform and σ(U)-FGM spacers (E_A=2.9 kV/mm), owing to the higher ε of the spacer at the spacer/HV conductor interface.

Those E_{DC} and E_{AC} distributions around each spacer determine the electric field distribution at DC-PR (E_{PR}), as shown in Fig. 3.10, where E_{max} is found around the HV-TJ. Fig. 3.10(c) reveals that σ(U)-FGM spacer, which is effective in reducing E_{max} under DC steady state, shows, on the contrary, higher electric field stress (E_{PR}^{max}=5.4 kV/mm) compared to the Uniform spacer at DC-PR. This is because E_{AC} around uniform and σ(U)-FGM spacers remain the same (E_{max}=E_A=2.9 kV/mm in Figs. 3.9(a) and 3.9(c)) and E_{DC} of σ(U)-FGM spacer at that point is greatly reduced (E_A=0.4 kV/mm in Fig. 3.8 (c)). As a result, E_{PR}^{max} of σ(U)-FGM spacer is higher than that of the Uniform spacer.

Meanwhile, the FGM spacers with graded ε have suppressed E_{PR} (E_{PR}^{max}=3.9, 4.4, 3.6 kV/mm in Figs. 3.10(b), 3.10(d), and 3.10(e), respectively) compared to the Uniform spacer (E_{PR}^{max}=4.9 kV/mm in Fig. 3.10 (a)). Referring to Equation (3.9), the effect of E_{AC} is more dominant than E_{DC} under PR condition. Therefore, ε grading can reduce E_{AC} component, hence, E_{PR} is also lower than that of the Uniform or σ(U)-FGM spacers.

Particularly, ε(U)/σ(GHC)-FGM spacer results in the lowest maximum electric field strength at polarity reversal (E_{PR}^{max}=3.6 kV/mm in Fig. 3.10 (e)) among all other ε/σ-FGM spacers. This is due to the fact that higher σ in the spacer part near the ground side causes potential burden from the ground side shifted toward the middle and upper part of the spacer (near HV side) and slightly increases E_{DC} around those parts with lower σ (E_A= 1.1 kV/mm in Fig. 3.8 (e)). Therefore, the resulted E_{PR} near the HV-TJ of ε(U)/σ(GHC)-FGM spacer (E_A=3.5 kV/mm in Fig. 3.10(e)) is also reduced a little bit more compared to ε(U)-FGM or ε(U)/σ(U)-FGM spacers (E_A=3.8 and 4.3 kV/mm in Figs. 3.10(b) and (d), respectively).

Another way to understand that at DC-PR the capacitive field or E_{AC} is more dominant

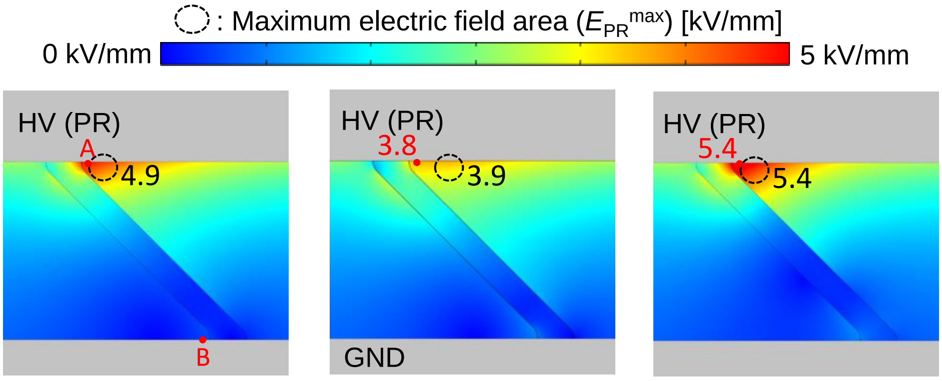

(a) Uniform (b) ε(U)-FGM (c) σ(U)-FGM

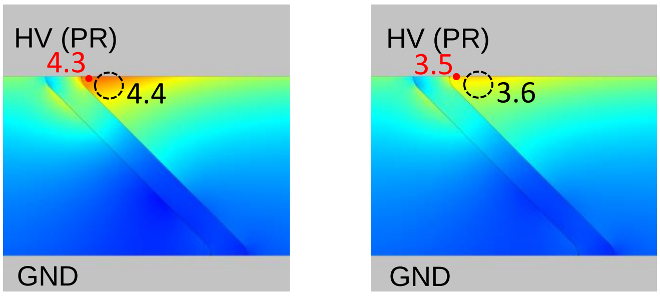

(d) ε(U)/σ(U)-FGM (e) ε(U)/σ(GHC)-FGM

Fig. 3.10 Electric field distribution under DC-PR (E_{PR}) at ΔT=20 K.

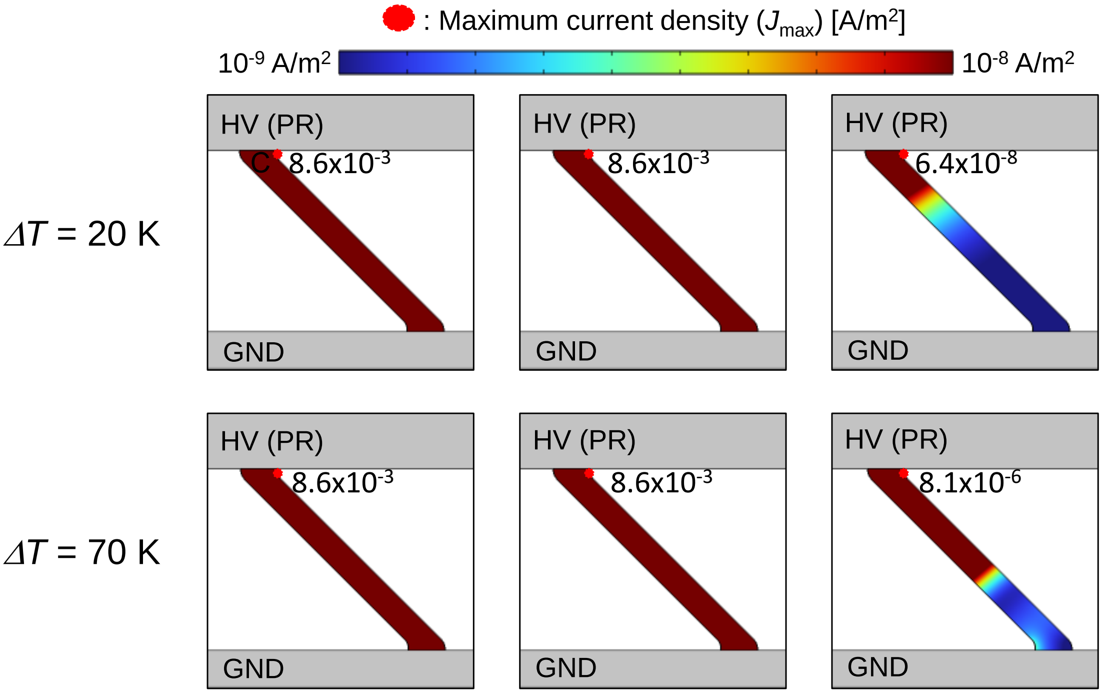

(a) J (b) J_d (c) J_C

Fig. 3.11 (a) Current density J, (b) Displacement current density J_d, and (c) Conduction current density J_c distribution at DC-PR around Uniform spacer at ΔT=20 and 70 K.

than the resistive field or E_{DC} is by monitoring the current density distribution. Fig. 3.11 shows (a) current density J, (b) displacement current density J_d, and (c) conduction current density J_c distribution within the Uniform spacer at ΔT=20 and 70 K when E_{PR}^{max} is reached. The same current distributions within the spacer in Fig. 3.11 (a) and (b) show that the overall current at DC-PR mostly consists of displacement current which affects the capacitive field. In addition, difference in temperature distribution does not have effect on the displacement current. On the other hand, Fig. 3.11(c) shows much smaller conduction current density compared to the displacement current density, but the effect of ΔT can be seen from the figure where the area with higher J_c within the spacer increase, as well as J_c^{max}. This is because J_c increases with σ which is influenced by temperature.

Fig. 3.12 shows time-varying J, J_d, and J_c at the Uniform spacer's concave surface near HV-TJ (Point C in Fig. 3.11 (a)) during DC-PR, since positive DC voltage is reversed until it reaches DC-SS (from +320 kV at t=10^6 s in Fig. 3.1). The graph in Fig. 3.12 (a) shows that at the beginning of DC-PR (t=0.001 s) to about t=10^5 s, J is almost equal with J_d. After $t > 10^5$ s, J_d keeps decreasing, while J_c increases, hence J approximately equals with J_c until it reaches DC-SS. This transition between displacement current to conduction current can also represent the transition between capacitive field to resistive field in electric field distribution.

Finally, in order to compare the effect of each FGM spacer, Fig. 3.13 shows E_{PR}^{max} against ΔT between HV and GND conductors. It can be concluded that at DC-PR, the largest reduction of E_{PR}^{max} at each ΔT is given by ε(U)/σ(GHC)-FGM spacer. The maximum E_{PR} reduction of ε(U)/σ(GHC)-FGM spacer is achieved by 30% at ΔT = 10 K compared to the Uniform spacer. Based on this result, for the next two simulation conditions (DC-on and superimposed lightning impulse on DC steady state), only the electric field analysis around ε(U)/σ(GHC)-FGM spacer, with comparison to the Uniform spacer, will be evaluated.

3.4.3 DC-On

The electric field analysis under DC-on condition is performed through time dependent simulation where positive 320 kV DC voltage is applied to the HV conductor within 0.01 s switching time. The electric field distribution and E_{max} are then evaluated over time until

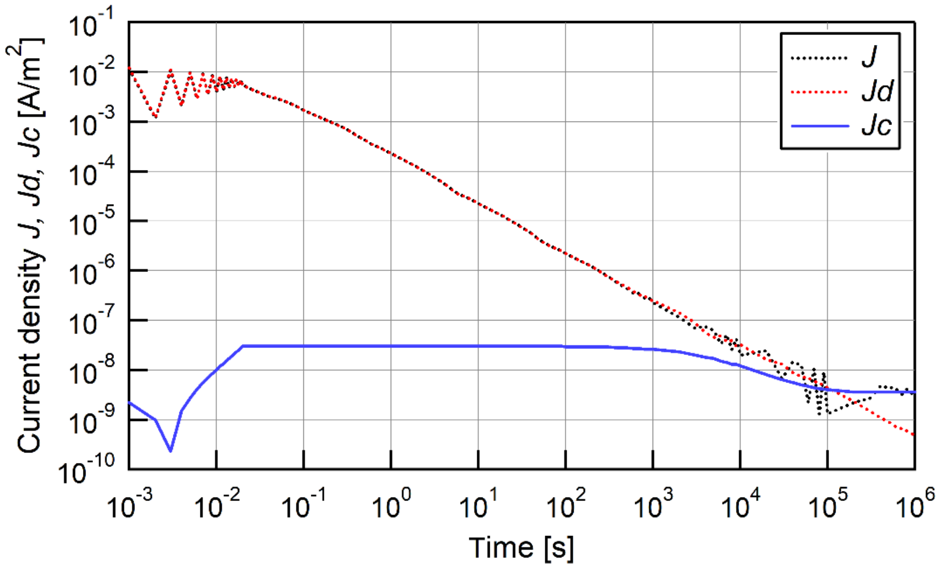

(a) Time in log x-axis

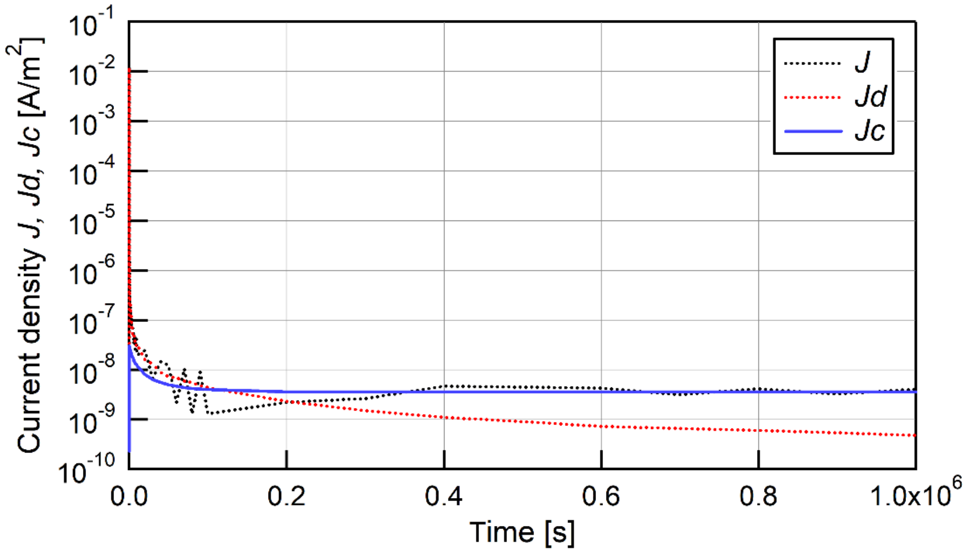

(b) Time in linear x-axis

Fig. 3.12 Current density *J*, displacement current density J_d, and conduction current density J_c distribution at DC-PR at point C of Uniform spacer at ΔT=20 and 70 K with (a) linear time axis, (b) log time axis

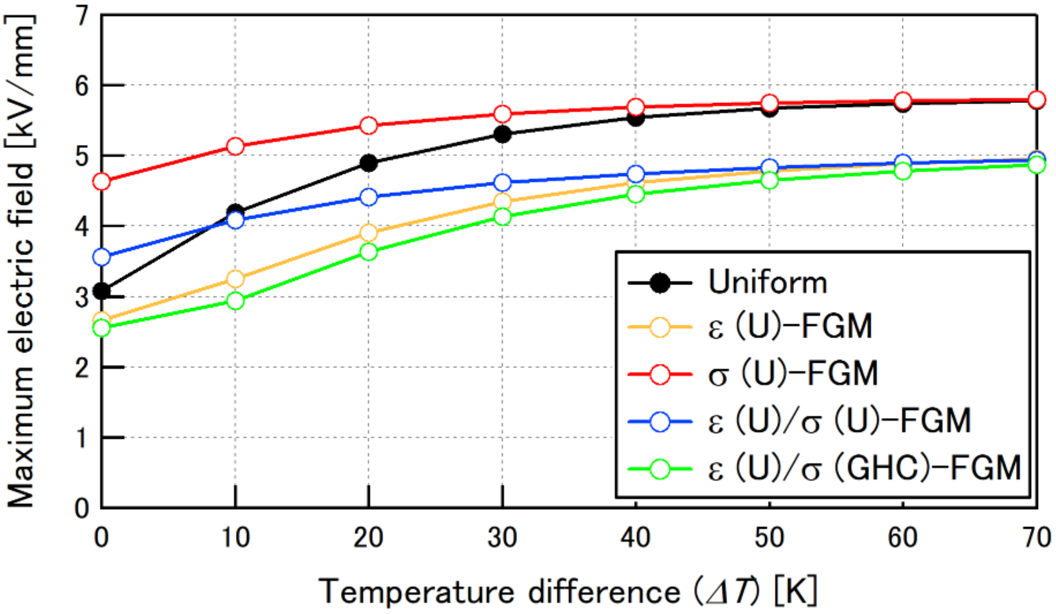

Fig. 3.13 E_{max} under DC-PR (E_{PR}^{max}) against temperature difference ΔT

it reaches DC steady state, particularly at points A and B, which are the critical points located at HV-TJ and GND-TJ, as illustrated in Fig. 3.3.

Figs. 3.14 and 3.15 show the E distribution around (a) uniform and (b) ε(U)/σ(GHC)-FGM spacers at different times for ΔT = 20 K and 70 K, respectively. At lower ΔT (ΔT = 20 K), the high E at early stage of the temporal transition ($t = 10^2$ s) since the voltage is applied, is concentrated near the HV-TJ (point A) and along the HV conductor surface for both spacers. As time passes, for the Uniform spacer, the high electric field stress is shifted toward point B at $t = 10^6$ s where the DC steady state has been already reached. However, for ε(U)/σ(GHC)-FGM spacer, the high electric field stress is concentrated on the middle part of the spacer at that time, so point B during DC steady state remains clear of high electric field stress.

The same situation also applies at higher ΔT (ΔT=70 K), as shown in Fig. 3.15. The high temperature enhances the σ of both spacers near the warm HV side, pushing the potential burden from the HV side toward the GND side. However, the higher σ of ε(U)/σ(GHC)-FGM spacer near the GND side is further enhanced with the temperature rise, causing the high electric field stress around point B reduced.

The electric field strength at both points A and B are more clearly distinguished in Fig. 3.16. At ΔT = 20 K (Fig. 3.16 (a)), as soon as DC voltage is applied, electric field strength of ε(U)/σ(GHC)-FGM spacer at point A is already lower than that of uniform spacer. This electric field reduction is caused by graded ε that has effect on E_{AC}. As time passes, electric field strength at point A decreases until it reaches the steady state. On the contrary, electric field strength at point B around the uniform spacer increases over time due to the displacement of field concentrations from the HV to the GND side. Nevertheless, electric field strength at point B around ε(U)/σ(GHC)-FGM spacer remains the same right from the beginning owing to the higher σ of the spacer near point B.

At ΔT = 70 K (Fig. 3.16 (b)), the time-varying electric field at points A and B evolves the same way as that at ΔT = 20 K, with higher increase of electric field strength at point B as the temperature increases. The transition time required for E_{AC} to shift into E_{DC} during DC-on can also be distinguished from the figures. As ΔT increases, this capacitive-resistive transition time of ε(U)/σ(GHC)-FGM spacer gets shorter.

Fig. 3.17 shows the time-varying $E_{\max}$ in gas around the (a) Uniform spacer and (b)

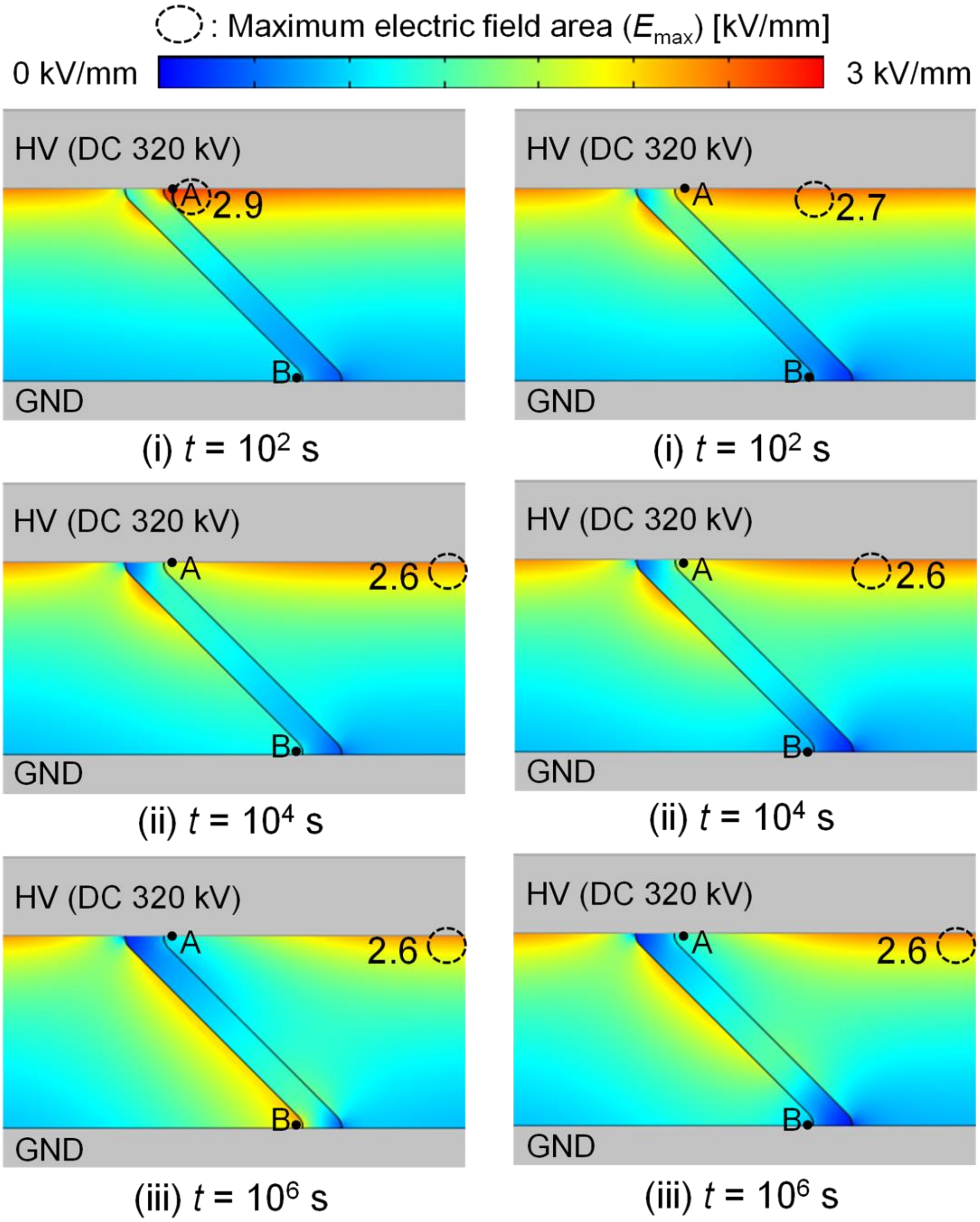

(a) Uniform

(b) ε(U)/σ(GHC)-FGM

Fig. 3.14 Electric field distribution around (a) the Uniform spacer and (b) ε(U)/σ(GHC)-FGM spacer during DC-on at ΔT=20 K

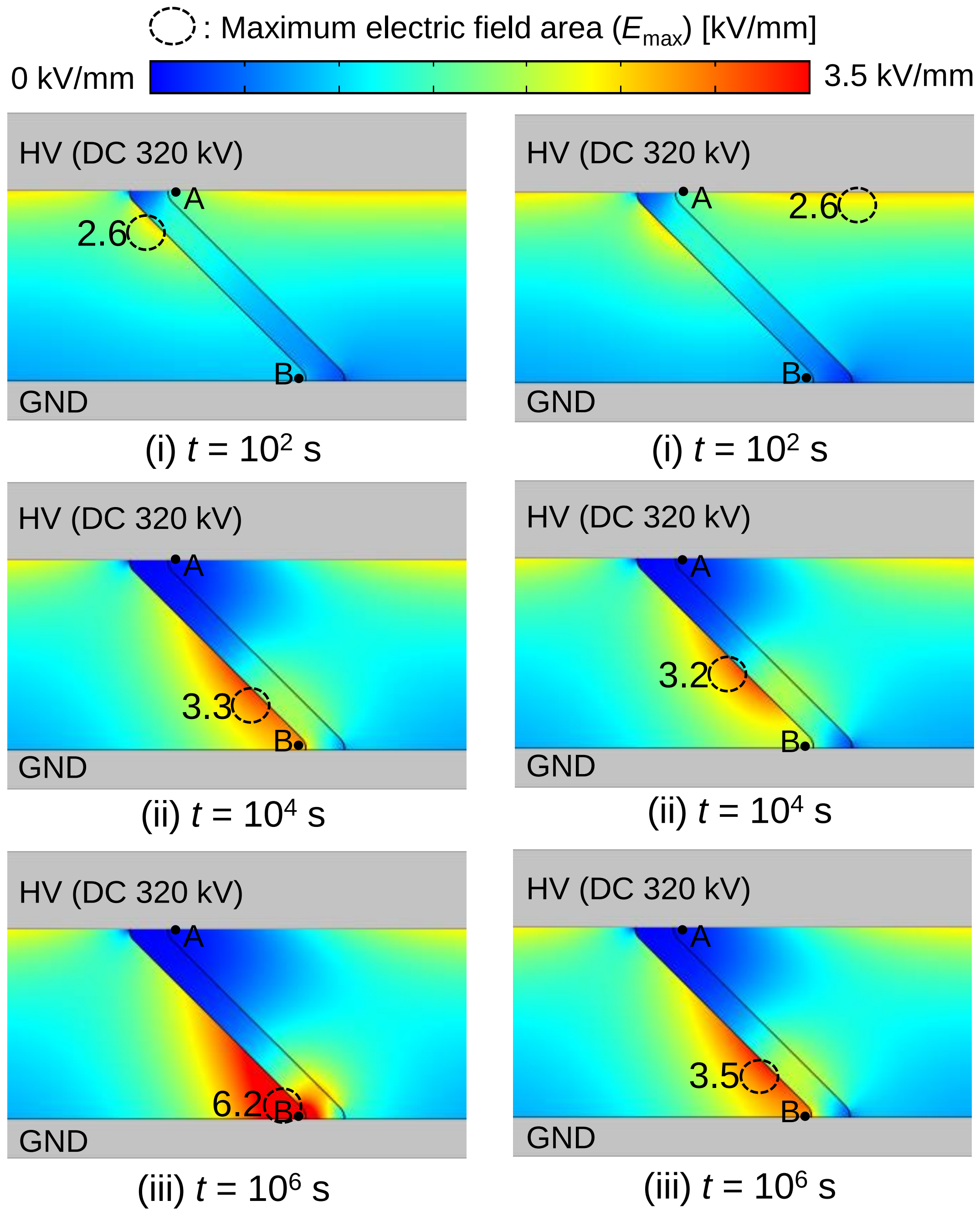

(a) Uniform

(b) ε(U)/σ(GHC)-FGM

Fig. 3.15 Electric field distribution around (a) the Uniform spacer and (b) ε(U)/σ(GHC)-FGM spacer during DC-on at ΔT=70 K

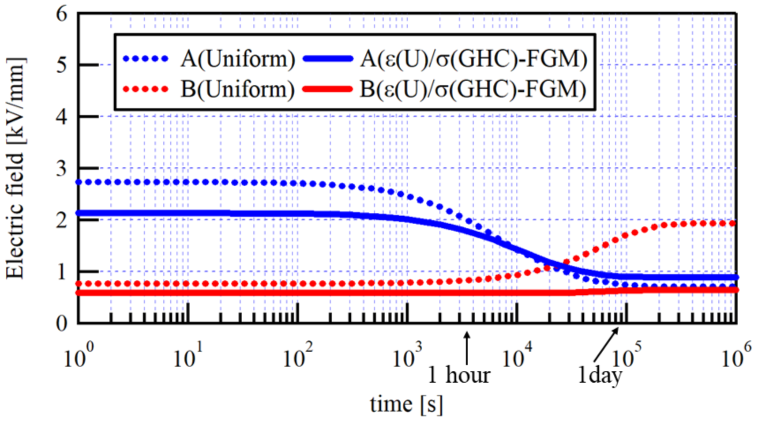

(a) ΔT=20 K

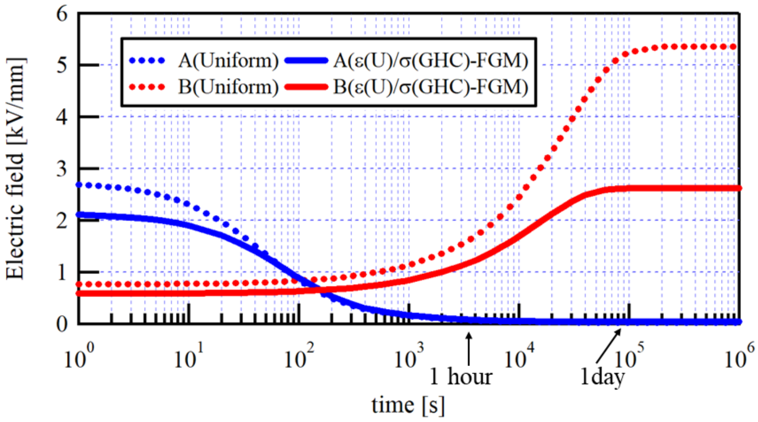

(b) ΔT=70 K

Fig. 3.16 Time varying electric field strength at point A near HV-TJ and at point B near GND-TJ of the Uniform and ε(U)/σ(GHC)-FGM spacers at: (a) ΔT=20 K, and (b) ΔT=70 K

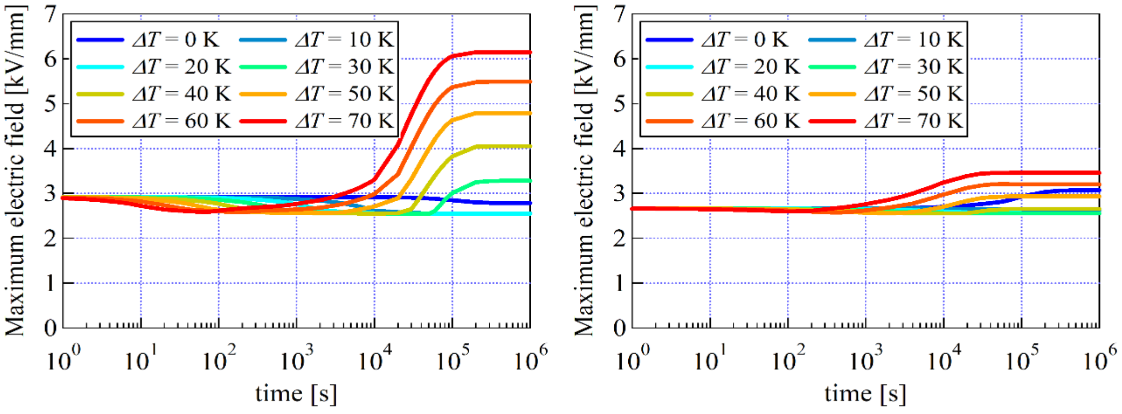

(a) Uniform

(b) ε(U)/σ(GHC)-FGM

Fig. 3.17 Time-varying $E_{\max}$ in SF_6 gas around (a) Uniform and (b) ε(U)/σ(GHC)-FGM spacers ε(U)/σ(GHC)-FGM spacers for different ΔT from 0–70 K. It is understood that both E_{AC} and E_{DC} of ε(U)/σ(GHC)-FGM spacer are relaxed than those of the Uniform spacer at each ΔT, which is indicated by the E_{max} location transition from point A to B. The E_{max} reduction is by 43% at ΔT= 70 K, which is consistent with that under DC steady state in the sub chapter 3.4.1.

3.4.4 Superimposed Lightning Impulse (LI) Voltage on DC Steady State

The electric field simulation under superimposed lightning impulse (LI) voltage on DC steady state is performed through time-dependent simulation, i.e., 320 kV DC voltage applied to the HV conductor until DC steady state is reached, then 1175 kV [11] positive and negative LI voltages are superimposed, as illustrated in Fig. 3.18.

Figs. 3.19 and 3.20 show electric field distribution around (a) the Uniform and (b) ε(U)/σ(GHC)-FGM spacers under superimposed standard positive and negative LI of 1175 $\mathrm{kV_{peak}}$ on 320 kV DC steady state condition, respectively. According to the figures, under both superimposed positive or negative LI voltage on DC steady state, and with or without ΔT, ε(U)/σ(GHC)-FGM can reduce the electric field stress around the HV-TJ and shift the E_{max} location away from the HV-TJ along the HV conductor surface.

In order to obtain the picture quantitatively, Fig. 3.21 (a) indicates the electric field strength at point A under different ΔT. Under both superimposed positive and negative LI voltages on DC steady state, the electric field strength at point A of ε(U)/σ(GHC)-FGM spacer is constantly lower than that of uniform spacer even with the higher ΔT. The electric field strength reduction is 1.6 kV/mm and 2.0 kV/mm under superimposed positive and negative LI, respectively.

Fig. 3.21(b) shows E_{max} under superimposed positive ($E_{\mathrm{+Imp}}$) and negative ($E_{\mathrm{-Imp}}$) LI voltage on DC steady state against ΔT. The maximum reduction of $E_{\mathrm{+Imp}}$ around ε(U)/σ(GHC)-FGM spacer is 7% at ΔT= 0 K. The decrease is due to graded ε of ε(U)/σ(GHC)-FGM spacer that reduces E_{AC} around HV-TJ. Meanwhile, the high σ at the GND side of the ε(U)/σ(GHC)-FGM spacer causes potential burden from GND side shifted toward HV side and increases E_{DC} around HV side. Consequently, the $\mathrm{E_{+Imp}}$ reduction by this FGM model is relatively small. When ΔT increases, E_{max} around either the Uniform or ε(U)/σ(GHC)-FGM spacers converges at approximately 11.9 kV/mm.

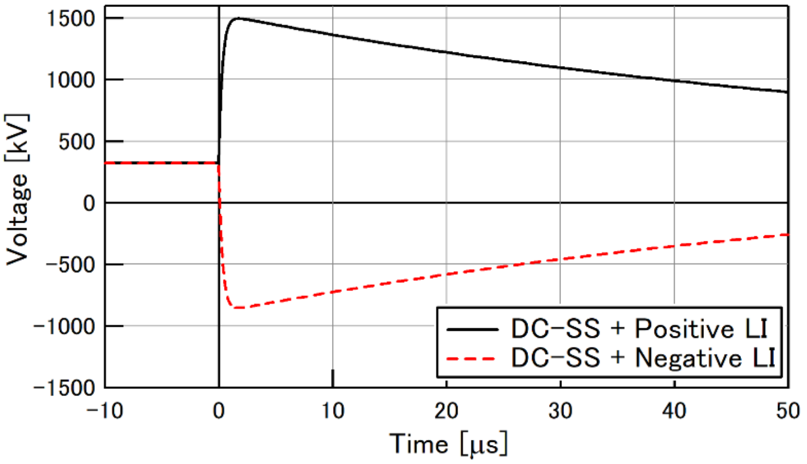

Fig. 3.18 Superimposed LI voltage on DC-SS.

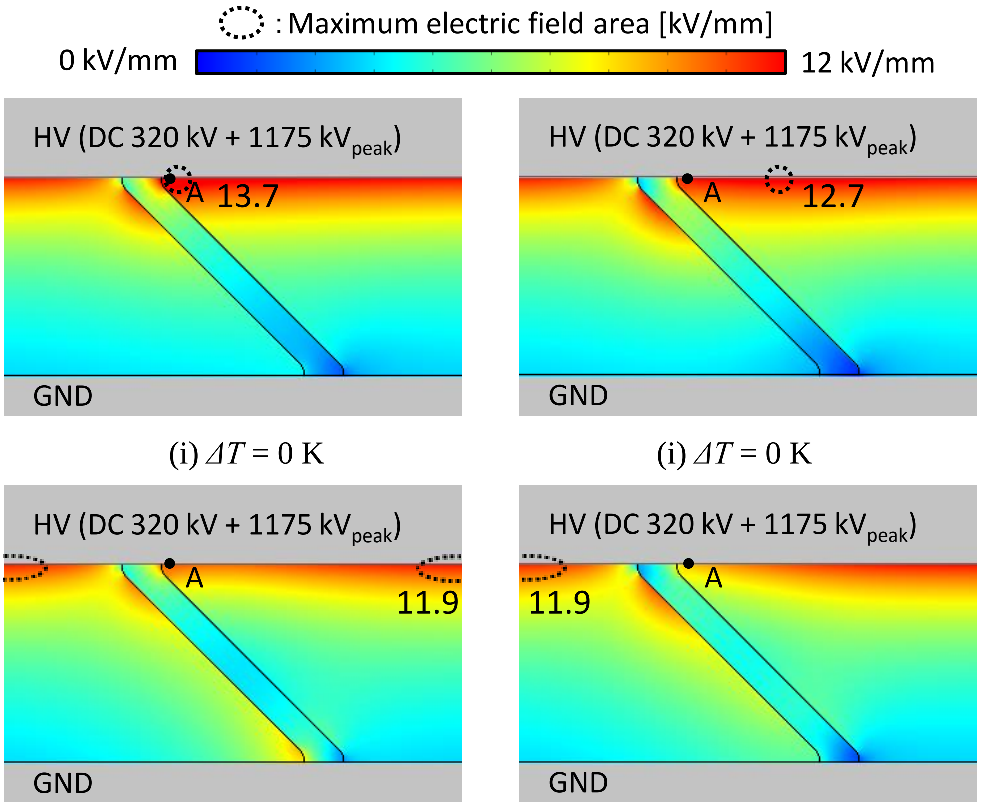

(i) $\varDelta T = 0$ K

(i) $\varDelta T = 0$ K

(ii) $\varDelta T = 70$ K

(a) Uniform

(ii) $\varDelta T = 70$ K

(b) ε(U)/σ(GHC)-FGM

Fig. 3.19 *E* distribution under superimposed positive LI on DC-SS

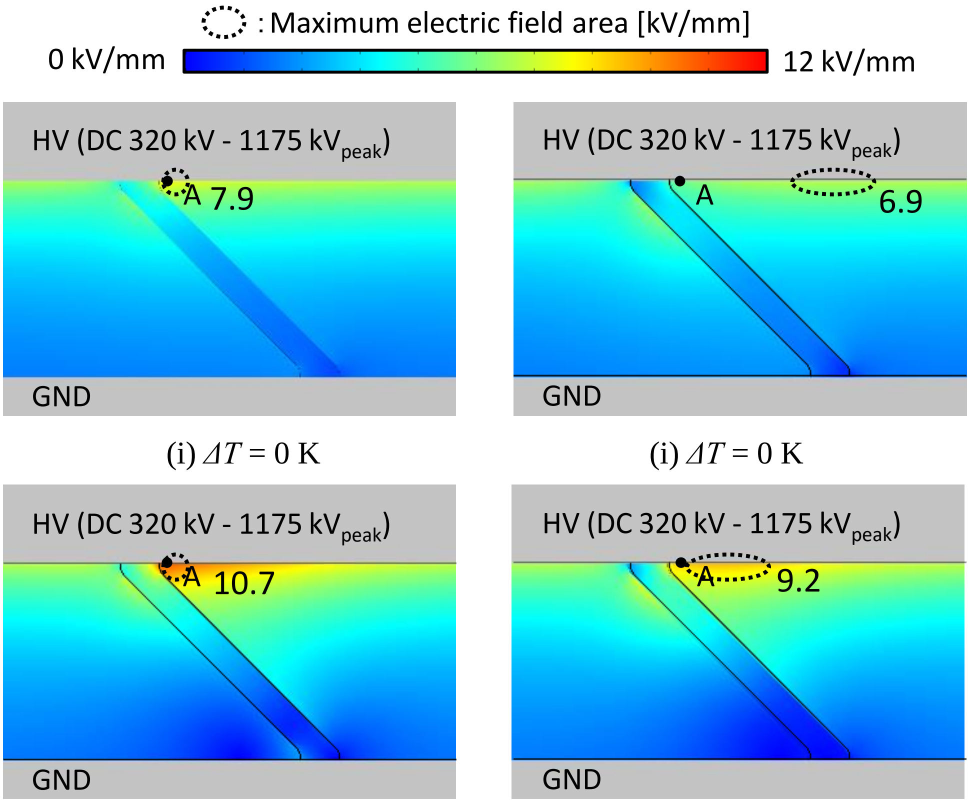

(i) $\Delta T = 0$ K (i) $\Delta T = 0$ K

(ii) $\Delta T = 70$ K (ii) $\Delta T = 70$ K

(a) Uniform (b) ε(U)/σ(GHC)-FGM

Fig. 3.20 *E* distribution under superimposed negative LI on DC-SS

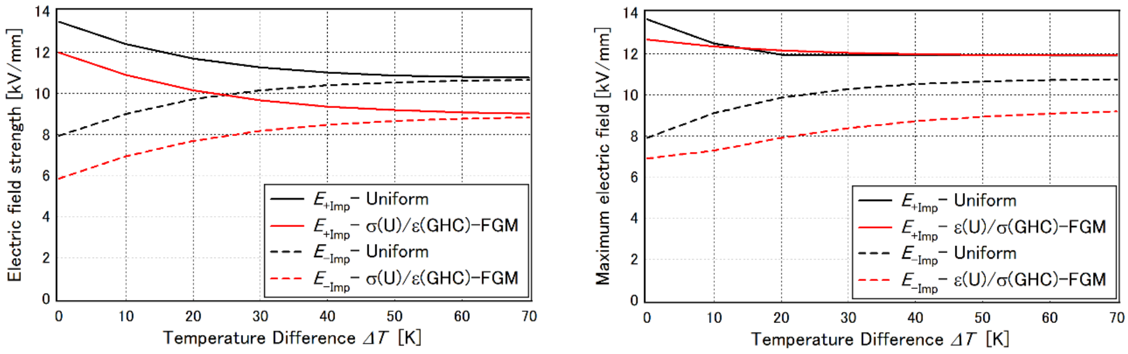

(a) *E* at point A (b) E_{max} in gas

Fig. 3.21 (a) *E* at point A, and (b) E_{max} in gas under superimposed positive and negative LI on DC-SS

This value is consistent with the theoretical value of E_{max} at inner conductor of an infinite coaxial cylinder electrodes.

Similar to the case of DC-PR, $E_{\text{-Imp}}$ around ε(U)/σ(GHC)-FGM spacer is constantly reduced despite the increase in ΔT. The highest $E_{\text{-Imp}}$ reduction by ε(U)/σ(GHC)-FGM application is 20% at $\Delta T = 10$ K.

3.5 Summary

FGM application with graded ε and σ in a DC GIS spacer has been proposed and the effectiveness in electric field relaxation has been evaluated under various DC operating conditions. Through electric field simulation, the following results are revealed:

1. FGM application with graded σ is effective for electric field relaxation under DC steady state operation. σ(U)-FGM and ε(U)/σ(GHC)-FGM spacers can reduce the E_{max} by 43% at ΔT of 70 K, compared to the Uniform spacer.
2. FGM application with both graded ε and σ is effective to reduce both resistive and capacitive field during other DC operating conditions with rapid voltage change over time, such as polarity reversal, DC-on, and superimposed positive and negative lightning impulse voltage on DC steady state. The new idea of ε(U)/σ(GHC)-FGM with low σ distribution near HV side of the spacer is currently evaluated as the most effective ε/σ distribution in reducing the E_{max} in gas compared to uniform spacer, particularly at DC-PR. It is validated through electric field simulations with E_{max} reduction of 30%, 43%, 7% and 20%, respectively, for each DC operating condition.

References

[1] H. Li, N. Zebouchi and A. Haddad, "Theoretical and practical investigations of spacer models for future HVDC GIS/GIL applications," in *Proceedings of the 21st International Symposium on High Voltage Engineering (ISH)*, Budapest, Hungary, 2019, vol. 2, pp.1538-1549.

[2] M. Hering, S. Grossmann, J. Speck and U. Riechert, "Investigation of the temperature influence on the breakdown voltage in gas insulated systems under DC voltage stress," in *Proceedings of the 18th International Symposium on High Voltage Engineering (ISH)*, Seoul, South Korea, 2013, OE7-2, pp. 1354-1359.

[3] M. Hering, K. Juhre, M. Secklehner and V. Hinrichsen, "Requirements on solid insulating materials and gas-solid interfaces in compact HVDC gas-insulated systems," in *The 20th*

International Symposium on High Voltage Engineering (ISH), OG1-3, Buenos Aires, Argentina, 2017.

[4] N. Hayakawa, R. Oishi, H. Kojima, K. Kato and N. Zebouchi, "Electric field grading by Functionally graded materials (FGM) for HVDC gas insulated power apparatus," in *2018 IEEE Conference on Electrical Insulation and Dielectric Phenomena (CEIDP)*, Cancun, Mexico, 2018, 5-4, pp. 390-393.

[5] U. Riechert, U. Straumann, R. Gremaud and M. Callavik, "Compact gas-insulated systems for high voltage direct current transmission: design and testing," in *IEEE PES Transmission & Distribution Conference & Exposition*, Dallas, USA, 2016, pp.1-5.

[6] U. Riechert, U. Straumann and R. Gremaud, "Compact Gas-insulated Systems for High Voltage Direct Current Transmission: Basic Design," in *IEEE/PES Transmission and Distribution Conference and Exposition (T&D)*, Dallas, USA, 2016, pp.1-5.

[7] N. Hayakawa, Y. Miyaji, H. Kojima and K. Kato, "Simulation on Discharge Inception Voltage Improvement of GIS Spacer with Permittivity Graded Materials (ε-FGM) Using Flexible Mixture Casting Method," *IEEE Transactions on Dielectrics and Electrical Insulation*, vol. 25, no. 4, pp. 1318-1323, 2018.

[8] A. Küchler, High voltage engineering Fundamentals-Technology-Applications, Berlin, Germany: Springer Vieweg, 2017.

[9] R. Nakane, K. Takabayashi, K. Kato and H. Okubo, "Electrical Insulation Performance of HVDC-GIS Spacer Under Various Testing Conditions," in *2017 IEEE Conference on Electrical Insulation and Dielectric Phenomenon (CEIDP)*, Fort Worth, USA, 2017, 7-6, pp. 621-624.

[10] N. Hayakawa, J. Ishiguro, H. Kojima, K. Kato and H. Okubo, "Fabrication and Simulation of Permittivity Graded Materials for Electric Field Grading of Gas Insulated Power Apparatus," *IEEE Transactions on Dielectrics and Electrical Insulation*, vol. 23, no. 1, pp. 547-554, 2016.

[11] H. Koch, D. Imamovic, B. Lutz, K. Juhre, T. Neidhart and R. -D. Rogler, "High power underground transmission for HVDC," in *CIGRE Session SC B3-104*, Paris, France, 2016, pp.1-11.

Chapter 4 Electric Field Relaxation and Breakdown Voltage Improvement on DC GIS/GIL Spacer with ε/σ-FGM

4.1 Introduction

In Chapter 3, the preliminary study of ε/σ-FGM effectiveness on a 320 kV HVDC GIS spacer model [1,2] is discussed based on electric field simulation results. In those simulations, the conductivity model is based on the reference data [3,4] of epoxy insulating material which has relatively higher temperature dependency (*W*=0.95 eV) and lower electric field dependency (*a*=0.08 mm/kV). However, the conductivity measurement results of SiC-filled epoxy composite which are considered as materials for FGM spacers show that the temperature and electric field dependency change with SiC filler contents. The σ measurement results have shown that *T*-dependence coefficient (*W*) decrease with SiC filler contents, while *E*-dependence coefficient (*a*) increase with SiC filler contents. *W* of non-SiC-filled epoxy composite itself is 0.63 eV, which is lower than the typical *W* value of epoxy resin (0.95 eV). The difference between these values can be due to SiO_2 filler contents which are contained in the bulk samples in this research, while the reference value of *W* does not mention whether the epoxy resin is filled with conventional fillers or not. Another possibility is that the σ measurement in this research have not yet reached the actual end value of steady state (measurement time is 50-70 minutes). Nevertheless, according to [5], the steady-state end value of conductivity at room temperatures can be identified only after very long times of several hours, days, or even weeks, while at higher temperatures, it can be identified earlier. It could mean that the actual σ of non-SiC-filled epoxy composite at *T*=303 K is much lower than the currently measured value, hence higher *W* value.

On the other hand, *E*-dependence coefficient (*a*) which also shows the nonlinearity of the material's conductivity increase with SiC filler contents. Based on percolation theory, filler particles in a matrix can form a conductive network once the filler concentration is large enough. Composite with higher SiC filler content has more conduction paths formed inside the bulk sample, and the distance between adjacent SiC particles decrease as well.

This leads to larger current flow at the same or lower electric field strength (high nonlinearity, lower switching field). Therefore, *a* increases with SiC filler contents [6, 7].

The different characteristics between σ obtained from measurement in Chapter 2 and σ based on reference papers in Chapter 3 may lead to different results in E relaxation effects. Therefore, in this chapter, the feasibility of ε/σ-FGM spacer is evaluated based on actual measured ε and σ characteristics of $SrTiO_3$-filled and SiC-filled epoxy composites, respectively. In addition, for future fabrication and experimental verification of ε/σ-FGM spacer, electric field simulations are performed on a scaled model DC GIS/GIL cone type spacer [8] to reveal the insulation performance of ε/σ-FGM spacers in σ-controlled resistive fields under DC steady state (DC-SS), both σ and ε-controlled fields under DC-PR and superimposed lightning impulse (LI) on DC-SS, and ε-controlled capacitive fields under LI voltage applications in addition to those at DC-on.

Furthermore, in order to make sure that thermal runaway do not occur due to internal heating in ε/σ-FGM spacer, the temperature increase and maximum level of SiC filler contents are investigated. Then finally, to estimate the breakdown voltage, the theoretical discharge inception voltage (TDIV) of ε/σ-FGM spacer is also calculated under LI voltage in comparison with the Uniform spacer with constant ε and σ.

4.2 ε and σ Distributions of Scaled ε/σ-FGM Spacer Model

Fig. 4.1 shows the scaled model of DC GIS/GIL cone type spacer with the same configuration and size as those of 1/4-scaled 245 kV AC GIS model [8], in which the ε characteristics of $SrTiO_3$-filled epoxy composite and σ characteristics of SiC-filled epoxy composite are implemented. The Flexible Mixture Casting (FMC) method which has been used to fabricate AC ε-FGM spacer in the past research works allows us to control ε and σ distributions independently, where grading to lower permittivity (GLP)-type ε distribution and U-shaped σ distribution are applied to ε/σ-FGM spacer, as illustrated in Figs. 4.1 (b) and (c), respectively.

Fig. 4.1 (b) shows that ε_r is graded from $\varepsilon_{r(max)}$ of 12.7 at the HV conductor/spacer interface, to $\varepsilon_{r(min)}$ of 4.0 at the GND/spacer interface [5,6]. Table 4.1 shows the compositions of $SrTiO_3$ and SiO_2 filler contents in comparison to the total volume of epoxy composite, in order to result in high and low ε_r composites of 12.7 and 4.0, respectively, according to Fig. 2.10 (in Section 2.6) as the ε_r characteristics of $SrTiO_3$-filled epoxy composite as a function of $SrTiO_3$ filler contents. The GLP-type ε distribution is considered in order to effectively suppress the capacitive electric field around the edge of shield electrode in the concave side owing to the higher ε_r of the spacer around that area. In this case, ε_r characteristics of SiC-filled epoxy composite can be neglected, since it is smaller than that of $SrTiO_3$-filled epoxy composite (see Sections 2.5.2 and 2.6).

Table 4.1 shows the compositions of $SrTiO_3$ and SiO_2 filler contents in comparison to the total volume of epoxy composite, in order to result in high and low ε_r composites of 12.7 and 4.0, respectively, according to Fig. 2.10 (in Section 2.6) as the ε_r characteristics of $SrTiO_3$-filled epoxy composite as a function of $SrTiO_3$ filler contents. The GLP-type ε distribution is considered in order to effectively suppress the capacitive electric field around the edge of shield electrode in the concave side owing to the higher ε_r of the spacer around that area. In this case, ε_r characteristics of SiC-filled epoxy composite can be neglected, since it is smaller than that of $SrTiO_3$-filled epoxy composite (see Sections 2.5.2 and 2.6).

Similarly, U-type σ distribution (Fig. 4.1 (c)), which is given by U-type distribution of 5 to 10 vol% SiC-filled epoxy composite (Fig. 4.1 (d)), has the higher σ around the HV conductor/spacer interface, so that the resistive electric field is distributed more uniformly to the area with the lower σ. However, in σ distribution, it is equally important to increase σ of the spacer at the GND/spacer interface, because with the presence of temperature distribution in the spacer, the equipotential lines are more likely to concentrate around the GND side. Keeping σ high at both ends of the spacer, i.e., U-type σ distribution will make the potential burden settled in the middle part of the spacer with lower σ [10].

Despite the results in Chapter 3 showing that GHC-type σ distribution as more effective for E relaxation, particularly at DC-PR, σ(GHC)-FGM spacer still has higher $E_{\max}$ values under DC-SS at lower ΔT compared to σ(U)-FGM and Uniform spacers (Fig. 3.7). However, in the current E simulation, by applying σ characteristics of 5 to 10 vol% SiC-filled epoxy composite, the base σ level of ε/σ-FGM spacer is almost 100 times higher than that of the Uniform spacer (Fig. 4.1 (c)) and the T-dependency is low. It is expected that σ(U)-FGM can result in significant E reduction at any voltage application, including DC-PR, and at any given ΔT.

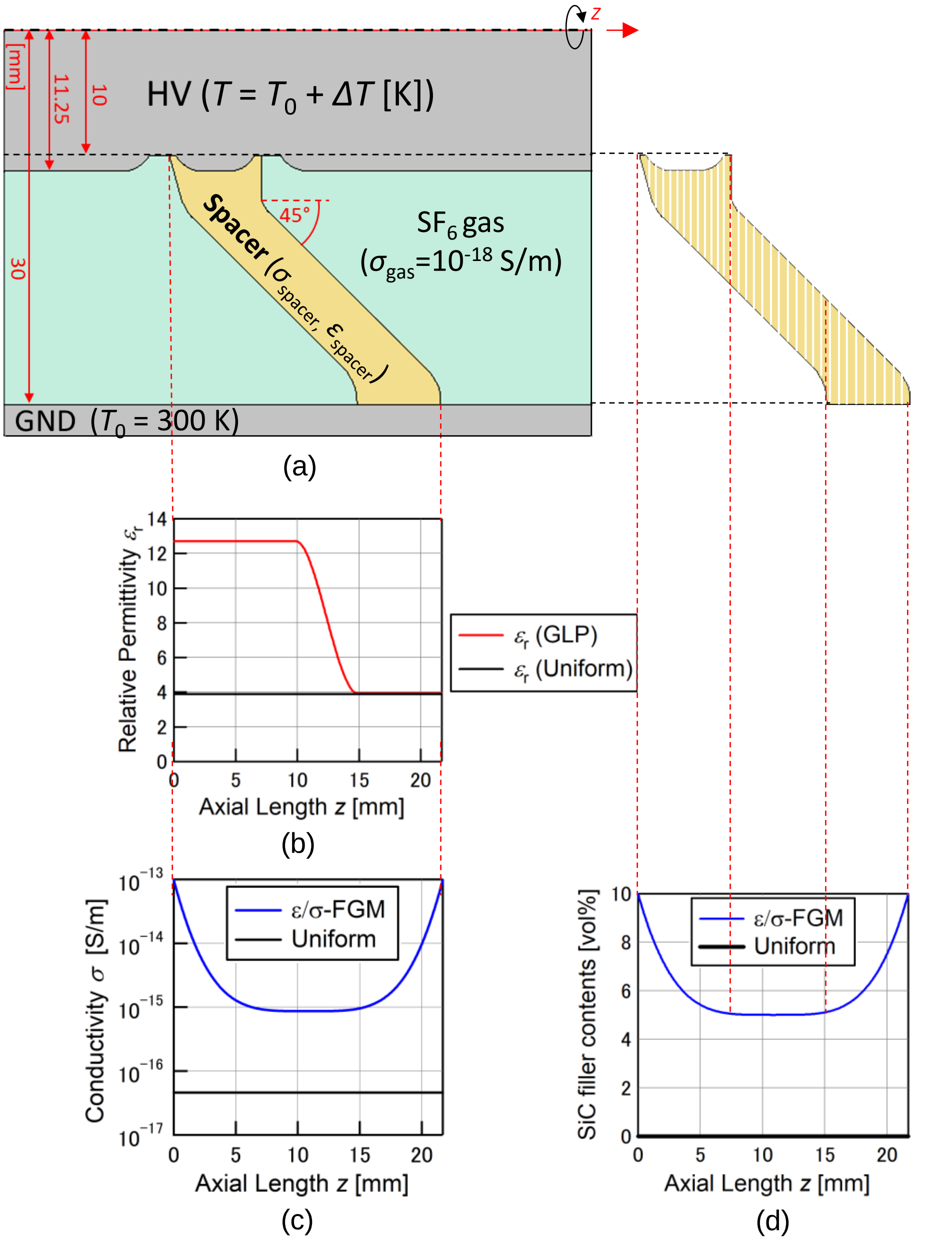

Fig. 4.1 (a) Scaled model of HVDC GIS spacer with (b) ε_r distribution, (c) σ distribution (at T=300 K and E=1 kV/mm) and the respective (d) SiC filler contents distribution of ε/σ-FGM and the Uniform spacers

Table 4.1 Composition of epoxy composite for ε grading

Relative permittivity ε_r	$SrTiO_3$ filler contents [vol%]	SiO_2 filler contents [vol%]
12.7	26.9	13.4
4.0	0	41.7

In addition, σ characteristics of $SrTiO_3$-filled epoxy composite have also been measured and confirmed to be less effective than those of SiC-filled epoxy composite (see section 2.7), hence they are not considered in this electric field simulation.

The simulation method, equations, and voltage application types are the same as those in Table 3.1 and section 3.2. However, due to the different spacer size, the voltage levels from 320 kV HVDC GIS spacer (320 kV for DC-SS and 1175 kV_{peak} for superimposed LI voltage) are scaled down following the ratio of spacer size (distance between HV electrode surface to inner surface of GND enclosure) of the 320 kV DC GIS spacer and the current scaled model. Then, 27 kV for DC-SS and 100 kV_{peak} for superimposed LI voltage are obtained to correspond approximately to the electric field strength to that of 320 kV HVDC GIS spacer [11].

4.3 Electric Field Simulation Results

4.3.1 DC Steady State

Under DC-SS condition, 27 kV DC-SS is applied on the HV conductor. Then electric field distribution and E_{max} around the spacer are monitored with changing temperature difference (ΔT) between HV and GND conductors from 0 to 70 K. Fig. 4.2 shows electric field distribution images around the Uniform and ε/σ-FGM spacers at ΔT of 0 K, 40 K, and 70 K. The black dot in the figures show the E_{max} locations in gas. Together with graph in Fig. 4.3 that shows E_{max} trend against ΔT, the following phenomena are explained.

E_{max} of the Uniform spacer first decreases at ΔT=0 to 20 K, but then gradually increases at ΔT=30 to 70 K. The first decline is caused by the temperature rise around the HV conductor/spacer interface that enhances σ of the spacer there, causing E_{max} location on the shield edge at ΔT=0 K (point A in Fig. 4.2 (a)) to be slightly pushed aside from the shield edge at ΔT=10 K (point B in Fig. 4.2 (a)), and pushed away onto the curved area of the spacer's convex surface at ΔT=20 K (point C in Fig. 4.2(a)). As the electric field strength declines with increased distance from the HV conductor, E_{max} around the Uniform spacer at ΔT=10 to 20 K is smaller than that at ΔT=0 K. Then, E_{max} location is shifted to point D near the GND/spacer interface with increasing magnitude as ΔT increases from 30 K to 70 K, as shown in Fig. 4.2 (a) center and bottom images.

The significant change of electric field distribution with ΔT around the Uniform spacer

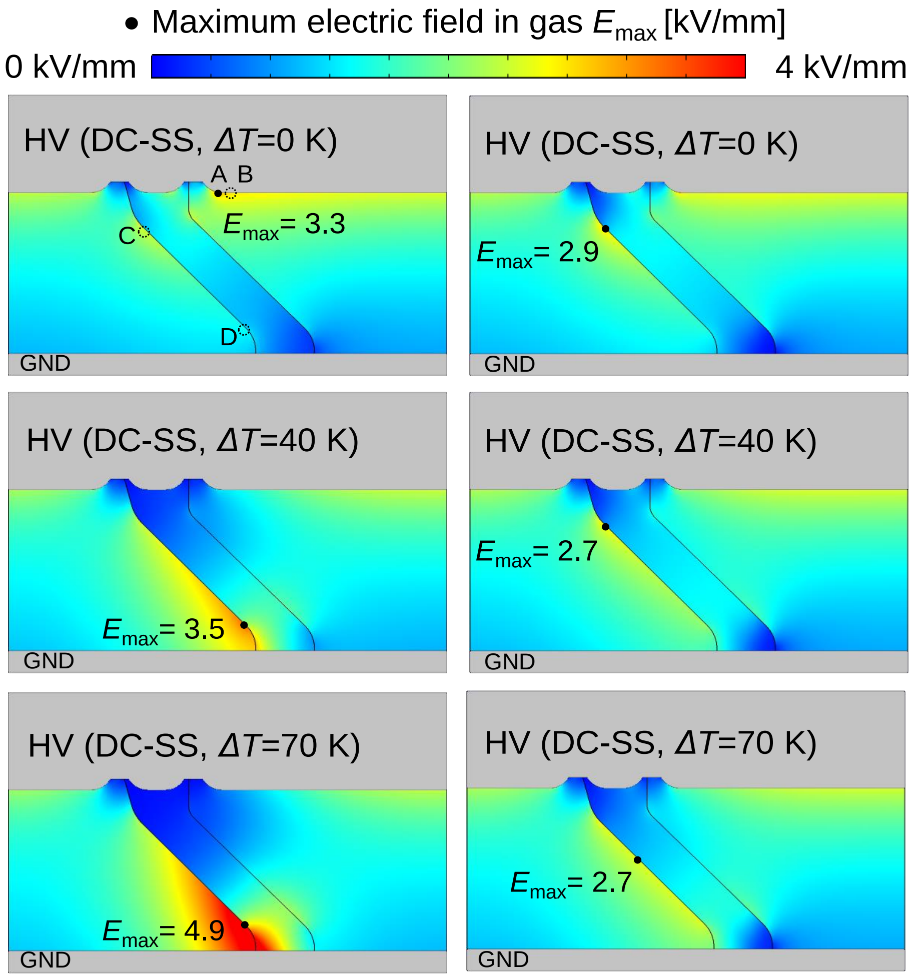

(a) Uniform spacer

b) ε/σ-FGM spacer

Fig. 4.2 Electric field distribution around (a) Uniform and (b) ε/σ-FGM spacers under 27 kV DC-SS at ΔT=0, 40, and 70 K.

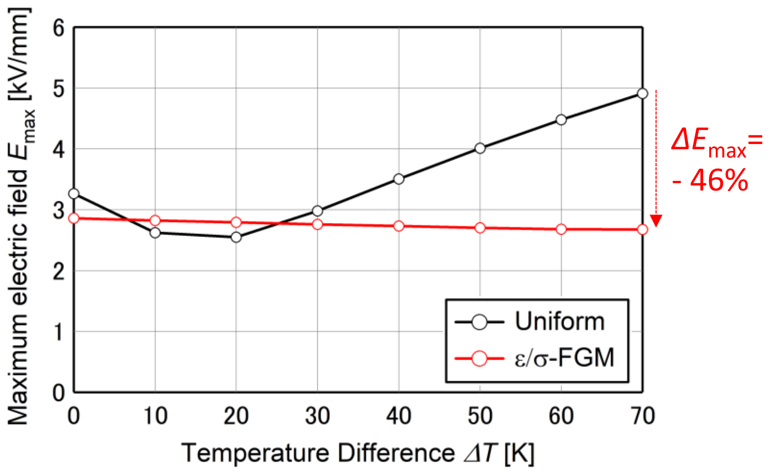

Fig. 4.3 E_{max} in gas under DC-SS with varying ΔT.

is consistent with higher T-dependent σ characteristics at 0 vol% SiC-filled epoxy composite in Fig. 2.7 (Section 2.4.2). As ΔT increases, more volume of the Uniform spacer near the HV side has enhanced σ, causing potential burden pushed toward the spacer part near the GND side with lower σ (Fig. 4.2 (a)). On the other hand, ε/σ-FGM spacer has almost constant suppression of $E_{\max}$ around ε/σ-FGM spacer owing to higher σ at the spacer part near the HV and GND conductors. Even the middle part of the spacer has higher σ than the Uniform spacer (Fig. 4.1 (c)). Consequently, $E_{\max}$ location of ε/σ-FGM spacer appears on the spacer's convex surface with lower σ, that shifts slightly toward the middle as ΔT increases, hence the magnitude of $E_{\max}$ is also reduced (Fig. 4.2 (b)). The largest $E_{\max}$ reduction around the ε/σ-FGM spacer is 46%, compared to the Uniform spacer, which is reached at ΔT=70 K.

Fig. 4.3 shows that $E_{\max}$ in gas around ε/σ-FGM spacer are constantly decreasing with the increase of ΔT, compared to $E_{\max}$ in gas around the Uniform spacer that tend to increase at $\Delta T > 20$ K. The electric field grading of ε(GLP)/σ(U)-FGM spacer compared to the Uniform spacer in Fig. 4.1 shows even better results than that of ε(U)/σ(U)-FGM spacer in Fig. 3.7 (see Section 3.4.1). It is because the current ε(GLP)/σ(U)-FGM spacer model has higher σ at all spacer's part compared to the Uniform spacer, given by 5 to 10 vol% SiC-filled epoxy composite (Fig. 4.1 (c)). Meanwhile, the ε(U)/σ(U)-FGM model in Fig.3.3 has the same base σ level as the Uniform spacer, as well as higher T-dependency.

4.3.2 DC Polarity Reversal

Fig. 4.4 shows the electric field distribution around the Uniform and ε/σ-FGM spacers at ΔT of 0, 40, and 70 K. First, at DC-PR both capacitive fields (E_{AC}) and resistive fields (E_{DC}) present. The GLP-type ε distribution has an advantage compared to the U-type or the constant one (Uniform), because GLP-type has high ε_r of 12.7 maintained from the spacer/HV conductor's interface until the middle part of the spacer. Consequently, E_{AC} component around the concave surface of HV side is largely reduced, shifting the $E_{\mathrm{PR}}^{\max}$ location to the concave surface of GND side, as can be seen in the upper figure of Fig. 4.4 (b). On the contrary, the $E_{\mathrm{PR}}^{\max}$ is found at the shield edge around the Uniform spacer, due to low ε throughout the spacer, allowing the potential burden concentrated around the concave surface near HV conductor. As ΔT increases, E_{DC} component around both spacers' part near HV conductor are further reduced due to higher σ, although the reduction for ε/σ-FGM spacer is not as large as the Uniform spacer because of the lower T-dependency. This E_{DC} reduction is indicated by the deep blue color in Fig. 4.4 (a), (b) around the HV conductor. In the PR case, E_{DC} has inverse polarity with 2×E_{AC}. As a result, E_{PR} around the spacer of HV side increases with ΔT, as shown in Fig. 4.4.

The E_{PR}^{max} location is always at the shield edge near concave surface of the Uniform spacer. However, for ε/σ-FGM spacer, at ΔT =0 to 20 K, the E_{PR}^{max} location is on the convex surface near GND enclosure, due to reduced E_{AC} component around the spacer/HV interface up to the middle part of the spacer. E_{DC} component slightly increases with ΔT, hence the magnitude of E_{PR} is reduced. However, as ΔT is further increased from 30 K to 70 K, the potential burden driven by conductivity is shifted more toward the GND side, leaving E_{DC} component around HV conductor keep on decreasing. Therefore, E_{PR} becomes larger in the HV side, with E_{PR}^{max} location is back to the shield edge (Fig. 4.4 (b) middle and lower figures).

Fig. 4.5 shows the maximum electric field strength in gas (E_{PR}^{max}) at DC-PR against increasing ΔT around the Uniform and ε/σ-FGM spacers, which is obtained from equation (3.9) (See Section 3.2). In the previous DC-PR simulation (Section 3.4.2), all of the Uniform and ε/σ-FGM spacers with different ε/σ distribution show significant increase of E_{PR}^{max} with increasing ΔT, where the most effective ε(U)/σ(GHC)-FGM spacer has 2.3 kV/mm increase in E_{PR}^{max} from ΔT=0 K to ΔT=70 K. Meanwhile, in the current ε(GLP)/σ(U)-FGM spacer, E_{PR}^{max} shows only a small change with varying ΔT, with average E_{PR}^{max} of 2.9 ± 0.3 kV/mm. It is possible due to effective combination of ε/σ characteristics of $SrTiO_3$-filled epoxy composite and SiC-filled epoxy composite, which will be discussed in detail as follows. The E_{PR}^{max} of ε/σ-FGM spacer is reduced by 11 to 47% compared to that of Uniform spacer.

4.3.2 DC-On

The electric field distribution at DC-on is obtained by time-dependent simulation where the applied voltage on HV conductor rises from 0 to 27 kV in the time span of 0.01 s. Fig. 4.6 shows the time-varying E_{max} in gas around (a) Uniform spacer, and (b) ε/σ-FGM spacer at various ΔT. At DC-on, there are only E_{AC} present around the medium. As

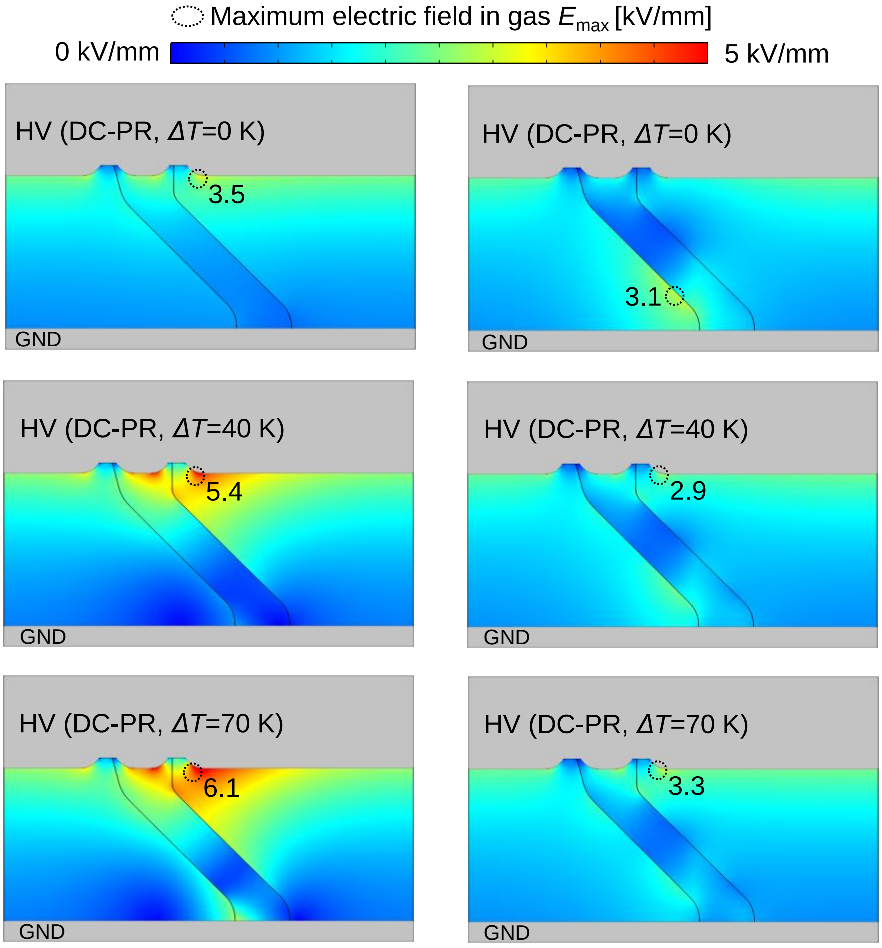

(a) Uniform spacer

(b) ε/σ-FGM spacer

Fig. 4.4 Electric field distribution around (a) Uniform and (b) ε/σ-FGM spacers under at DC Polarity Reversal when ΔT=0, 40, and 70 K.

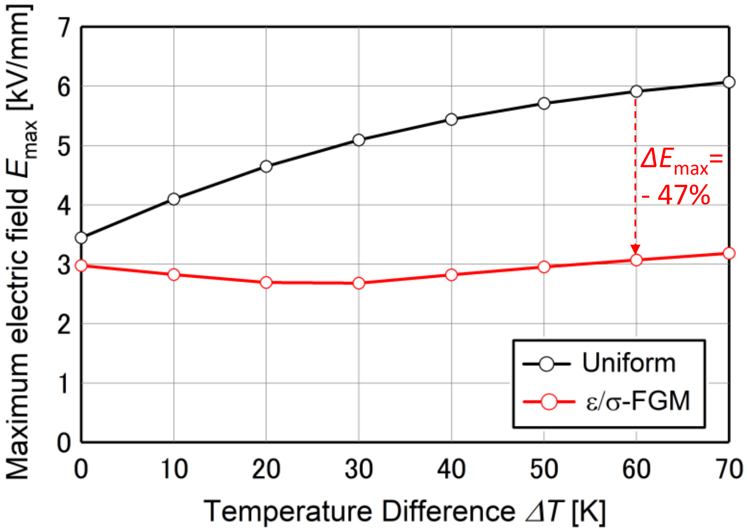

Fig. 4.5 E_{max} in gas at DC-PR with varying ΔT.

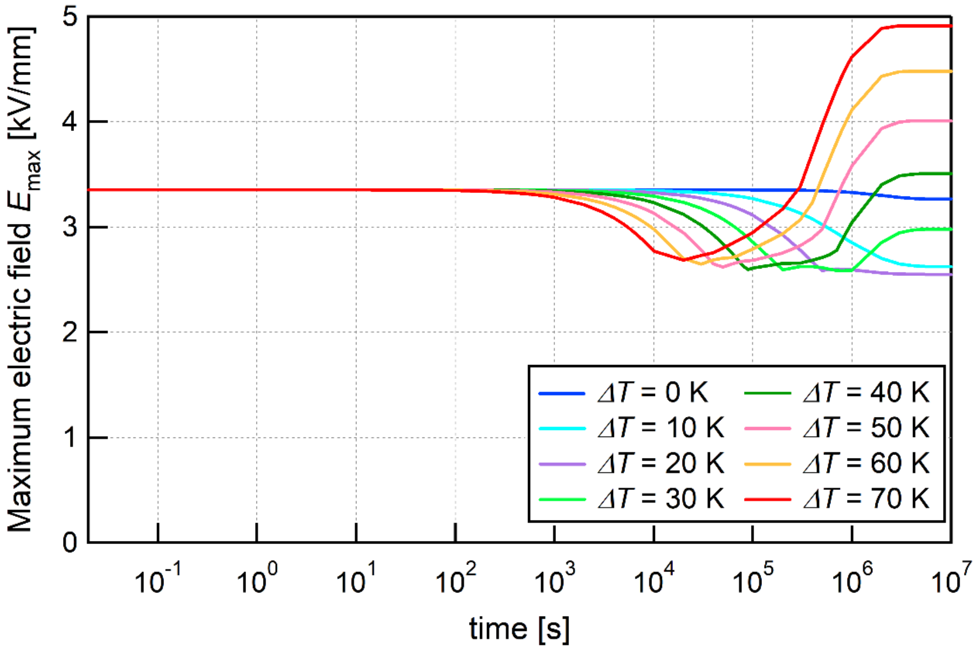

(a) Uniform spacer

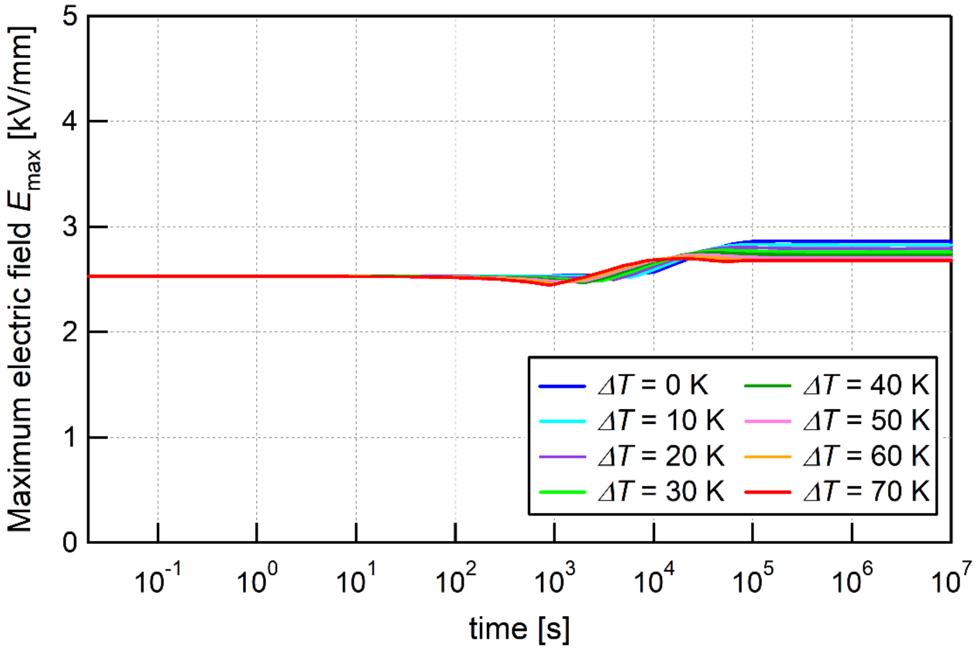

(b) ε/σ-FGM spacer

Fig. 4.6 E_{max} in gas after DC-on with varying ΔT.

can be seen from the figure, E_{max} of ε/σ-FGM spacer (2.53 kV/mm) is already relaxed compared to that of the Uniform spacer (3.35 kV/mm). It is because of the high ε_r of 12.7 that is provided by $SrTiO_3$-filled epoxy composite, compared to the Uniform spacer that only has ε_r of 4.0 by SiO_2-filled epoxy composite. The high ε_r at the spacer parts near HV conductor causes potential burden shifted to the spacer parts with lower ε_r, hence electric field stress around the spacer parts with higher ε_r is reduced.

As time passes, E_{DC} also occur toward steady state. That is why in Fig. 4.6 (a), the E_{max} near steady state varies with ΔT, as the conductivity depends on the temperature. However, the variation of E_{max} around ε/σ-FGM spacer is small as it gets closer to DC-SS, due to the high σ of σ(U) distribution and low T-dependency given by SiC-filled epoxy composite. It can also be seen that the time required for the electric field transition from ε-dependent to σ-dependent for ε/σ-FGM spacer is shorter than that of the Uniform spacer. It is due to the conductivity of ε/σ-FGM spacer that is higher than the Uniform spacer. Hence, the time constant which is defined by permittivity over conductivity decreases.

4.3.4 Superimposed LI voltage on DC-SS

From the last simulation condition, after the time-varying electric field reaches DC-SS under 27 kV voltage application on the HV conductor, positive and negative 100 kV LI voltage is superimposed. Electric field distribution as well as E_{max} location is monitored with varying time and temperature distributions. Figs. 4.7 and 4.8 show the electric field distribution and E_{max} around the Uniform and ε/σ-FGM spacers under superimposed positive LI voltage on DC-SS, while Figs. 4.9 and 4.10 show those under superimposed negative LI voltage on DC-SS.

Under superimposed positive LI on DC-SS, E_{max} decreases with ΔT for both Uniform and ε/σ-FGM spacers, although in the case of ε/σ-FGM spacer, it slightly decreases. Under superimposed LI on DC-SS, both capacitive and resistive fields present in the medium. As capacitive field is not affected by the change in temperature, so it is resistive field distributions that cause decrease in E_{max}, despite the E_{AC} component is larger in magnitude than E_{DC} component due to the LI voltage magnitude. With the increase of ΔT, σ of the spacer's part near spacer/HV interface is enhanced, suppressing the electric field around that area and distribute the equipotential lines to other areas with lower σ. Thus,

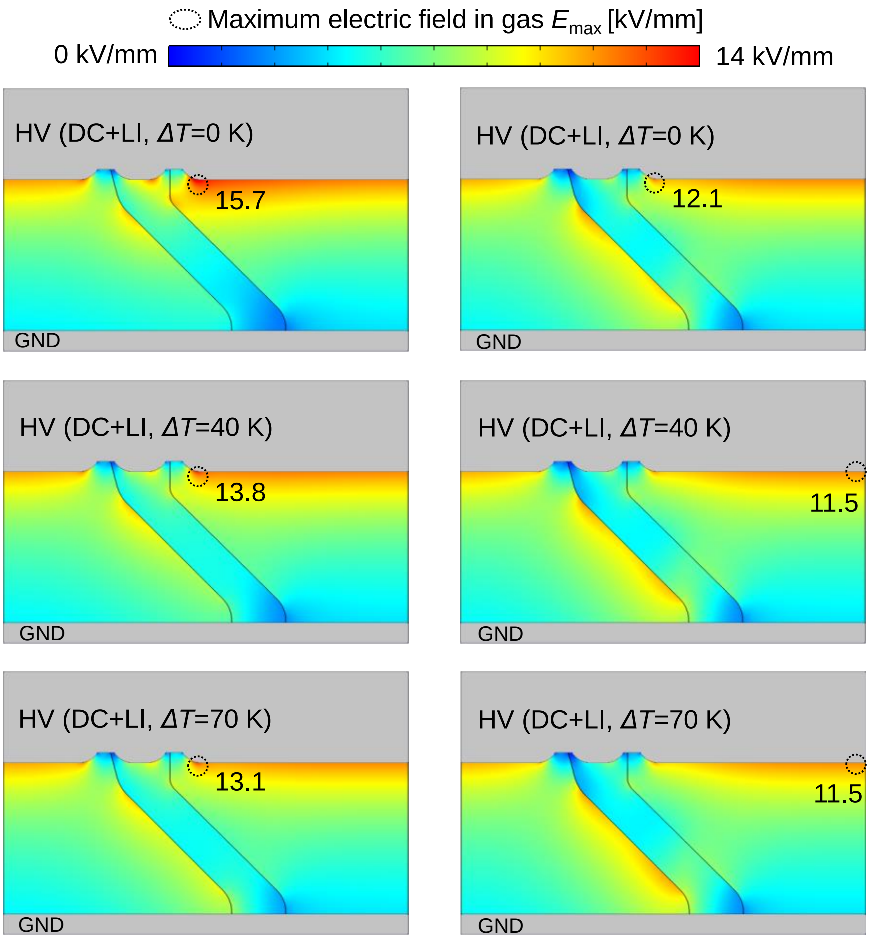

(a) Uniform spacer (b) ε/σ-FGM spacer

Fig. 4.7 Electric field distribution around (a) Uniform and (b) ε/σ-FGM spacers under DC+LI at ΔT=0, 40, and 70 K.

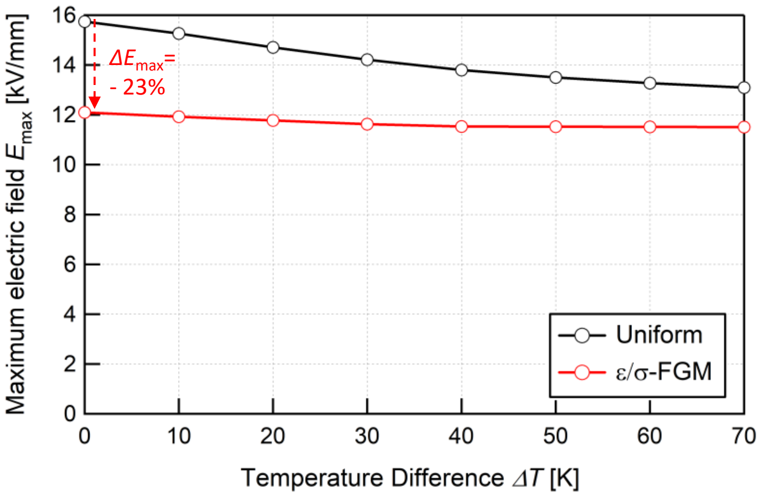

Fig. 4.8 E_{max} in gas under DC+LI with varying ΔT.

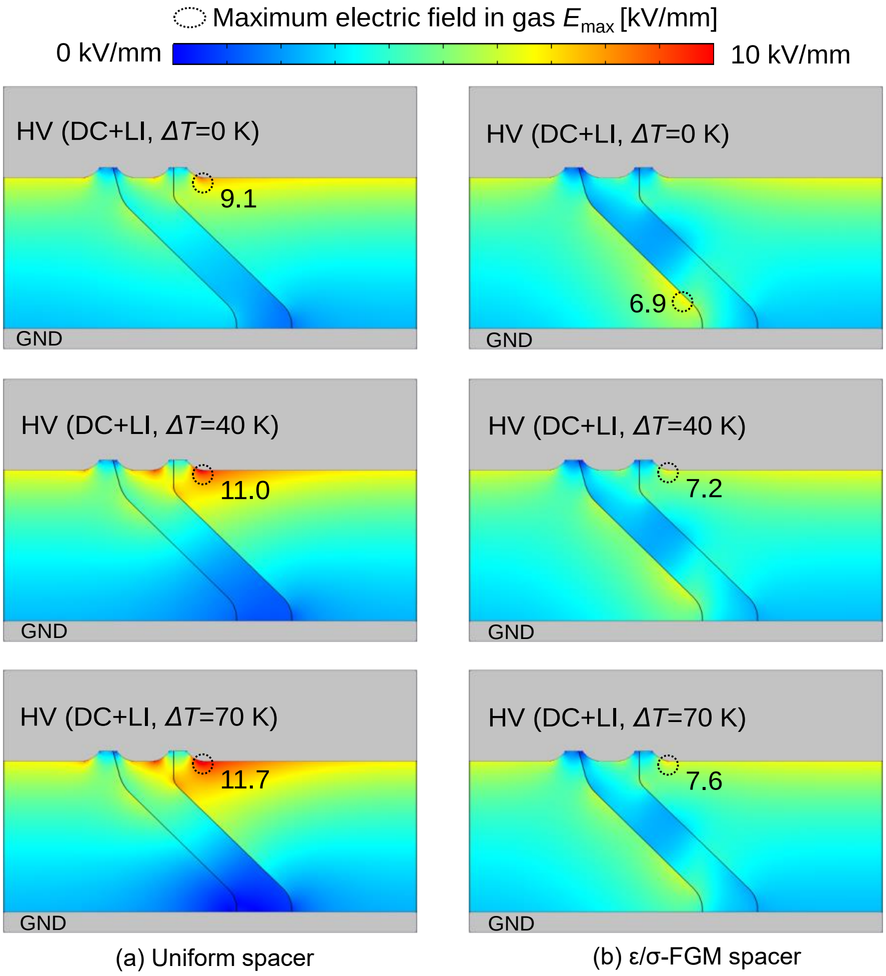

(a) Uniform spacer (b) ε/σ-FGM spacer

Fig. 4.9 Electric field distribution around (a) Uniform and (b) ε/σ-FGM spacers under DC-LI at *ΔT*=0, 40, and 70 K.

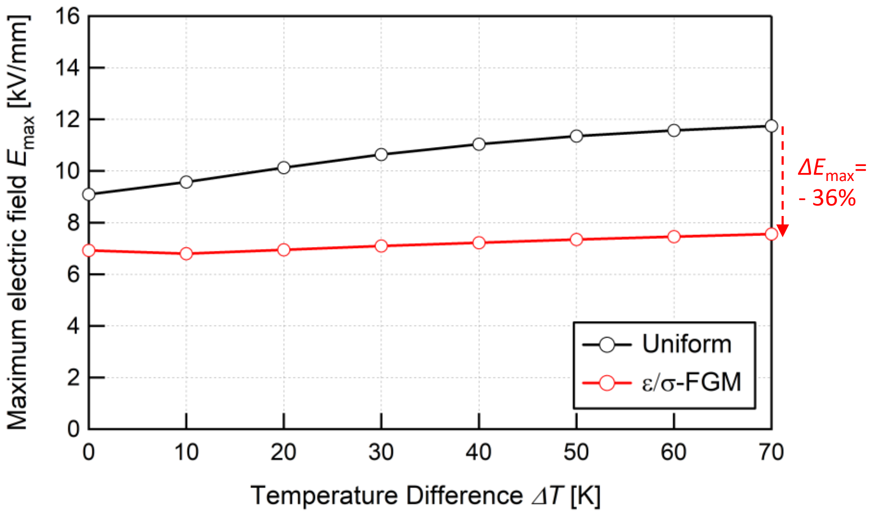

Fig. 4.10 E_{max} in gas under DC-LI with varying *ΔT*.

the E_{max} magnitude at HV shield edge is reduced (Fig 4.9).

Similar occurrence is also experienced by ε/σ-FGM spacer, however the starting point of σ is already 10^4 higher than that of the Uniform spacer (see Fig. 4.1 (c)). Therefore, E_{max} is already suppressed by large gap (23%) since ΔT= 0 K. This is what distinguish the current simulation results from the previous simulation results in Section 3.4.4, where GHC-type σ distribution has the same level of σ with the Uniform spacer at the spacer/HV conductor interface, and only higher σ at the spacer/GND enclosure interface. Consequently, the E_{max} reduction only reaches 7% at ΔT= 0 K (Fig. 3.21 in Section 3.4.4).

For superimposed negative LI on DC-SS, E_{AC} and E_{DC} component oppose each other, similar to the occurrence at DC-PR. Thus, E_{max} increases with ΔT. The E_{max} locations of both Uniform and ε/σ-FGM spacers are also the same as those under DC-PR at each different ΔT, as shown in Fig. 4.9. The E_{max} reduction under superimposed negative LI on DC-SS reaches 36% at ΔT=70 K.

4.4 Evaluation on Leakage Current and Temperature Rise Due to Internal Heating of ε/σ-FGM Spacer Model

4.4.1 Heat Conduction Analysis

In ε/σ-FGM concept, it is important to keep the σ level at some parts of the spacer high enough for field grading, but not too high that it can cause large leakage current flow in the spacer which leads to internal heating and eventually thermal runaway [12]. The previous electric field simulation steps have not included heat generation within the spacer due to leakage current. For that reason, in this Section, the temperature distribution, leakage current, and heat generation within ε/σ-FGM spacer is evaluated under DC-SS, in order to discuss the maximum σ level as well as the maximum SiC filler contents that are safe for ε/σ-FGM spacer not to cause thermal runaway.

Similar with the E simulation in Chapter 3, the heat conduction analysis is calculated by equation (4.1) below which is also derived from energy balance equation in the same way in section 3.2 [13, 14]. However, this time the spacer behaves as a heat source with Q is the heat generated within the spacer due to leakage current, and is calculated by equation (4.2).

$$\frac{\partial T}{\partial t}=\frac{1}{\rho C_p}\left(\frac{1}{r}\frac{\partial}{\partial r}\left(\kappa r\frac{\partial T}{\partial r}\right)+\frac{1}{r^2}\frac{\partial}{\partial \phi}\left(\kappa\frac{\partial T}{\partial \phi}\right)+\frac{\partial}{\partial z}\left(\kappa\frac{\partial T}{\partial z}\right)\right)+Q \tag{4.1}$$

$$\rho C_p\frac{\partial T}{\partial t}-\left(\frac{1}{r}\frac{\partial}{\partial r}\left(\kappa r\frac{\partial T}{\partial r}\right)+\frac{1}{r^2}\frac{\partial}{\partial \phi}\left(\kappa\frac{\partial T}{\partial \phi}\right)+\frac{\partial}{\partial z}\left(\kappa\frac{\partial T}{\partial z}\right)\right)=Q \tag{4.2}$$

In steady state,

$$-\left(\frac{1}{r}\frac{\partial}{\partial r}\left(\kappa r\frac{\partial T}{\partial r}\right)+\frac{1}{r^2}\frac{\partial}{\partial \phi}\left(\kappa\frac{\partial T}{\partial \phi}\right)+\frac{\partial}{\partial z}\left(\kappa\frac{\partial T}{\partial z}\right)\right)=Q \tag{4.3}$$

In vector form, equation (4.3) can be written as follows,

$$-\nabla\cdot(\kappa\nabla T)=Q \tag{4.4}$$

and Q is calculated by

$$Q=\boldsymbol{J}.\boldsymbol{E} \tag{4.5}$$

where T is temperature in K, t is time in s, κ is thermal conductivity in W/(m.K), ρ is density in kg/m^3, C_p is the specific heat capacity at constant pressure in J/(kg.K), Q is total heat dissipation density in spacer in W/m^3 , $\boldsymbol{J}$ is vector current density in A/m^2, $\boldsymbol{E}$ is vector electric field in V/m, and r, ϕ, z are the cylindrical coordinates of any point in the domain. Table 4.2 shows the values of κ, ρ, and C_p that are used in this simulation [15-18]. Here, the thermal conductivity κ is assumed to be constant.

The conductivity model which is applied in the spacer is obtained from equations in Fig. 2.8, and can be plot as a function of SiC filler contents as shown in Fig. 4.11.

Table 4.2 Heat conduction parameters

Material	κ [W/(m.K)]	ρ [kg/m^3]	C_p [J/(kg.K)]
Gas	0.014	23.43	0.065
Spacer	0.2	1500	1000
Conductor	155	2730	893

4.4.2 Temperature Rise and Leakage Current in ε/σ-FGM Spacer

Fig. 4.12 shows the maximum temperature (T_max) within the σ(U)-FGM spacer without ε grading, as a function of the lower level (x) of SiC filler contents, e.g x = 5 means σ(U)-FGM made of 5 to 10 vol% SiC-filled epoxy composite, x = 10 means σ(U)-FGM made of 10 to 15 vol% SiC-filled epoxy composite, and so on, with the fixed SiC filler content difference of 5 vol%. The simulation is conducted for two temperature differences between HV and GND conductors, which are ΔT=0 K and ΔT=70 K.

As can be seen in the figure, the simulated model of σ(U)-FGM composed of 5 to 10 vol% SiC-filled epoxy composite has T_max of 300 K when ΔT=0 K and 370 K at the

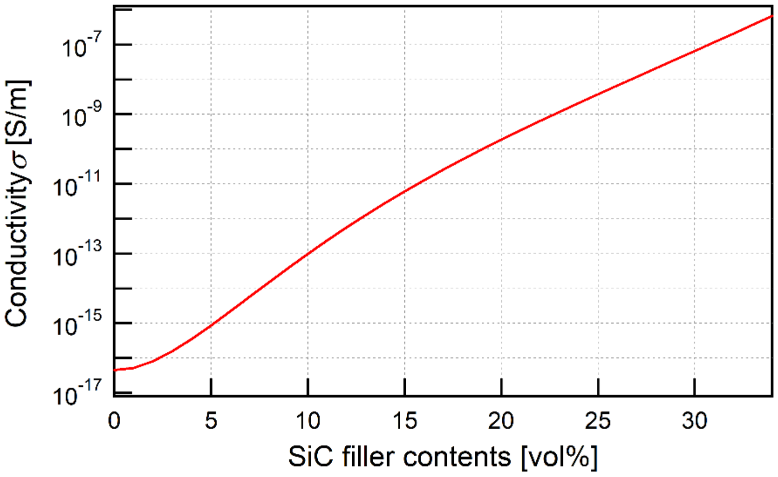

Fig. 4.11 Conductivity of spacer as a function of SiC filler contents at T=300 K and E=1 kV/mm

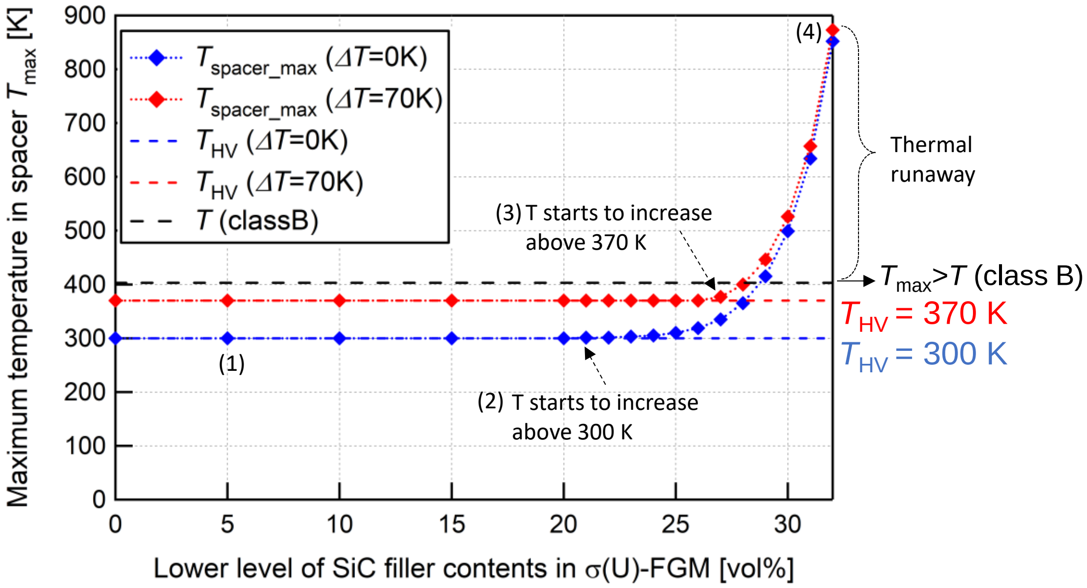

(2) T starts to increase above 300 K

(3) T starts to increase above 370 K

Thermal runaway

T_{max}>T (class B)

T_{HV} = 370 K

T_{HV} = 300 K

Fig. 4.12 Maximum temperature (T_{max}) in spacer due to internal heating.

spacer/HV conductor interface when ΔT=70 K. This means no heat generation within the spacer due to leakage current under DC-SS. The temperature distribution within the spacers follows the temperature gradient between the HV/GND conductors, as shown in Fig. 4.13. At this state, the leakage current (I_{LC}) is 0.89 pA to 2.59 pA for ΔT of 0 to 70 K (in the order of a few pA, as shown in Fig. 4.14). Then, the same T_{max} values and T distribution are still obtained until σ(U)-FGM with 20 to 25 vol% SiC-filled epoxy composite, with I_{LC} level that increases up to a few nA.

Afterward, when ΔT=0 K, T_{max} starts to increase above 300 K within σ(U)-FGM spacer with 21 to 26 vol% SiC-filled epoxy composite, as shown at (2) in Fig. 4.12 and in Fig. 4.15 (i). And when ΔT=70 K, T_{max} starts to increase above 370 K within σ(U)-FGM spacer with 27 to 32 vol% SiC-filled epoxy composite, as shown at (3) in Fig. 4.12 and in Fig. 4.15 (ii). At this stage, internal heating within spacer has started and is indicated by $T_{max} > T_{HV}$, where heat is generated by larger I_{LC} in the order of hundreds of nA up to tens of μA (Fig. 4.14(b)).

The exponential increase of T_{max} in Fig. 4.12 above 27 to 32 vol% SiC-filled epoxy composite level indicates the occurrence of thermal runaway. In this research, a condition is called as thermal runaway when the maximum temperature within spacer exceeds the maximum permissible temperature of epoxy resin (spacer) (insulation class B, T=130°C (403 K)) [19, 20]. Fig. 4.15 (iii) shows how the temperature distribution looks like at thermal runaway ((4) in Fig. 4.12). The area within the most inner red contour line (T=370 K) indicates the area with temperature over 370 K, and almost all of the spacer parts are in that area. The dark brown area around the middle part of the spacer indicates the area with temperature around 800 K, with T_{max} of 852 K and 873 K in the center of the spacer at ΔT=0 K and 70 K, respectively. Fig. 4.14 (a) also shows the catastrophic increase of I_{LC} in the order of hundreds of μA.

Fig. 4.16 shows the average heat generated within the spacer due to leakage current. According to the graph, temperature rises within the spacer (other than given by surrounding ΔT) when Q is more than 1 kW/m^3. Finally, we can find the level of maximum σ in Fig. 4.16. Spacer's internal heating starts when σ_{max} within the spacer reaches above 4x10^{-9} S/m. In the case of this simulation model under DC-SS, it is equivalent with σ(U)-FGM with the lower level of SiC filler contents of 21 vol%. Based on these results, it can be concluded that the ε/σ-FGM spacer with 5 to 10 vol% SiC-filled epoxy composite in this thesis will have no problem for internal heating or thermal runaway.

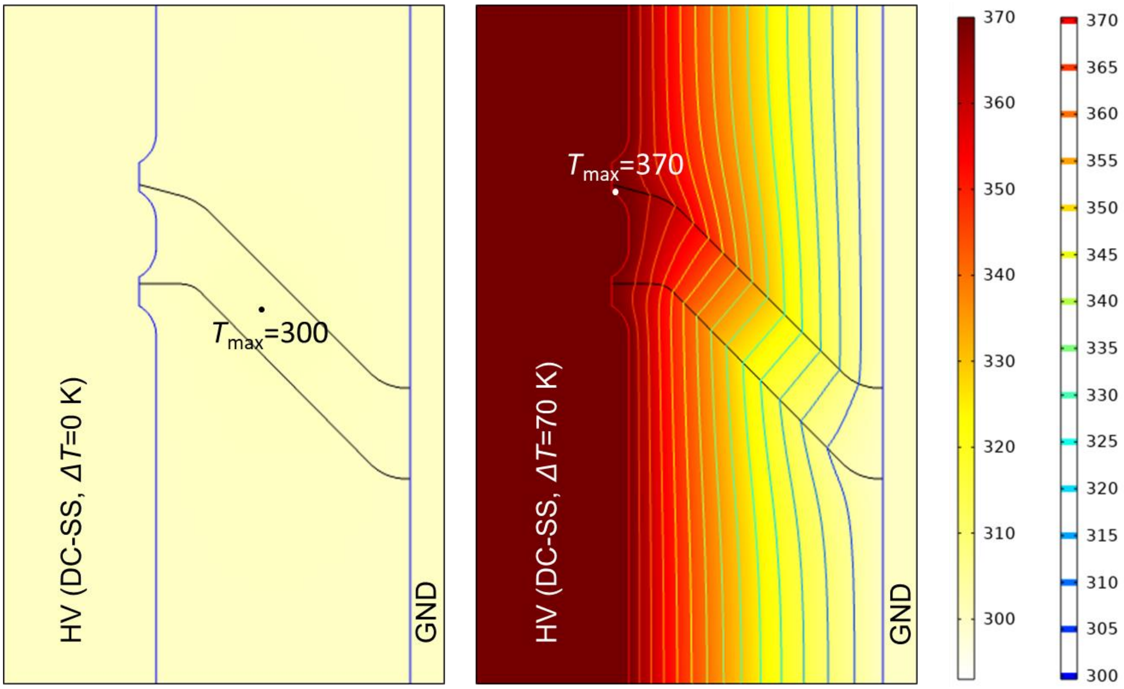

(a) (b)

Fig. 4.13 Normal temperature distribution on σ(U)-FGM spacer with SiC 5-10 vol% at (a) ΔT=0 K, and (b) ΔT=70 K.

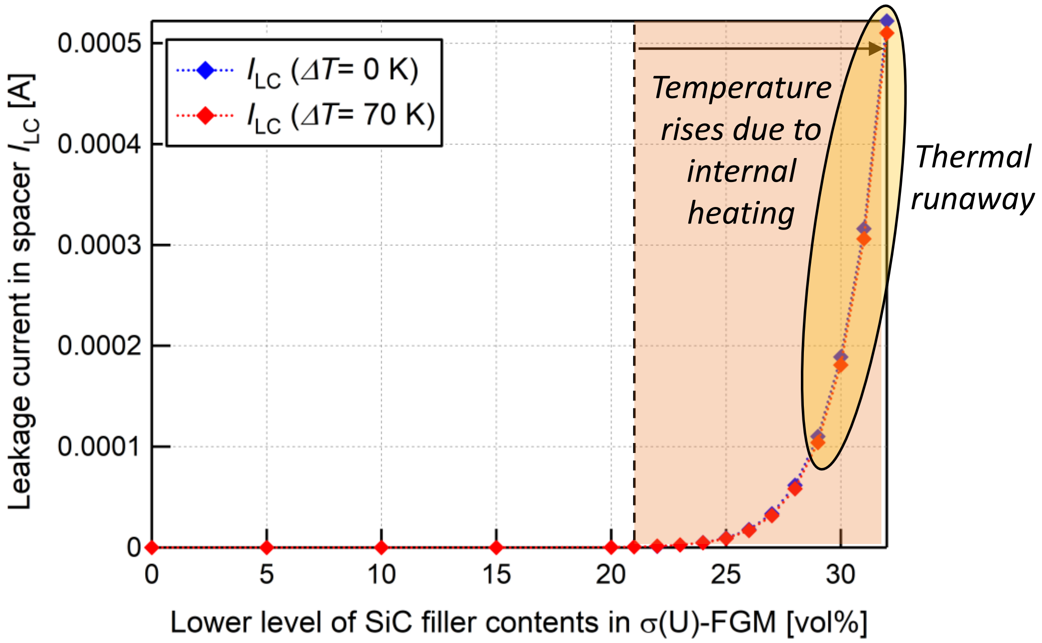

(a) I_{LC} (in linear axis)

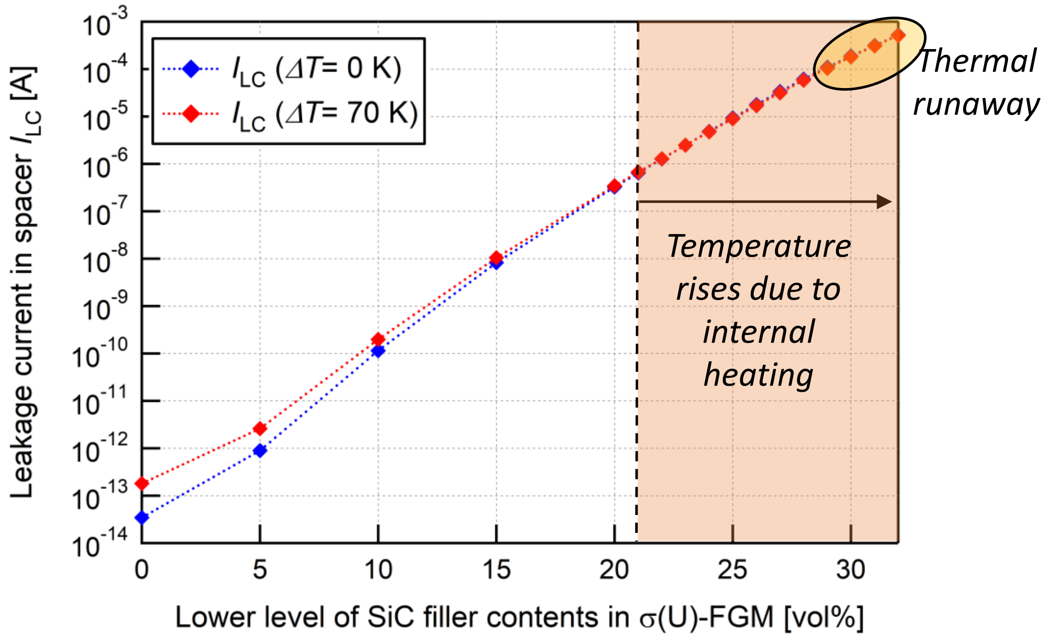

(b) I_{LC} (in log axis)

Fig. 4.14 Leakage current in the spacer in (a) linear axis, (b) log axis.

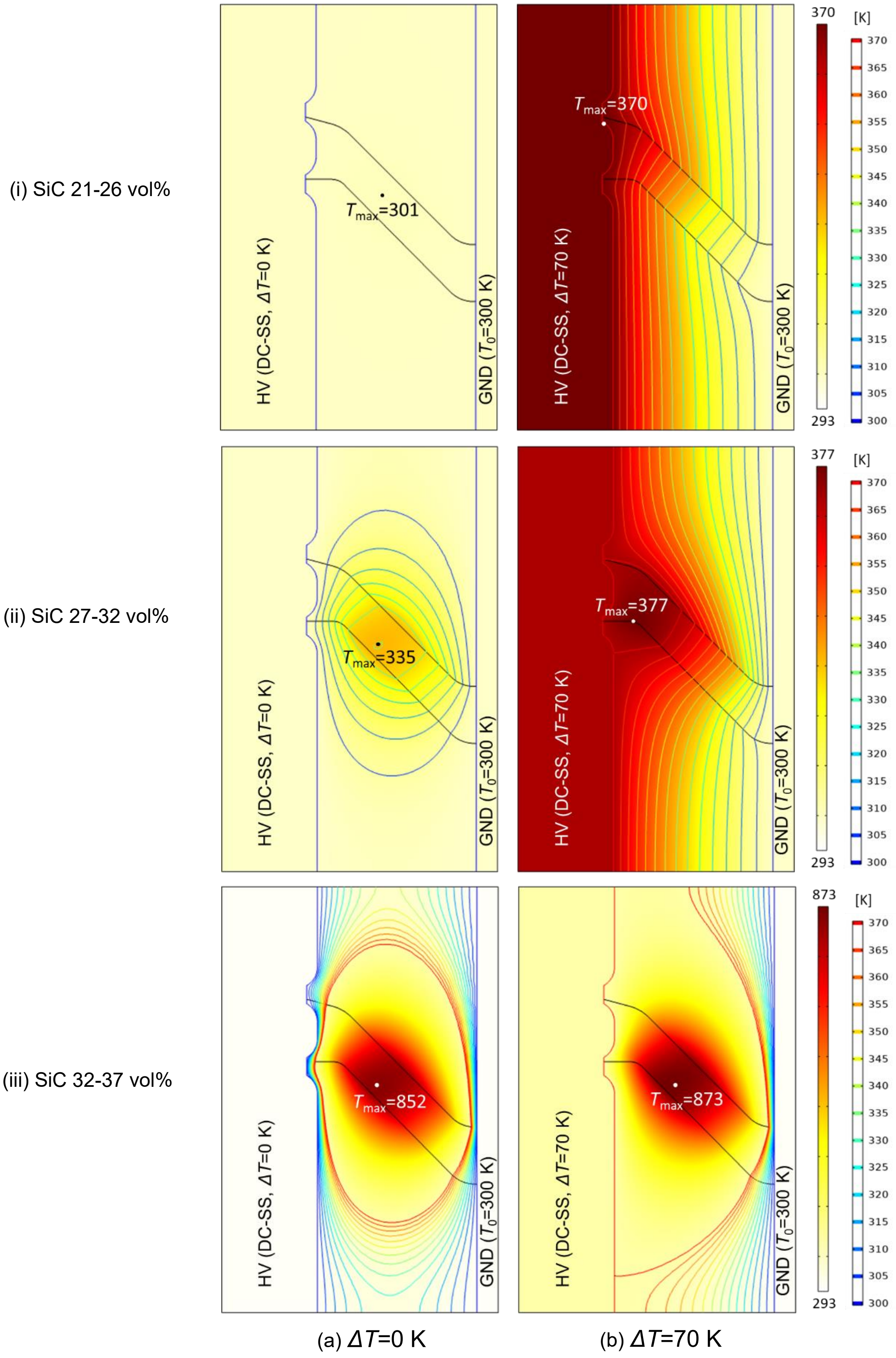
(i) SiC 21-26 vol%

(ii) SiC 27-32 vol%

(iii) SiC 32-37 vol%

(a) ΔT=0 K

(b) ΔT=70 K

Fig. 4.15 Temperature rises in σ(U)-FGM spacer with (i) SiC 21-26 vol%, (ii) SiC 27-32 vol%, (iii) SiC 32-37 vol% at (a) ΔT=0 K, and (b) ΔT=70 K.

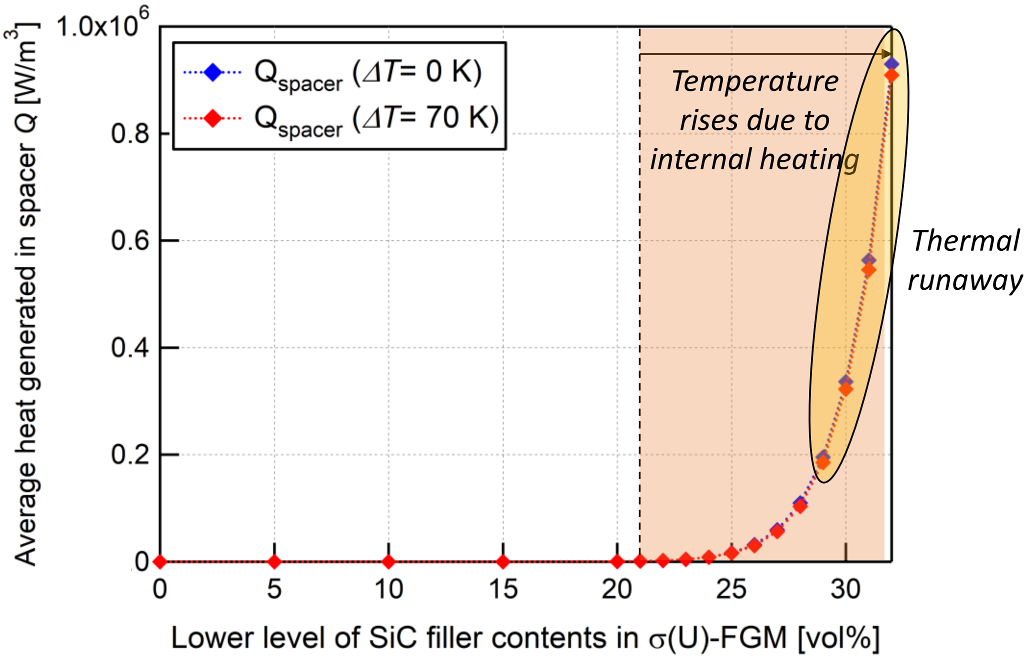

Fig. 4.16 Average heat generated within the spacer due to leakage current

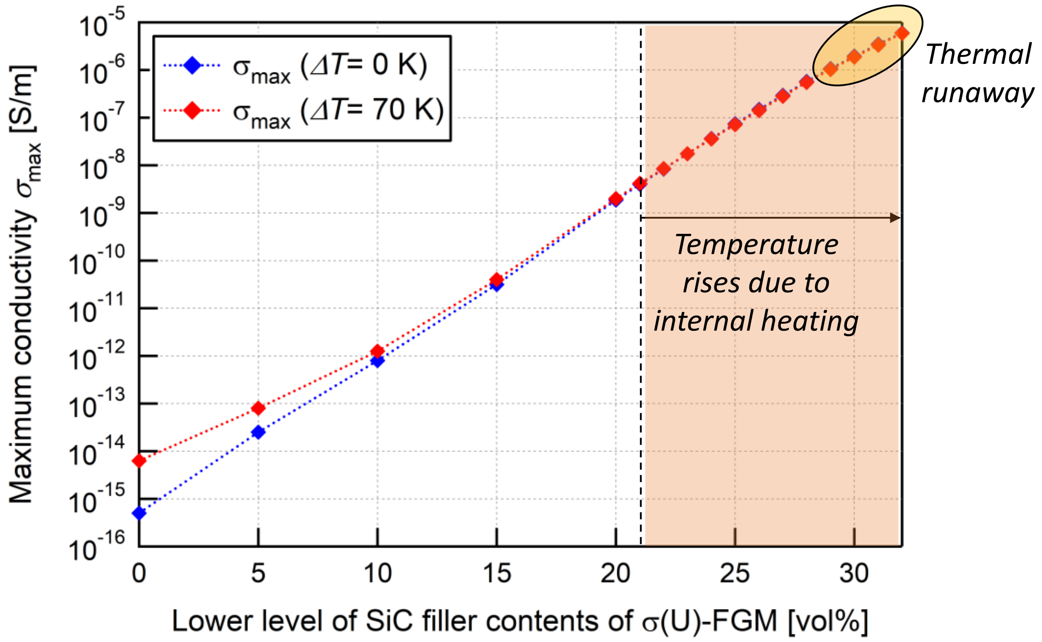

Fig. 4.17 Maximum conductivity within the spacer as a result of SiC filler addition.

4.5 Theoretical Discharge Inception Voltage (TDIV) Calculation of ε/σ-FGM Spacer

4.5.1 Volume-Time Theory

Breakdown test is an ultimate method to evaluate performances of the insulating materials. The electric field relaxation effect of ε/σ-FGM spacer which has been disclosed through simulation should contribute to the breakdown voltage improvement. The Volume-Time theory allows us to calculate the discharge inception probability at a given applied voltage which is suggested by the generation of initial electrons in high electric field volume in SF_6 gas, as expressed in equation (4.6) [21, 22],

$$P = 1 - \exp\left[-\int_t \int_{V_{cr}} \frac{dn_e}{dt}\left(1 - \frac{\eta}{\alpha}\right) dV dt\right] \tag{4.6}$$

where P is the generation probability of initial electrons, dn_e/dt is the number of electrons desorbed from SF_6^- ions per unit time and per unit volume, α and η are the ionization and attachment coefficients. V_{cr} is the critical volume which satisfies a condition where $\alpha > \eta$ and when streamer is formed, according to Schumann's formula, as in equation (4.7),

$$\int_{x_{cr}} (\alpha - \eta)\, dx = K \tag{4.7}$$

where K equals 18 for SF_6 gas and x_{cr} is the critical path along electric lines of force. The term $(\alpha - \eta)$ for SF_6 gas is expressed in equation (4.8),

$$\frac{\alpha - \eta}{p} = 27\left(\frac{E}{p} - 87.75\right) \tag{4.8}$$

where E is the electric field strength in kV/mm and p is the absolute pressure of SF_6 gas in MPa.

4.5.2 Electric Field Distribution of ε/σ-FGM Spacer under Lightning Impulse (LI) Voltage

The electric field distribution images in Fig. 4.18 are obtained through time-dependent electric field simulation under 100 kV_{peak} LI voltage without temperature gap. As can be seen in the figure, E_{max} is found at the shield edge in the concave side for both of the Uniform and ε/σ-FGM spacers. However, the magnitude of E_{max} of ε/σ-FGM spacer is reduced by 25% compared to that of the Uniform spacer, as shown in Fig. 4.19.

Under 100 kV_{peak} LI voltage, the capacitive fields are dominant, hence ε distribution within the spacer influences the electric field distribution. The constantly low ε distribution ($\varepsilon_r = 4$) of the Uniform spacer has higher electric field strength around the shield edge in the concave side of the spacer (indicated by red area in Fig. 4.18 (a)). On the other hand, ε/σ-FGM spacer has higher ε from the spacer/HV conductor interface until the middle part of the spacer ($\varepsilon_r = 12.7$). Thus, E_{max} at the shield edge is reduced, and the area with higher electric field strength on the spacer's concave surface (indicated by red ellipse) shows that potential burden is distributed uniformly around the middle part of the spacer.

Fig. 4.19 shows time varying E_{max} in SF_6 gas under LI 100 kV_{peak}, around the spacers without ε/σ grading (Uniform), with only GLP-type ε grading (ε(GLP)/σ(Uniform)-FGM), and with GLP-type ε grading combined with U-type σ grading (ε(GLP)/σ(U)-FGM, Fig. 4.1). The graph reveals that E_{max} around ε(GLP)/σ(Uniform)-FGM and ε(GLP)/σ(U)-FGM spacers are the same, confirming that the 25% E_{max} reduction effect under LI voltage is due to the ε grading. In this case, there is no temperature dependence on E_{max}. These electric field data under LI 100 kV are then used to calculate TDIV_{50} with the following results.

4.5.3 TDIV_{50} Calculation Results

TDIV_{50} refers to the applied voltage level at which the probability (P) of the discharge inception in equation (4.3) is 50%. Here, TDIV_{50} is calculated under standard LI voltage at varying SF_6 gas pressure from 0.1 to 0.5 MPa-abs, with results as presented in Fig. 4.20. The graph shows TDIV_{50} improvement of ε/σ-FGM spacer by at least 19% at 0.1 MPa-abs and at most 26% at 0.5 MPa-abs, compared to the Uniform spacer. This TDIV improvement is achieved due to the electric field relaxation effect which is contributed by ε grading, rather than σ grading, because mainly capacitive fields exist under time-varying LI voltage, as described in Fig. 4.19. With these results, it is verified that ε/σ-FGM spacer with GLP-type ε distribution and U-type σ distribution can give electric field relaxation effect, and hence TDIV improvement in DC GIS insulation system.

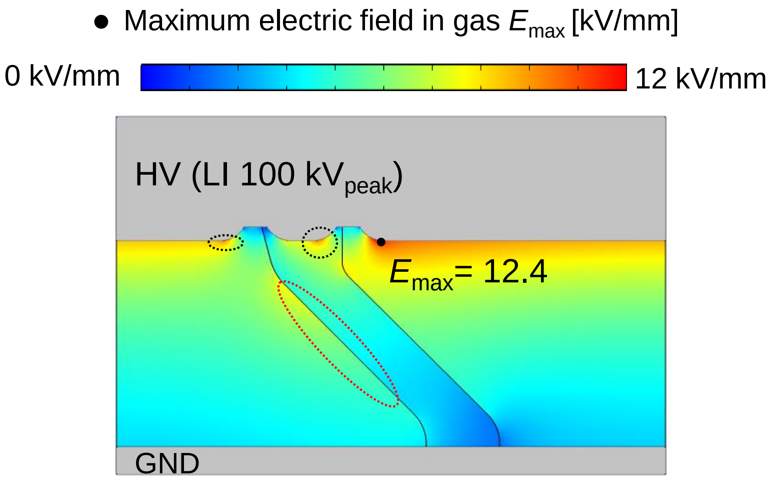

(a) Uniform spacer

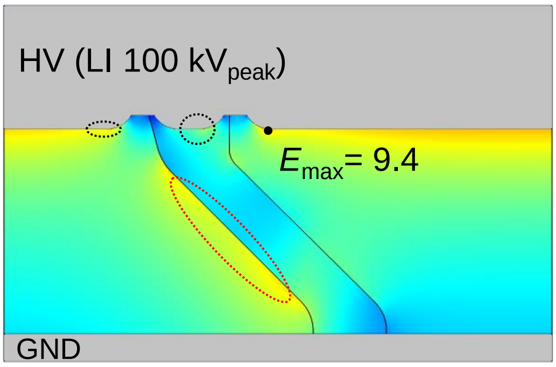

(b) ε/σ-FGM spacer

Fig. 4.18 E_{max} in gas under DC-SS with varying ΔT.

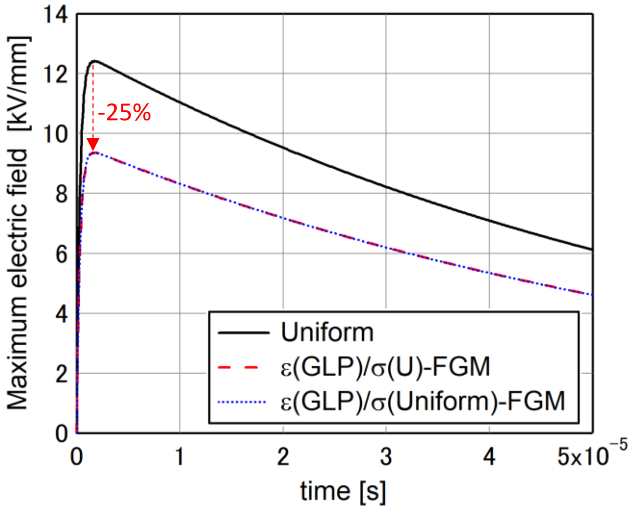

Fig. 4.19 E_{max} in SF_6 gas around the Uniform and ε(GLP)-FGM spacers with and without σ grading under LI 100 kV_{peak}.

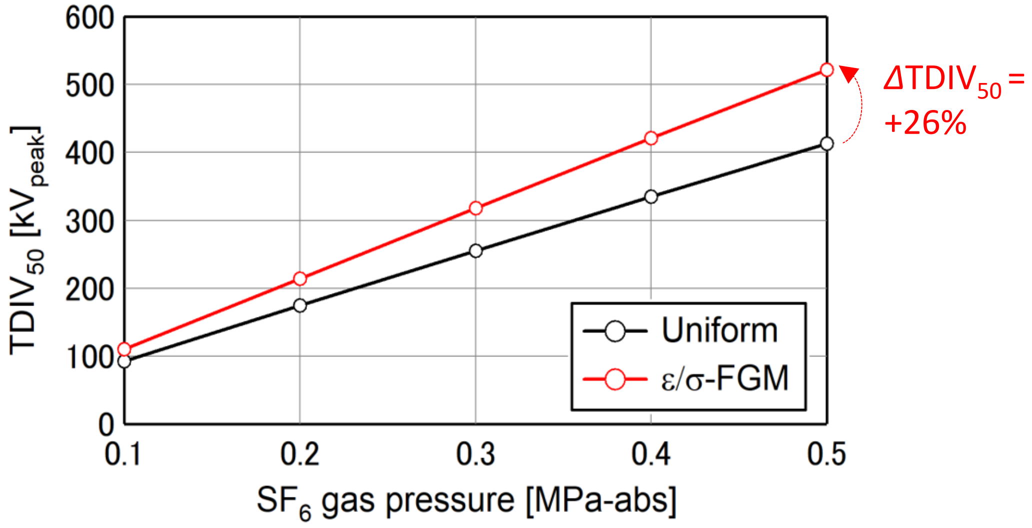

Fig. 4.20 TDIV$_{50}$ of the Uniform and ε/σ-FGM spacers under LI voltage and at varying SF$_6$ gas pressure.

4.6 Summary

In this chapter, toward future experimental verification, electric field relaxation effect of a scaled model ε/σ-FGM DC GIS spacer with actual measured ε/σ characteristics of functionally graded materials are evaluated under various DC operating conditions. In addition, theoretical discharge inception voltage ($TDIV_{50}$) of ε/σ-FGM spacer is calculated at various values of SF_6 gas pressure. The following results are obtained:

1) ε/σ-FGM spacer with GLP-type ε distribution (ε_r=12.7 to 4) containing 0 to 26.9 vol% $SrTiO_3$-filled epoxy composite and U-shaped σ distribution ($\sigma=10^{-15}$ to 10^{-13} S/m at T=300 K and E=1 kV/mm) containing 5 to 10 vol% SiC-filled epoxy composite resulted in better E relaxation effect than expected ε/σ-FGM spacer with ε/σ characteristics of typical epoxy resin. The maximum E_{max} reduction compared to the Uniform spacer obtained from the E calculations are 46%, 47%, 23%, and 36% under DC-SS, DC-PR, superimposed positive and negative LI on DC-SS, respectively.
2) The designed ε(GLP)/σ(U)-FGM spacer is estimated to have leakage current of about 0.89 pA to 2.59 pA at ΔT = 0 to 70 K, and no temperature rise occurs within the spacer due to internal heating.
3) $TDIV_{50}$ under LI applied voltage can be improved by 19 to 26% at SF_6 gas pressure of 0.1 to 0.5 MPa-abs, compared to the Uniform spacer.
4) σ(U) distribution in ε/σ-FGM spacer contributes more to the reduction of resistive fields under DC-SS, DC-PR, and superimposed LI on DC-SS. The high σ given by 5 to 10 vol% SiC-filled epoxy composite has smaller T-dependency, allowing almost constant field relaxation despite the increase in the temperature.
5) ε(GLP) distribution in ε/σ-FGM spacer contributes to the reduction of capacitive fields under DC-PR, DC-on, and LI applied voltages. Hence, $TDIV_{50}$ is improved.

Based on the above results, the following ε/σ-FGM specification in Table 4.3 is proposed for the ¼-scaled model of 245 kV AC GIS spacer or 1/12-scaled model of 320 kV DC GIS spacer.

Table 4.3 Proposed ε/σ-FGM specification

Spacer size	Inner diameter (φ = 20 mm) Outer diameter (φ = 60 mm) Height (h = 21.7 mm)
ε_r range	4 – 12.7
ε_r grading type	Grading-to-lower permittivity/GLP (high ε_r near spacer/HV conductor interface)
σ range	10^{-15} S/m – 10^{-13} S/m (at E=1 kV/mm, T=300 K) $\sigma_{max} < 10^{-9}$ S/m
σ grading type	U-shaped
$SrTiO_3$ filler contents	0 – 26.9 vol% (of total volume of $SrTiO_3/SiO_2$/EP composite)
SiC filler contents	5 – 10 vol% (of total volume of SiC/SiO_2/EP composite)

References

[1] U. Riechert, U. Straumann and R. Gremaud, "Compact Gas-insulated Systems for High Voltage Direct Current Transmission: Basic Design," in *IEEE PES Transmission & Distribution Conference & Exposition*, Dallas, USA, 2016, pp.1-5.

[2] U. Riechert, U. Straumann, R. Gremaud and M. Callavik, "Compact gas-insulated systems for high voltage direct current transmission: design and testing," in *IEEE PES Transmission & Distribution Conference & Exposition*, Dallas, USA, 2016, pp.1-5.

[3] H. Li, N. Zebouchi and A. Haddad, "Theoretical and practical investigations of spacer models for future HVDC GIL/GIS applications," in *Proceedings of the 21st International Symposium on High Voltage Engineering (ISH)*, Budapest, Hungary, 2019, vol. 2, pp.1538-1549.

[4] M. Hering, S. Grossmann, J. Speck and U. Riechert, "Investigation of the temperature influence on the breakdown voltage in gas insulated systems under DC voltage stress," in *Proceedings of the 18th International Symposium on High Voltage Engineering (ISH)*, Seoul, South Korea, 2013, OE7-2, pp. 1354-1359.

[5] A. Küchler, High voltage engineering Fundamentals-Technology-Applications, Berlin, Germany: Springer Vieweg, 2017.

[6] B. X. Du, Z. R. Yang, Z. L. Li, and J. Li, "Temperature-Dependent Charge Property of Silicone Rubber/SiC Composites under Lightning Impulse Superimposed DC Voltage," *IEEE Transactions on Dielectrics and Electrical Insulation*, vol. 26, no. 3, pp. 810-817, Jun 2019.

[7] X. Yang, X. Zhao, J. Hu, and J. He, "Grading Electric Field in High Voltage Insulation Using Composite Materials," *IEEE Electrical Insulation Magazine*, vol. 34, no. 1, pp. 15-25, 2018.

[8] Y. Miyazaki, A. Izu, Z. Liang, H. Kojima, H. Masui, H. Mitsudome, H. Yanase, K. Okamoto, K. Watanabe, K. Kato and N. Hayakawa, "Breakdown Characteristics of Cone-type ε-FGM Spacer for Gas Insulated Switchgears," in *9th International Symposium on Electrical Insulating Material*

(ISEIM), [online], 2020, VK-2, pp. 533-536.

[9] Y. Miyazaki, H. Kojima, H. Masui, H. Mitsudome, H. Yanase, K. Okamoto, K. Watanabe, K. Kato and N. Hayakawa, "Breakdown characteristics of cone-type ε-FGM spacer for gas insulated switchgears," *IEE Japan-A*, vol. 141, no. 10, pp. 546-551, 2021.

[10] N. Hayakawa, R. Oishi, H. Kojima, K. Kato and N. Zebouchi, "Electric field grading by Functionally graded materials (FGM) for HVDC gas insulated power apparatus," in *2018 IEEE Conference on Electrical Insulation and Dielectric Phenomena (CEIDP)*, Cancun, Mexico, 2018, 5-4, pp. 390-393..

[11] Rachmawati, H. Kojima, N. Hayakawa, K. Kato and N. Zebouchi`, "Electric Field Simulation of Permittivity and Conductivity Graded Materials (ε/σ-FGM) for HVDC GIS Spacers," *IEEE Transactions on Dielectrics and Electrical Insulation,* vol. 28, no. 2, pp. 736-744, 2021.

[12] M. Hering, K. Juhre, M. Secklehner and V. Hinrichsen, "Requirements on solid insulating materials and gas-solid interfaces in compact HVDC gas-insulated systems," in *The 20th International Symposium on High Voltage Engineering (ISH),* OG1-3, Buenos Aires, Argentina, 2017.

[13] 電気学会, "電熱工学," 第二改訂版, pp. 7-22, 1984.

[14] "Heat Transfer Module, User's Guide," Comsol Multiphysics®, p. 161, 2018.

[15] 宮﨑 勇作, "誘電率傾斜機能材料 ε FGM) を用いた実規模 GIS スペ ーサの絶縁性能向上に関する研究", 名古屋大学大学院工学研究科 修士学位論文, 2021.

[16] 宅間:「SF6 とはどんなものか？―その応用と性質―」,電気学会誌, Vol.115, No.8, pp.488-491, 1995.

[17] 電気学会：「固体絶縁材料の添加剤･フィラー効果」, 電気学会技術報告（Ⅱ部）, No.342, pp.30-48, 1990.

[18] ASM Specialty Handbook, "Aluminum and Aluminum Alloys," ASM International, USA, 1993, pp. 669.

[19] S. Ohta, "Temperature Classes of Electrical Insulators", *Three Bond Technical News,* No. 13, pp. 1-10, Dec 1985.

[20] JIS C 4003, Electrical insulation – Thermal evaluation and designation, 2010.

[21] N. Hayakawa, Y. Miyaji, H. Kojima and K. Kato, "Simulation on Discharge Inception Voltage Improvement of GIS Spacer with Permittivity Graded Materials (ε-FGM) by Flexible Mixture Casting Method," *IEEE Transactions on Dielectrics and Electrical Insulation,* vol. 25, no. 4, pp. 1318-1323, 2018.

[22] H. Okubo, H. Shumiya, M. Ito and K. Kato, "Insulation performance of permittivity graded FGM (functionally graded materials) in SF6 gas under lightning impulse condition," in *Proceedings of the IEEE International Symposium on Electrical Insulation (ISEI),* Toronto, Canada, 2006, 9-7, pp.332-335.

Chapter 5 Conclusions

5.1 Conclusions

The effectiveness of application of functionally graded materials (ε-FGM) on HVAC GIS/GIL spacers for electric field relaxation and hence, the downsizing of GIS/GIL have been long proven. However, the knowledge about its feasible application for HVDC GIS/GIL spacer is still unclear, and the research working on this particular topic are still limited. Therefore, it is important to investigate the feasibility of applications and insulation performances of FGM spacers with graded permittivity and conductivity (ε/σ-FGM) for HVDC GIS/GIL spacers.

This thesis elaborates the basic of DC-FGM concepts, the investigations on ε and σ characteristics of the used functionally graded epoxy composites, and the evaluation on insulation performance of ε/σ-FGM spacers in terms of electric field relaxation effect through electric field simulations, thermal conduction analysis, and breakdown probability improvement through theoretical discharge inception voltage (TDIV) calculations, with understanding of the electromagnetic theory, heat transfer analysis, and charge phenomena in GIS/GIL.

The outline of each chapter in this thesis as well as the results of this research are summarized below.

Chapter 2 discusses the concept of DC-FGM and the preliminary steps of material characteristics investigation of the used nonlinear composites, i.e. the permittivity and the conductivity characteristics of SiC- and $SrTiO_3$-filled epoxy composites. Bulk samples of SiC-filled epoxy composite with varying filler contents are fabricated using bulk cutting method and parallel glass pressing method. Then, the permittivity of each sample is measured by direct capacitance measurement, while the conductivity of each sample is measured using double-ring electrode method at varying applied voltages (applied field E= 1 to 10 kV/mm) and varying temperatures (T=303 K, 333 K, 353 K). Afterwards, multivariate analysis is performed on the σ measurement data to obtain σ characteristics as a function of T, E, and SiC filler contents.

The σ profiles of 0 to 10 vol% SiC-filled epoxy composite are obtained, however the ε profiles of the same range of filler contents show relatively small gap that is expected as not sufficient for capacitive field grading. Therefore, ε characteristics of $SrTiO_3$-filled epoxy composite which is already used for AC FGM spacer, is adopted here and incorporated to the implementation of ε/σ-FGM spacer for DC application.

Chapter 3 discusses the electric field analysis results of ε/σ-FGM application on a 320 kV HVDC GIS cone-type spacer model under various DC operating conditions: DC steady-state (DC-SS), DC polarity reversal (DC-PR), DC-on, and superimposed positive and negative LI voltage on DC-SS. The simulation is conducted using COMSOL Multiphysics® software by finite element method. In this simulation several types of ε and σ distribution shapes are applied on the ε/σ-FGM spacer model, such as U-type and grading-to-higher conductivity (GHC)-type, and each E relaxation effect are evaluated by also taking into account the temperature distribution effect. In this simulation, the ε/σ characteristics have not considered the actual measured SiC-filled epoxy composite, but rather the ε/σ characteristics of typical epoxy resin.

The results show that the effectiveness of FGM with graded σ for E relaxation under DC-SS is confirmed, where σ(U)-FGM and ε(U)/σ(GHC)-FGM spacers can reduce the $E_{\max}$ by 43% at ΔT of 70 K, compared to the Uniform spacer. The ε(U)/σ(GHC)-FGM spacer is evaluated as the most effective ε/σ distribution in reducing the $E_{\max}$ in gas compared to the Uniform spacer with constant ε and σ. The $E_{\max}$ reduction of at most 30%, 43%, 7% and 20% are achieved at DC-PR, DC-on, superimposed positive and negative LI voltage on DC-SS, respectively.

In Chapter 4, toward future fabrication and experimental verification of ε/σ-FGM spacer, similar electric field simulations to those in Chapter 3 are performed on a scaled model DC GIS cone type spacer and by implementing the actual measured ε and σ characteristics of $SrTiO_3$-filled and SiC-filled epoxy composites. Moreover, in order to make sure thermal runaway do not occur, the maximum level of SiC filler contents in FGM spacer at which temperature of the spacer does not increase due to internal heating is also investigated. Furthermore, the theoretical discharge inception voltage (TDIV) of ε/σ-FGM spacer is calculated under LI voltage to estimate the breakdown probability.

The results show that ε/σ-FGM spacer with GLP-type ε distribution (ε_r=12.7 to 4) containing 0 to 26.9 vol% $SrTiO_3$-filled epoxy composite and U-shaped σ distribution ($\sigma=10^{-15}$ to 10^{-7} S/m) containing 5 to 10 vol% SiC-filled epoxy composite resulted in even better *E* relaxation effect than those in Chapter 3, with maximum E_{max} reduction compared to the Uniform spacer obtained from the *E* calculations are 45%, 48%, 22%, and 36% under DC-SS, DC-PR, superimposed positive and negative LI on DC-SS, respectively. It is due to high σ given by 5 to 10 vol% SiC-filled epoxy composite has smaller *T*-dependency, allowing almost constant field relaxation despite the increase in the temperature.

The heat conduction analysis results suggest that temperature rise will not occur due to internal heating within the designed ε/σ-FGM spacer. Finally, the $TDIV_{50}$ calculation results under LI voltage show 19 to 26% improvement at SF_6 gas pressure of 0.1 to 0.5 MPa-abs, compared to the Uniform spacer. The ε(GLP) distribution here contributes to the reduction of capacitive fields under DC-PR, DC-on, and LI applied voltages. Hence, $TDIV_{50}$ is improved.

5.2 Future Problems

The feasibility of ε/σ-FGM application to HVDC GIS/GIL spacer has been analytically investigated with promising results. However, the ε/σ distribution specified in this paper is merely one example which is currently evaluated as the effective distribution for electric field relaxation on the current model of DC GIS/GIL spacer. The ε/σ distribution shapes may change depending on the size and shape of spacer and can be optimized through inverse analysis [1], which can be our future works.

More practically, the ε/σ-FGM spacer sample fabrication through Flexible Mixture Casting (FMC) method is required to be conducted so that we can evaluate if the combination using three types of different composites can result in independent ε and σ distributions as expected. Verification of ε and/or σ distribution in the fabricated ε/σ-FGM samples by non-destructive method, e.g. X-ray CT scanning method, is expected [2]. Then, experimental verification on the insulation performance of the fabricated ε/σ-FGM spacer is needed by conducting breakdown test under positive and negative LI voltage. The results are then to be compared with the already calculated $TDIV_{50}$. For further applications, the compatibility of ε/σ-FGM spacers of DC GIS/GIL with SF_6 gas alternatives can also be expected for global warming mitigation.

References

[1] K. Kato, H. Kojima, N. Hayakawa, H. Masui, H. Yanase, K. Okamoto and H. Okubo, "Inverse analysis of optimum permittivity distribution for FGM spacer in consideration with multiple objective functions in gaseous insulation systems," in *22nd Int. Symp. High Voltage Engineering (ISH)*, no. 401, *online*, 2021.

[2] 加藤 拓夢 他, "X 線 CT を用いた誘電率傾斜機能材料（ε-FGM）の誘電率分布測定," in 電気・電子・情報関係学会東海支部連合大会, A5-7, *online*, 2021.

Acknowledgement

First of all, I would like to express my deepest gratitude to my research and academic advisor, Professor Naoki Hayakawa of the Department of Electrical and Engineering, Nagoya University, for his generous and thorough guidance and encouragement in the last 3.5 years while I am doing this research in Hayakawa Laboratory. I would also like to express my sincere gratitude to Professor Yasunobu Yokomizu and Associate Professor Hiroki Kojima of the Department of Electrical Engineering, Nagoya University, as well as to Professor Yukio Mizuno of the Department of Electrical and Mechanical Engineering, Nagoya Institute of Technology who have kindly provided knowledge and expertise regarding this research work and during this thesis preparation.

Secondly, I would like to express my deepest appreciation to my research collaborators, Dr. Katsumi Kato of the Department of Electrical Engineering and Information Science, National Institute of Technology, Niihama College, and Dr. Nabila Zebouchi of the Advanced High Voltage Engineering Research Centre, Cardiff University, UK for their useful comments and support to these research works and in preparing each academic papers. I would also like to extend my sincere thanks to Associate Professor Muneaki Kurimoto of the Institute of Materials and Systems for Sustainability, Nagoya University who has provided solution and knowledge to some technical problems that I faced.

I am also thankful to Professor Suwarno of the School of Electrical Engineering and Informatics, Institut Teknologi Bandung (ITB) who has recommended me to Professor Hayakawa and gave me a chance to pursue my doctoral study in Nagoya University.

I am also grateful to the students and secretaries of Hayakawa Laboratory, who have been helpful since the beginning and along the way, especially to Dr. Ryuichi Nakane, Dr. Takefumi Kaji, Mr. Atsuhiro Izu, Mr. Yusaku Miyazaki, Mr. Liang Zhaoyuan, Mr. Takumu Kato, and Mr. Hideaki Kato for their supportive comments and knowledge sharing. Additionally, I would like to thank Mr. Motoshi Hirai of Kato Laboratory who has taught me a new method of fabricating thin samples.

Finally, I would like to thank my family, especially my husband and daughters who have endlessly supported and accompanied me during this journey, as well as to my colleagues in ITB for their constant support.

List of Publications Concerned with This Dissertation

Publications in Academic Journals Regarding This Research

Chapter	Title	Journal Name	Co-authors
3	Electric Field Simulation of Permittivity and Conductivity Graded Materials (ε/σ-FGM) for HVDC GIS Spacers	IEEE Transactions on Dielectrics and Electrical Insulation, Vol. 28, No. 2, pp. 736-744 (2021)	Hiroki Kojima Katsumi Kato Nabila Zebouchi Naoki Hayakawa
2 4	Electric Field Grading and Discharge Inception Voltage Improvement on HVDC GIS/GIL Spacer with Permittivity and Conductivity Graded Materials (ε/σ-FGM)	IEEE Transactions on Dielectrics and Electrical Insulation, *accepted* (2022)	Hiroki Kojima Katsumi Kato Nabila Zebouchi Naoki Hayakawa

Publications in International Conferences Regarding This Research

Chapter	Title	Conferences Name	Co-authors
3	Electric Field Grading by Permittivity and Conductivity Graded Materials (ε/σ-FGM) for HVDC Gas Insulated Power Apparatus	2020 International Symposium on Electrical Insulating Materials (ISEIM), September 13-17, web conference, pp. 421-424 (2020)	Atsuhiro Izu Ryuichi Nakane Hiroki Kojima Katsumi Kato Nabila Zebouchi Naoki Hayakawa
2 4	Application of SiC-filled Permittivity and Conductivity Graded Material (ε/σ-FGM) in HVDC GIS Spacer	22nd International Symposium on High Voltage Engineering (ISH), November 21-25, hybrid conference (Xi'an, China), No. 729 (2021)	Hiroki Kojima Katsumi Kato Nabila Zebouchi Naoki Hayakawa